SCALE EFFECTS ON CAVITATION INCEPTION IN SUBMERGED JETS

Thesis by

Kean Khoon Ooi

In Partial Fulfillment of the Requirements

for the Degree of

Doctor of Philosophy

California Institute of Technology

Pasadena, California

1982

(Submitted on December 14, 1981)

ACKNOWLEDGMENTS

I would like to express my gratitude and thanks to my thesis advisor, Professor A.J. Acosta, for his invaluable assistance, guidance and advice throughout the course of the present work. His concern for the welfare of this writer is deeply appreciated. Thanks also go to Professor R.H. Sabersky who expressed a continuing interest in this research work and for his many helpful suggestions and comments. Dr. D. Oldenziel provided useful suggestions and stimulating discussions. This is gratefully acknowledged.

I would like to thank my colleague J. Katz. His advice and assistance on matters related to holography were instrumental in bringing about a successful completion of the present holographic studies.

E.F. Daly is deserving of special mention for his help during the design stages of the experimental apparatus. He has never ceased to amaze this writer with his uncanny design abilities. I am also grateful to J. Fontana who did the machining and assembly of the various components of the experimental equipment. Thanks are due too, to R. Eastvedt and L. Montenegro for their assistance.

Several students helped in the processing of films and data reduction. In this respect, I would like to thank Catherine Petrov, Ronald Franz and Tawach Ungsuwarungsri.

I am grateful to Susan Berkley and Rennie Dudek for their help and friendship. They have gone out of their way to accommodate the wishes of this writer, for which I am thankful.

I would like to acknowledge the financial support of the Institute

and of the Naval Sea System Command General Hydrodynamic Research Program administered by David W. Taylor Naval Ship Research and Development Center.

Finally, I would like to express my deepest thanks to my family for their never ending support. It is to them and the memories of my mother that I dedicate this work.

ABSTRACT

The present work is an investigation into the scale effects on cavitation inception in submerged water jets. Four scale effects were studied: (i) jet size, (ii) jet velocity, (iii) dissolved air content, and (iv) the nuclei population in the flow. The nuclei population was artificially altered by "electrolysis seeding."

Holography and schlieren photography were used to observe the flow. Direct measurements of the nuclei population were also accomplished by holography. In addition, the instantaneous pressure field in the jet was successfully mapped out using specially tailored bubbles as pressure sensors.

It was found that inception did not generally occur in the cores of the turbulent eddies and that the region in which the cavities were first seen were dependent on the size of the jet.

Pressure measurements showed that negative peak pressure fluctuation intensities of as high as 120 percent of the dynamic head existed in the jet. The results also revealed that the instantaneous pressure fluctuations have a slightly skewed bell shape probability distribution.

For the present tests, the inception index was independent of the exit velocity for a constant size jet. However, when the flow was seeded, the inception number showed a linear dependence on velocity and this dependence increased with increased number of seeded nuclei. The effects of the nuclei number density and pressure fluctuations are incorporated in a "probable cavitation occurrence" parameter which

shows promise in reducing scatter in this type of experiment.

TABLE OF CONTENTS

TABLE OF CONTENTS (continued)

TABLE OF CONTENTS (continued)

List of Symbols

D	diameter of the nozzle
f	frequency of pressure fluctuation
G	volume of hydrogen gas produced by electrolysis per unit time
I	current through the electrode
K_a, K	constant of proportionality
ℓ_w	length of the exposed portion of the electrode
L_j	length of the laminar region in the jet
m	number of cavitation events per unit time
n	total number of nuclei present in the cavitation-prone region of the jet
n_k	number of nuclei present in a particular size category
n_d	number of nuclei that are normally present in the flow field in the absence of flow seeding
$\dot{n}_g$	number of hydrogen bubbles produced by electrolysis per unit time
N_b	frequency of occurrence
N_b^*	maximum frequency of occurrence
$N(\overline{R})$	nuclei number density distribution function
N_P	probable cavitation occurrence parameter
P'	instantaneous pressure fluctuation
P_c	cavity pressure
$P_g(T)$	partial pressure of the gas in the cavity at temperature T
P_o	reference pressure or free stream pressure
P_T	mean static pressure in the water tunnel at inception
$P_v(T)$	vapor pressure of liquid at the bulk temperature

$P_\ell, P_\infty(t)$ instantaneous local static pressure

P_{g_o} partial pressure of the gas in the bubble at the reference position

P_{g_x} partial pressure of the gas in the bubble at position x

$P(P_f)$ cumulative probabilities of favorable negative peak pressure fluctuations intensities that would cause the explosive growth of a nucleus

$P(m)$ probability of m cavitation events occurring per unit time

$\frac{P}{\frac{1}{2}\rho V_j^2}$ rms of the dimensionless pressure fluctuations

Q volume of the cavitation-prone region

$\dot{Q}_j$ volume discharged through the nozzle per unit time

r radial position in the jet

R instantaneous bubble radius

R_e radius of the bubble immediately after exiting from the nozzle

R_g radius of the bubbles produced by electrolysis

R_m geometric mean radius of the ellipsoidal bubble

R_o reference bubble radius

R_x radius of the bubble at position x

$\overline{R}$ mean radius of the bubble or nucleus

R^* dimensionless bubble radius $(= \frac{R}{R_o})$

Re_D jet exit Reynolds number $(= \frac{V_j D}{\nu})$

$\dot{R}$ radial velocity of the bubble

$\ddot{R}$ radial acceleration of the bubble

S surface tension

St Strouhal number $(= \frac{fD}{V_j})$

t	time
T	bulk temperature of the liquid
T_B	characteristic bubble response time
u_o	tangential velocity of the bubble ($= w_o R_o$)
V_j	exit velocity of the jet
V_∞	reference velocity or free stream velocity
W_e	Weber number ($= \frac{S}{\rho R_o u_o^2}$)
x	axial position in the jet
α	dissolved air content
$\bar{\alpha}$	average dissolved air content
β	damping constant
γ	polytropic index (= 4/3)
ε	amplitude of oscillation of a bubble from the initial size
ε^*	dimensionless amplitude of oscillation of the bubble ($=\varepsilon/R_o$)
ν	kinematic viscosity of the liquid
ρ	density of the water
σ	cavitation number
σ_i	cavitation inception number
ω	circular frequency of pressure fluctuation
ω_o	natural circular frequency of the bubble
ω^*	dimensionless circular frequency ($= \frac{\omega}{\omega_o}$)

FIGURE CAPTIONS

1. INTRODUCTION

1.1 General Background

One of the first questions a layman or a newcomer to the study of cavitation would ask would be "What is cavitation?" Cavitation here can be defined as the occurrence of a second gaseous phase in a liquid. The second phase could be a mixture of some noncondensable gas and the liquid vapor or just pure vapor. The change of phase is usually brought about by dynamical pressure reduction at a constant temperature.

Among the first persons to observe cavitation on ship propellers was O. Reynolds in the late nineteenth century. Since then, it has captured the attention of a wide spectrum of professionals ranging from engineers in various disciplines to applied mathematicians, primarily because of the widespread harmful effects that accompany this process. The performance of numerous hydraulic machines has been gravely affected by cavitation, especially in the advanced stages. Examples are, the decreased power output of turbines and the increase in drag on marine vehicles. In addition, when the cavities collapse, pressure shock waves and high velocity microjets are generated. If these shock waves and microjets strike the surfaces of machinery, erosion by pitting of these surfaces would be sustained. Other deleterious effects of cavitation include noise and vibration. As a direct result of all these adverse effects, cavitation has been responsible for very expensive premature repairs or replacement of parts of hydraulic devices.

In recent years, the use of artificial heart valves has been on the increase. The valves have to be very carefully tested to insure that they do not give rise to cavitation as the consequences could be fatal. This area of study is being pursued, for example, by Freed et al [39].

In view of all these devastating effects that accompany the cavitation process, it is not surprising to find that researchers and engineers alike are actively engaged in extensive related research. It is hoped that with increased understanding of this common but perplexing phenomenon, better future designs of hydraulic machines and marine vehicles would occur with eventual huge savings.

A first step towards a better understanding of the cavitation process would be to determine the cause. This would require a close examination of the microscopic structure of the liquid itself which will now be briefly considered.

1.2 Cavitation Nuclei

Plesset [97] has shown, from his theoretical analysis, that a pure homogeneous liquid could sustain tensile stresses of several thousands of atmospheres. However, laboratory tests performed by Dixon (1909), Vincent (1943) and Scott (1948) as reported by Knapp et al [71] demonstrated that even under the most careful tests, tensile strengths of only a few hundred atmospheres have been measured. This discrepancy in the measured and the calculated values of tensile

stresses led workers in this field to postulate the existence of "weak spots" in real life liquids. Two questions that immediately come to mind at this point are the nature of these "weak spots" and the part they play in the cavitation inception process.

Solid impurities in the form of hydrophobic particles were proposed by Pease and Blinks [93] as probable "weak spot" candidates. However, Plesset [97] and Holl [54] have examined these and have dismissed them as unlikely. It is now generally accepted that these "weak spots" exist in the form of undissolved gas or vapor pockets in the liquid. Now, Epstein and Plesset [34] have demonstrated that free gas bubbles of finite sizes would rise to the surface of the liquid while bubbles that were small enough to experience Brownian motion would be forced into solution by the immense surface tension forces acting on them. Therefore, for the undissolved gas or uncondensed vapor pockets to exist, some agent responsible for stabilizing the bubbles has to be present. Several mechanisms have been proposed to explain the stabilized states of these pockets.

Fox and Herzfeld [35] suggested that an organic skin around the gas bubble prevented gas from diffusing into the liquid. Again, after careful consideration, Plesset [97] has concluded that this was an improbable candidate. The most widely accepted model was that suggested by Harvey et al [49]. In this model, Harvey proposed that the undissolved gas could be trapped in the crevices of suspended particles. His analysis showed that when the liquid pressure dropped below the vapor pressure, the gas pockets trapped in the crevices

would "seed" the flow, otherwise they remained permanently stabilized in the crevices. A further analysis of Harvey's model and a critical review of other proposed models can be found in Chapter 3 of the monograph by Knapp et al [71] and also the work of Holl [53].

With the nature of the "weak spots" established, the remaining question to be answered is the role they play in bringing about the onset of cavitation in liquids. It is obvious that since the weakest points in a liquid are of the "weak spots", the inception of cavitation would take place at one or more of these spots. Since these spots serve as the nuclei on which the cavities grow, they are commonly referred to as cavitation nuclei. Typically, when a cavitation nucleus traverses a region where the pressure in the flow is below the vapor pressure, the bubble will explode violently, giving rise to the term "vaporous cavitation". It is conceivable also to think of gas diffusing into the bubble across the interface from a super-saturated liquid, thus giving rise to a "cavity". This type of cavitation is often referred to as "gaseous cavitation" and can take place at liquid pressures both above and below the vapor pressure. However, this process proceeds at a much slower rate than "vaporous cavitation". Both types of cavitation have been observed experimentally.

1.3 Scale Effects

As discussed earlier, cavitation is always accompanied by many harmful effects. Consequently, prior to the construction of a new

design of hydrodynamic vehicle or hydraulic machine, it is desirable to predict its performance. If the design is known to cavitate under normal operating conditions, then there is a need to modify the design which will eventually result in the successful operation of the machinery. Unfortunately, most flows, especially those that are likely to cavitate, are very complex and therefore do not succumb readily to mathematical analysis. The only recourse to predict the performance of the new design, short of actually constructing a prototype and operating it, is to do model tests. These tests are often performed in towing tanks or water tunnels where the model could be mounted and tested under various controlled flow conditions. Once the results of the model tests are obtained, the remaining problem is to extrapolate these data to a full scale model or prototype.

An important parameter in cavitation tests is the cavitation number defined by

$$\sigma = \frac{P_\infty - P_v}{\frac{1}{2}\rho V_\infty^2}$$

where P_∞ and V_∞ are some reference pressure and velocity, respectively, P_v, the partial pressure of the vapor phase of the liquid evaluated at the bulk temperature of the liquid and ρ, the density of the liquid. If the tests are carried on in a water tunnel say, the reference pressure and velocity are usually taken to be the free stream pressure and velocity, in that order. The cavitation number

at the start of cavitation is referred to as the "incipient cavitation index".

It follows that if the incipient cavitation index is the only important scaling parameter, then, the onset of cavitation on the test model and the prototype would occur at the same value of σ when both are operated at identical dynamical conditions. However, this is found not to be the case. Cavitation inception has been found to depend not only on the model size, test velocity and fluid properties but also on the nuclei population in the fluid, among many other parameters. These are collectively referred to as "scale effects". (Holl and Wislicenus [51]).

Hence, to accurately predict the performance of the prototype from model tests, a thorough knowledge of these scaling parameters and the corresponding scaling laws is required. As a result, a lot of attention has been focused on this particular area of cavitation studies. Two types of flow configurations have attracted the most attention because they are often encountered in many engineering situations. These are (i) the flow around a streamlined body of revolution and (ii) free shear flows. Recent findings made in these two areas will be discussed in Section 1.5 of this chapter. For the time being, the equipment and instrumentation that are presently available for cavitation research will be reviewed.

1.4 Equipment and Instrumentation that Are Currently Employed in Cavitation Research

Recent advances in the development of instrumentation and equip-

ment used in cavitation research have fallen primarily into two categories. The first category is the methods that have been developed for flow visualization and nuclei measurements. The other is instrumentation used in cavitation detection. These will be discussed in turn.

1.4.1 Flow Visualization and Nuclei Measurements

The events occurring in a cavitation process normally take place very rapidly, and this makes flow visualization difficult. High speed motion pictures have been successfully employed as a means of flow visualization for many years. An example is the now classic work of Knapp and Hollander [70] in recording the growth and collapse of bubbles on an axisymmetric body. Arakeri and Acosta [5] succeeded in using the schlieren photography to look at laminar flow separation on the hemispherical nose body. Gates [45] later used the same system to study the effects of transition on cavitation inception on several axisymmetric bodies. The "dual photo technique" developed by Hoyt and Taylor [59] was utilized to look at cavitation in polymer jets. Theirs was one of the first pictures of jet cavitation.

All the above flow visualization techniques provided only a two-dimensional record of the flow field. As a result, much important information about the flow was lost. This problem was overcome with the advent of holography. Among those who have employed holography in cavitation research were van der Meulen [110], Gates *et al* [48] and Peterson *et al* [96]. Recently Katz [65] used a combined schlieren and

holographic technique to study cavitation associated with separated flows. In this technique, a recording of a slightly heated body and flow field is made as in any holographic system. The difference enters during reconstruction of the hologram. A knife edge is used to cut off the main beam during reconstruction, thus leaving only the diffracted beam to be observed. In this way, different parts of the flow could be analyzed at any one time, by correctly positioning the knife edge, without sacrificing the rest of the information. This method has the advantage of reproducing a good image because of little or no background noise.

It is known that nuclei play a very important role in the inception process. However, it is only recently that they are becoming accessible to measurement. The size and density of these nuclei have been measured from holograms of the flow field. This was carried out by Peterson et al [96] and Gates [45]. Unfortunately, this is a very time consuming process. Another method developed by Keller[67] to measure the nuclei population involved a single point light scattering technique. The principle behind the operation of this system is to measure the intensity of the light scattered by single nuclei as they cross a focal volume. The size of the nucleus is then determined from an earlier calibration curve. This method has the advantage that the size distribution is known almost instantaneously. In a comparison test, Gates et al [48] used both the holographic and a light scattering system which is similar in many respects to Keller's [67], to measure the nuclei

population in the freestream region of the LTWT*. They found that the nuclei population distribution measured by these two optical systems do not agree quantitatively. One reason for this discrepancy is the inability to calibrate the light scattering system accurately with known sizes of polystyrene spheres. Also this system does not only register a count of the bubble size it sees, but also records a count in all the size ranges below that particular size. This results in a nuclei count histogram that does not accurately reflect the true size distribution. However, studies are currently being carried out at ARL/PSU** to correct the short comings and the preliminary results show great promise as reported by Yungkurth and Billet [114] and Kohler and Billet [72]. Another system that has been utilized to measure the bubble population density is the acoustic doppler system. This system is described in some detail by Oldenziel [86].

Comparative tests, such as the much reported ITTC tests, (Lindgren and Johnsson[80]) have revealed a poor agreement in experimental results. This apparent inconsistency is not only in the measured inception index but also in the appearance of the types of cavitation. Since these tests were carried out on the same headform but in different facilities around the world, it was concluded that the discrepancy in the results are caused by "scale effects". In-

---

* The Low Turbulence Water Tunnel, Keck Laboratory of Hydraulic Research, California Institute of Technology.

** Applied Research Laboratory, Pennsylvania State University.

disputedly, this is indeed a reason. However, this lack of agreement in the experimental results could also be partly due to different definitions of the inception point by the numerous workers. For example, one investigator observing the flow under strobe-light may call inception at the first sign of a cavity while another may interpret it differently. Recently, workers in this area are becoming more aware for the need of a universal definition for the inception point. To accomplish this, several systems have been developed to detect the onset of cavitation in a quantitative manner.

1.4.2 Detection of the Inception Point

Two systems are currently employed in the detection of the inception point. The first is by acoustical means, developed by a group at St. Anthony Falls Hydraulic Laboratory, and the other is by light scattering. Both systems involve the counting of cavitation events.

In the acoustical method, a pressure transducer is mounted flush on a test body. When a cavitation event occurs, a spike is obtained. Inception is called when the count reaches an arbitrary predetermined number per unit time.

Ellis *et al* [33] and Keller [67] used a light scattering technique to detect the onset of cavitation. In this case, a drop in the light intensity recorded by the receiving optics was taken to correspond to a cavitation event. Again the start of cavitation was denoted when the counted events reached a prechosen value per unit time.

Based on the work of Ellis and Keller, a similar system was developed and tested for use in the LTWT. Just as in Keller's work, a beam of light from a He-Ne laser was adjusted to graze the surface of the test body at the position where inception has been seen to occur. However, the beam used in the present case was expanded 4 times. This was done because it was found from preliminary work that particles and bubbles, not associated with the cavitation inception process, when crossing the path of the unexpanded beam, caused a large enough drop in the light intensity received at the photo sensor to prematurely trigger a count. This problem was overcome with the expanded beam. The expanded beam was eventually focused onto a sensing element.

The photo sensor used was a "HP PIN" diode, and the cavitation events were counted on a frequency counter. A count of 50 events or more per second signaled the inception point. A main setback of the present system was the alignment procedure. Since the sensing area of the PIN diode was approximately 1 mm in diameter, alignment was critical and was often achieved only after great difficulty.

Several other detection systems have also been developed by numerous researchers but their methods are not as widely used as those described above.

1.5 Review of Recent Studies of Scale Effects

1.5.1 Flow around Axisymmetric Bodies

The development of the flow visualization and inception

detection equipment described above has served as an added impetus to cavitation research. Recent scale studies performed with the aid of these instruments will be briefly reviewed. It must be emphasized that the following discussion is not exhaustive.

In the quest to learn more about the scale effects on cavitating flow around axisymmetric bodies, Arakeri [4] and Gates [45] used the schlieren system to study the effect of viscosity on flow separation and flow transition to turbulence. Their work demonstrated the importance of viscous effects on cavitation inception.

Peterson, et al [96] and Gates and Acosta [46] have looked into the scaling problem associated with the nuclei population of the flow. Their holographic studies together with the work of a few other investigators, for example, Keller [67] who used a light scattering technique, represent the relatively few papers on this topic.

Both Gates [45] and van der Meulen [109] looked at the effect of polymer additives on the cavitation inception process. van der Meulen reported finding that the polymer injected appeared to suppress laminar separation on the hemispherical body by initiating a turbulent transition. This resulted in a delay on the onset of cavitation. He also found the polymers had little effect on the Schiebe body; a body which does not exhibit a laminar separation. These findings were independently substantiated by Gates [45].

It was recently suggested that conditions on a prototype could be simulated by distributed roughness on the model. This prompted several investigations on the effect of roughness scaling. Some

of the investigators who have undertaken this task include Billet et al [22], Gates et al [48] and Oldenziel [87]. The group of investigators at ARL discovered that patch cavitation which appeared on axisymmetric headforms and hydrofoils could be controlled by surface roughness. They went on to report on the dependence of the cavitation index on Reynolds number. In general it was found that the cavitation number for a given body size increases with Reynolds number, and increases with decreasing size for a given Reynolds number. Oldenziel discovered that the inception number on a Schiebe body with attached roughness was unaffected by roughness size when the inception point was defined as the instant when the travelling bubble patch reached a length of one cm. This is indeed quite surprising. Obviously, a good deal of work has still to be performed before a more complete picture could be acquired. However, the results reported to date have provided valuable information on this relatively new "scaling effect".

In their effort to explain the onset of cavitation near the surface of axisymmetric bodies, numerous investigators have formulated theories, for example, Parkin [90], Parkin and Kermeen [91], van der Walle [111], Oshima [89] and Johnson and Hsieh [62]. These and other related theories will not be discussed here as they are beyond the scope of the present work. The attention will now be focused on the studies of scale effects on cavitation inception in free shear flows, especially in submerged jets, which is the primary objective of the present investigation.

1.5.2 Free Shear Flows

The study of cavitation in free shear flows, namely, jets and wakes, is of great interest because they are encountered in many engineering applications, such as in the separated flow around propellers and hydrofoils. Shear flows are also found just downstream of gate valves in pipes or in the mixing layers that are formed downstream of control gates in dams (Arndt[13]). However, unlike studies of flow around stream-lined bodies, relatively little is known about such cavitating flows.

Kermeen and Parkin [69] carried out cavitation tests behind sharp edged disks of different diameters. They reported that the cavitation inception number was a unique function of the Reynolds number. However, Arndt and George [10], through their survey of numerous literature, found that although the inception number increased with velocity for all the model sizes, the rate of increase of the inception index with velocity was less for the larger disks than for the smaller ones.

The first person to investigate cavitation inception in jets was Rouse [103]. Since then, numerous other investigators have become seriously involved in the studies. The following table is a partial listing of the investigators and the studies undertaken by them.

Name of Investigator	Scale Effects Studied
Arndt and Arndt et al (8,9,10,12,13)	Air content, jet size, polymer additives

Baker *et al* (14)	Air content, polymer additives
Ball (15)	Jet size
Hoyt (58)	Polymer additive
Jorgensen (63)	Jet size
Lienhard and Stephenson (78)	Jet size, water temperature

Table 1.1. A tabulation of the investigators and the studies performed by them on cavitating jets.

A quick review of the findings of these researchers showed that the measured value of the cavitation number did not seem to exhibit an upper limit. Furthermore, the incipient index for the same jet size, differs considerably from investigator to investigator. To date, no one has succeeded in finding a universal scaling parameter although a few, for example, Lienhard and Stephenson [78] and Arndt [12], have managed to obtain semi-empirical relationships for some of the inception data.

A possible reason for the differing results could be the different nuclei population in the test flows. Few workers have looked into this aspect of the flow. In addition, many workers have failed to document carefully the region in the jet where cavities were first seen, for example, whether inception was in the shear layer between the potential core and the jet boundary or in the region beyond the potential core where the shear layers have merged. It is

possible that the discrepancy in the measured inception index could be due to the fact that the onset of cavitation occurred in different regimes of the jet which are governed by different scaling laws. It is also equally important to look into certain features of the flow, such as the exit condition of the jet and the spread rate, as these may provide insights into the initial vortex roll-up and the size of the coherent structures, which could in turn affect the cavitation inception process.

In brief, in order to achieve an understanding of the scale effects and the scaling laws that govern cavitation in shear flows, one must not only carefully study the environment but must also look into the fluid dynamics of the flow.

1.6 Scope of the Present Work

The points raised above are only some of the questions that need to be considered and answered. It was with these thoughts in mind, that the present study was undertaken. The aims of the present work were two-fold. The first was to measure the cavitation inception number of jet flows under widely different flow conditions. Four parameters were considered. They were (i) jet size, (ii) dissolved air content, (iii) nuclei population and (iv) jet velocity. The second aim, of course, is to draw these observations together in some meaningful way.

Flow visualizations were made with schlieren photography as well as holography. Holography was also used to determine the nuclei

population in the various regions of the jet. A method was devised to measure the pressure fluctuations in the jet. This method in brief, uses well-characterized air bubbles as pressure sensors.

The results of all these measurements will be presented and discussed in later chapters together with an interpretation.

2. DESCRIPTION OF THE EXPERIMENTAL APPARATUS AND INSTRUMENTATION

2.1 General Description

The experimental objectives required an experimental setup wherein a jet of water could be discharged and made to cavitate under prescribed conditions. This not only called for a reservoir of water which could be treated to meet the test requirements, for example, deaerating the water to the desired air content, but also an environment where the flow could be observed. The LTWT* was chosen as the experimental setup because it met the above requirements.

In the present work, the jet was created by discharging tunnel water itself from a pressure vessel through a contoured nozzle into the center line of the LTWT. Cavitation inception in the jet was brought about by lowering the pressure in the tunnel while maintaining a constant jet exit velocity. Onset of incipient cavitation in the jet was detected by a microphone placed against the top window of the tunnel. Two optical systems were used for flow visualization. These were the holocamera and the schlieren system.

A general view of the experimental apparatus is shown in Figures 2.1. To facilitate presentation, the various components that make up the apparatus are discussed separately, commencing with the familiar LTWT.

---

* see Section 2.2 to follow

2.2 Low Turbulence Water Tunnel (LTWT)

This facility was described in great detail by Gates [45], and it will be redundant to repeat that description here. For the present work, it is sufficient to say that the pressure in the tunnel could be lowered by the action of a vacuum pump. The side windows of the 8 1/3 ft test section are made of ground and polished plate glass thus facilitating flow visualization. The tunnel is also equipped with a filter system and this permits the water in the tunnel to be kept clean.

One of the aims of the present work was to study the effects of air content in the water on cavitation inception. This required running tests at different air content, from nearly saturated water to water with very low air content. When Gates performed his tests, the method he adopted in reducing the air content was to cavitate the tunnel, stop it, then bleed the lines. This was repeated over a period of many hours. He reported achieving an air content of 7 ppm after operating for 16 hours in this manner. This method was not only undesirably time consuming, but it was difficult to attain an air content of much less than 7 ppm. For this reason, a deaerator system was designed and installed recently as part of the LTWT. The following is a detail description of this unit.

2.3 Deaerator System

Figure 2.2(a) is a schematic diagram of the deaerator system, while Figure 2.2(b) shows a photograph of the deaeration tank. The

main component is a closed cylindrical vessel measuring 2.54 m (100") in length and 0.91 m (3 ft) in diameter. Water is pumped (by the supply pump) to the top of the tank from the water tunnel. The water is then forced through a set of 10 "Bete Spiral Nozzles", Model #TF28FC, mounted on a horizontal section of the pipe, suspended inside the tank, from the top. These commercially designed nozzles effectively atomize the water. The fine sprays then rain down on a packed bed of "Plastic Super Intalox" tower packings resting on a steel grating stretched across the entire length and width of the tank. This is aimed at increasing the surface area from which gas diffusion can take place. The water flows through the packed bed and collects at the base of the tank where a second pump returns the water back to the tunnel. The deaeration process begins when the pressure inside the vessel is reduced by a vacuum pump.

During deaeration, the tunnel water is continuously circulated through the deaeration vessel. It is desirable to prevent flooding of the packed beds because this will drastically reduce the surface area for gas diffusion. Therefore, there is a need to be able to adjust the water level in the vessel. This is accomplished by throttling the flow on the supply and drain lines to the tank until the desired water level is achieved.

To prevent the drain pump from running dry, the drain pump automatically kicks off when the water level in the tank becomes too low. A check valve in the drain line stops any back flow into the tank. This pump remains shut off even though the supply pump is

still operating, until the water level rises to a predetermined level. By the same token, the supply pump shuts off when the water level in the tank becomes too high or overflooding will occur. The supply pump comes on again when the water drops to a safe level. These "ON-OFF" actions of the two pumps are controlled by a 4-level "Gems Level Switch", Model #LS800, mounted on a side viewing glass, and a set of latched relays. When the water level in the tank is properly adjusted, both pumps will run continuously throughout the deaeration process.

The present deaeration system can circulate 200 gpm. It has been found that at this flow rate, the deaeration time was reduced when the water tunnel was kept at a partial vacuum. Figure 2.3 shows the performance curve of the present system at two different tunnel pressures. It should be pointed out that the lower curve represents the limit of the present system because further reduction of the tunnel pressure would soon cause the supply pump to cavitate. The air content is measured with a Van Slyke Blood Analyzer.

The present deaerator thus allows an easy control of the air content in the tunnel water.

2.4 Flow Apparatus

The flow apparatus is made up of a cylindrical pressure vessel and a nozzle assembly. This is shown schematically in Figure 2.1 . The pressure vessel is 0.3 m in height and approximately 1.22 m in width. A small pump is used to pump water from the water tunnel to

this vessel, and the tank is pressurized with the Institute compressed air supply. The inlet pressure is regulated with a pressure regulator and can be varied from 5 psig to 85 psig. If desired, the water in the pressure vessel can be heated. This is done by circulating the water through a heat exchanger (which consists of a coil of copper tubing sitting in a hot water bath.) which is located upstream of the vessel. The flow rate through the nozzle is measured by a "Flotech" turbine flow meter which is placed on the discharge side of the pressure tank. The pressure vessel is connected to the nozzle assembly which is mounted on the top window on the tunnel by a 1.9 cm (0.75 inch) I.D. pressure hose. A ball valve in the line allows the flow in the jet to be shut off in between runs.

The nozzle assembly is made up of five different sections. They are (i) a 0.25 m (9") straight vertical section of pipe, (ii) a vaned long radius elbow to assist in turning the flow through a right angle, (iii) a honeycombed section of pipe downstream of the elbow, (iv) a settling chamber, and (v) a circular nozzle. The geometrical details of the nozzle assembly are shown in Figure 2.4. These various parts will now be described.

The elbow contains 2 vanes made up of cut out brass sheets of 0.76 mm (0.03") thickness. They are equally spaced and are held in place by wedging them in the inner walls of the elbow. The elbow is welded at one end to the short vertical section of pipe and the other end to the honeycombed section. The honeycomb sits in a shouldered region and is

prevented from being washed downstream when the settling chamber is in position. The settling chamber could be unscrewed from the honeycombed section, thus revealing the honeycomb. This facilitates the cleaning and replacement of the honeycomb. Finally, nozzles of different sizes can be attached to complete the assembly. Three different nozzle sizes were used. They were 3.17 mm (0.125 inch), 4.76 mm (0.188 inch) and 6.35 mm (0.25 inch) in diameter. The shape of a typical nozzle used in the present work is illustrated in Fig. 2.5.

2.5 Electrolysis Bubble Production

Electrolysis bubbles have been used in the past by numerous investigators for flow visualization. In the present studies, electrolysis was used to alter artificially the nuclei population in the jet to levels which are well above what is normally found in water.

A 1.59 mm O.D. tungsten rod was used as the electrode. It was completely insulated with "heat shrink" tubing with an exception of about 0.5 mm of the pointed tip. The electrode was inserted into the nozzle assembly through a hole bored in the vaned elbow (see Figure 2.4) and positioned on the center line of the flow. The tip of the electrode was adjusted to be approximately 4 nozzle diameters upstream of the nozzle exit. A length of insulated wire connected the electrode to the negative terminal of a D.C. power supply. The other terminal was grounded to the tunnel. In this configuration, hydrogen bubbles were generated at the electrode. By varying the current to the electrode, different nuclei populations in the flow were artificially created.

2.6 Inception Detection System

Figure 2.6 is a diagrammatic layout of the detection system employed in the present studies. The sensor was a microphone pressed against the window of the tunnel and placed directly above the cavitating region. The microphone was insulated from surrounding noises. On cavitation inception, the noise generated by the exploding and collapsing cavities was picked up by the microphone. The signal from the microphone was then fed through the preamplifier section of a commercial tape deck. From the preamplifier, the amplified signal was band passed by a "KRONHITE" band pass filter set in the range of 1.9 to 2.1 kHz. The output from the tape was also monitored by a pair of headphones to ensure that the signal picked up by the microphone was that of a cavitating jet at inception and not of some other sources. The filtered signal was further amplified by a variable gain amplifier. In the present work, the gain of the amplifier was set at 7. The signal was finally fed into a frequency counter. When a count of 5 per sec or more was noted, inception was called. All inception data were obtained this way.

In addition to measuring the incipient cavitation number under different flow conditions, it was desired to observe the flow. Flow visualization was accomplished with the aid of the holocamera and the schlieren system. This equipment will now be described.

2.7 Holocamera and Reconstruction System

The present holographic system is a completely new design by Katz [64]. The various components in the holocamera are shown in

Figure 2.1. The principal unit is a ruby rod measuring 7.62 cm (3.00 inch) in length and 0.6 cm (0.25 inch) in diameter. The ends of the ruby rod are highly polished plane surfaces. Excitation of the ruby is brought about by a helical xenon flashlamp. Cylindrical aluminum reflectors which cover the flashlamp are used to reflect the light from the flashlamp into the ruby rod. Cooling of the ruby rod-flashlamp is accomplished by continuously recirculating deionized water through this assembly during operation.

The optical cavity is formed by placing two flat surface mirrors on both sides of the ruby rod-xenon flashlamp assembly. They are held parallel to each other. The back mirror (component 3 in Fig.(2.1)) is a 100% reflecting dielectric surface, while the front mirror is sapphire ethalen and is only 60% reflecting. The front mirror also assists in the longitudinal mode control of the laser. Transverse mode control is achieved by two iris apertures (components 4 and 13) placed in the optical cavity.

When the flashlamp is triggered, about 1 kJ of energy is discharged through it. When the optical cavity is open, the resulting light emitted by the ruby rod races back and forth between the two mirrors and at each passing, more electrons in the ruby are excited. Hence a population inversion is created and eventually results in the lasing of the ruby rod. Since the duration that the flashlamp is on is much longer than that for a single lasing of the ruby, numerous light pulses are generated in a single flash of the flashlamp. This is quite undesirable because it causes multiple exposure to the

holographic film. For this reason, the cavity has to be "Q switched". "Q switching" is accomplished by a KD*P cylindrical ring electrode pockel's cell and a calcite glan polarizer. This process works as follows:

Light emitted by the ruby is first polarized by the glan polarizer. It then enters the KD*P crystal. A high voltage is applied to the crystal so that the angle of polarization of the incoming light is turned through 45°. After exiting from the pockel's cell, the light is reflected back by the mirror into the cell again. On this second passage through the cell, the polarization angle is rotated through another 45°. When the reflected light reaches the polarizer, it is now rotated through 90° to its original polarization angle and thus not permitted into the ruby. Population inversion is thus avoided and no lasing occurs. In short, when the pockel's cell is on, the optical cavity is closed.

When the voltage to the pockel cell is dropped to zero, the cavity is effectively open to light oscillations which results in the eventual lasing of the ruby. Hence the idea is to drop the voltage to the cell for a sufficiently long time during the flashing of the xenon lamp so that the ruby is allowed to lase only once (or twice, if double pulsing is desired). This is accomplished by setting a delay time on the power source to the pockel's cell. The delay time here is defined as the time that elapsed between the instant the flashlamp is triggered to the instant the voltage to the cell is dropped to zero. The right setting of the delay time is obtained through trial and

error and is usually around 800 μs. It should be pointed out that the duration of the laser pulse is between 20 to 50 nanoseconds.

A beam splitter directs about 4% of the beam emitted from the cavity into a pin diode which monitors the output of the laser. The remaining beam passes through a microscope objective which expands the beam. The resulting beam is spatially filtered by an 11 μm pin hole and finally collimated. The collimated beam is used to illuminate the sample volume. A camera placed on the opposite window of the tunnel is used for recording the images. The recording film used is 70 mm Agfa Gevaert film.

Holograms obtained are then reconstructed in the reconstruction system. This system is illustrated in Figure 2.7. The hologram to be examined is mounted on an x-y-z vernier carriage and is illuminated by a 5 mW Spectra Physics He-Ne laser. The beam is expanded and collimated in the same manner as in the holocamera. The reconstructed image is magnified 220 times with a microscope objective and imaged on a videcon. This magnified image is then displayed on a closed circuit TV monitor. The sizes of the nuclei are read directly off the screen of the monitor with the aid of a reticle.

2.8 Schlieren System

A comprehensive description of the present schlieren system is found in the thesis by Gates [45]. A schematic drawing of this system is shown in Figure 2.8. Basically, the light source was generated by discharging two 0.05 microfarad, 10 kV capacitors through a tungsten

electrode. The duration of the spark was about two microseconds thus permitting photographs of the instantaneous flow field under observation to be recorded. The light emitted from the spark source was collimated by a 12 inch focal length lens and was directed across the test section of the water tunnel. In the present work, the required "schlieren effect" was created by heating the water in the jet to about 2° to 4° C above the temperature of the surrounding fluid. It is worth mentioning that preliminary work showed that a jet heated to only 1° C above the ambient liquid could also be photographed. However, poor contrast on the recording film was observed especially at distances far downstream of the jet exit. Photographs of "Epsom salt solution" jets (0.5 percent concentration) were also taken when high contrast was desired.

The scattered light emerging from the test section was then focused onto a knife edge. The edge was adjusted to block a major portion of the beam. Two knife edge positions were used: (i) with the cutting edge parallel to the direction of flow and (ii) with the edge perpendicular to the flow direction. The image was finally recorded on Kodak 4x5 "Royal-X-Pan" film. Due to the size limitation of the recording film, most of the photographs were taken at low image magnification (approximately 3) to enable a larger portion of the jet to be recorded.

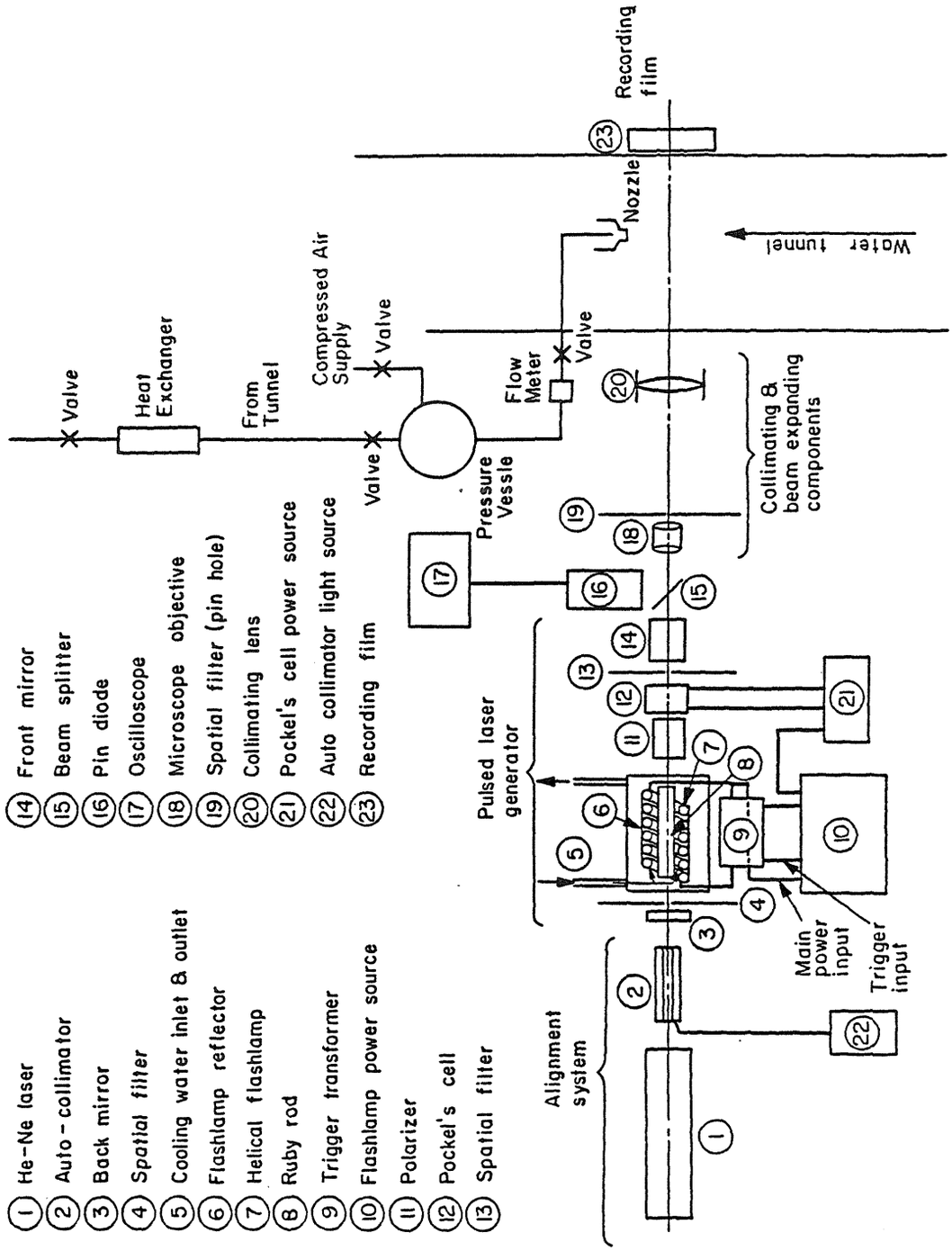

Fig. 2.1. Diagram showing the layout of the experimental apparatus.

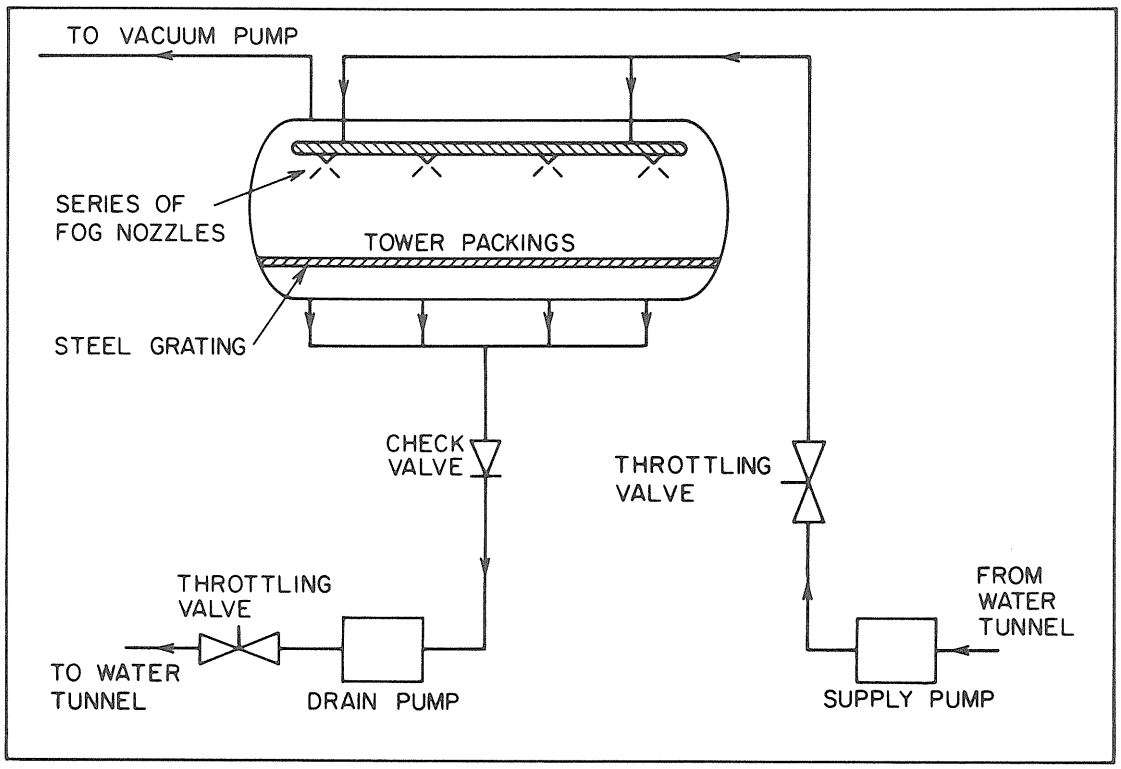

Fig. 2.2(a). Schematic diagram of the dearator system.

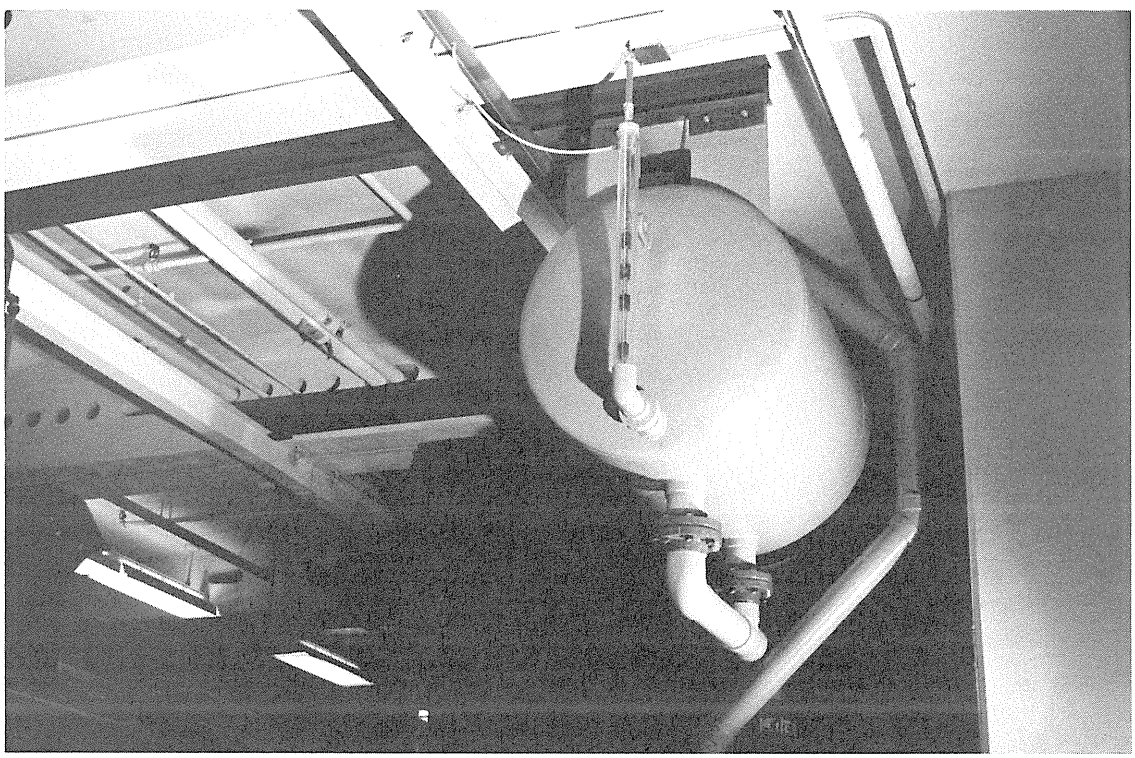

Fig. 2.2(b). Photograph of the dearation tank.

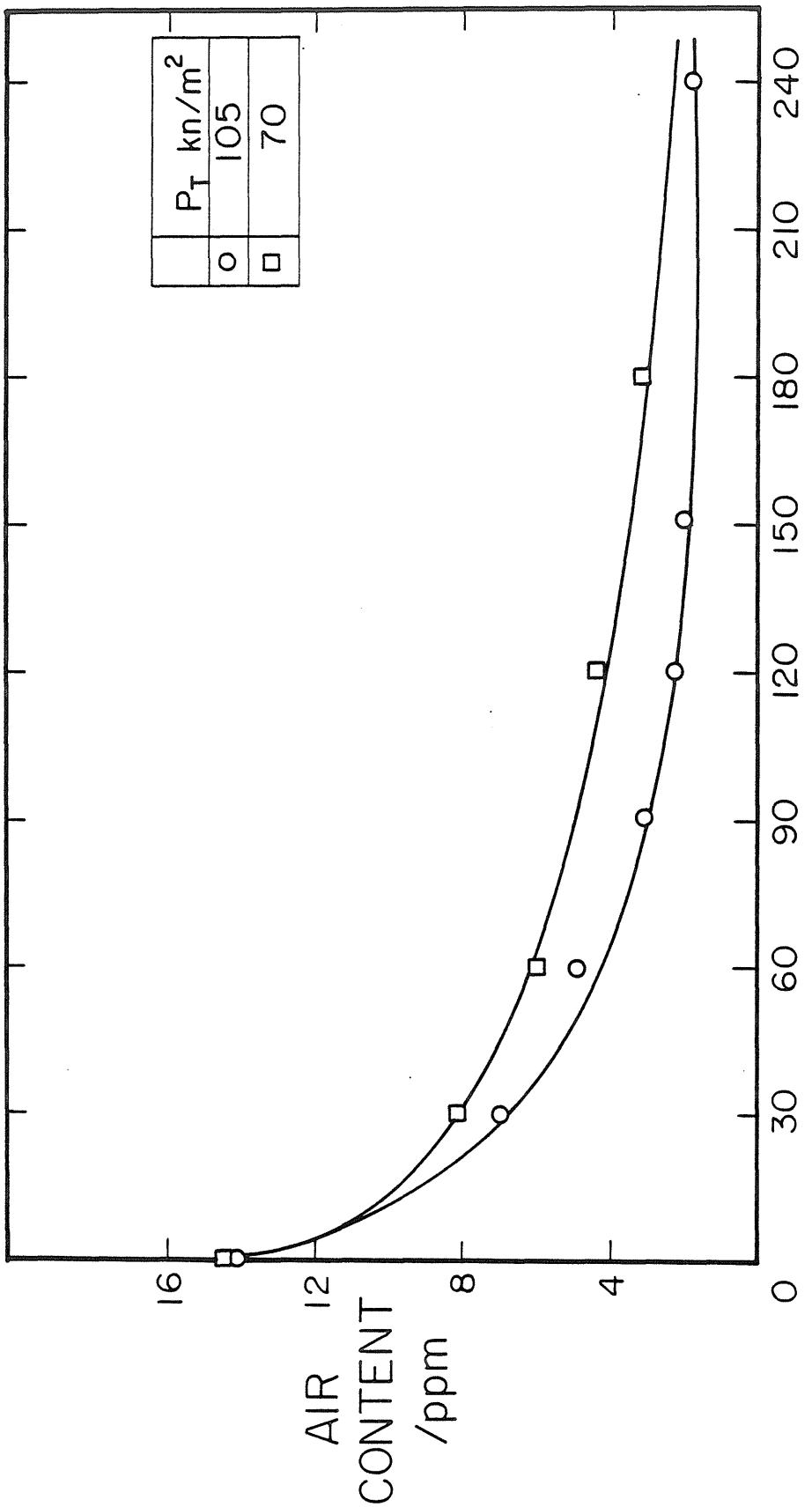

Fig. 2.3. Graph displaying the performance curve of the deaeration system.

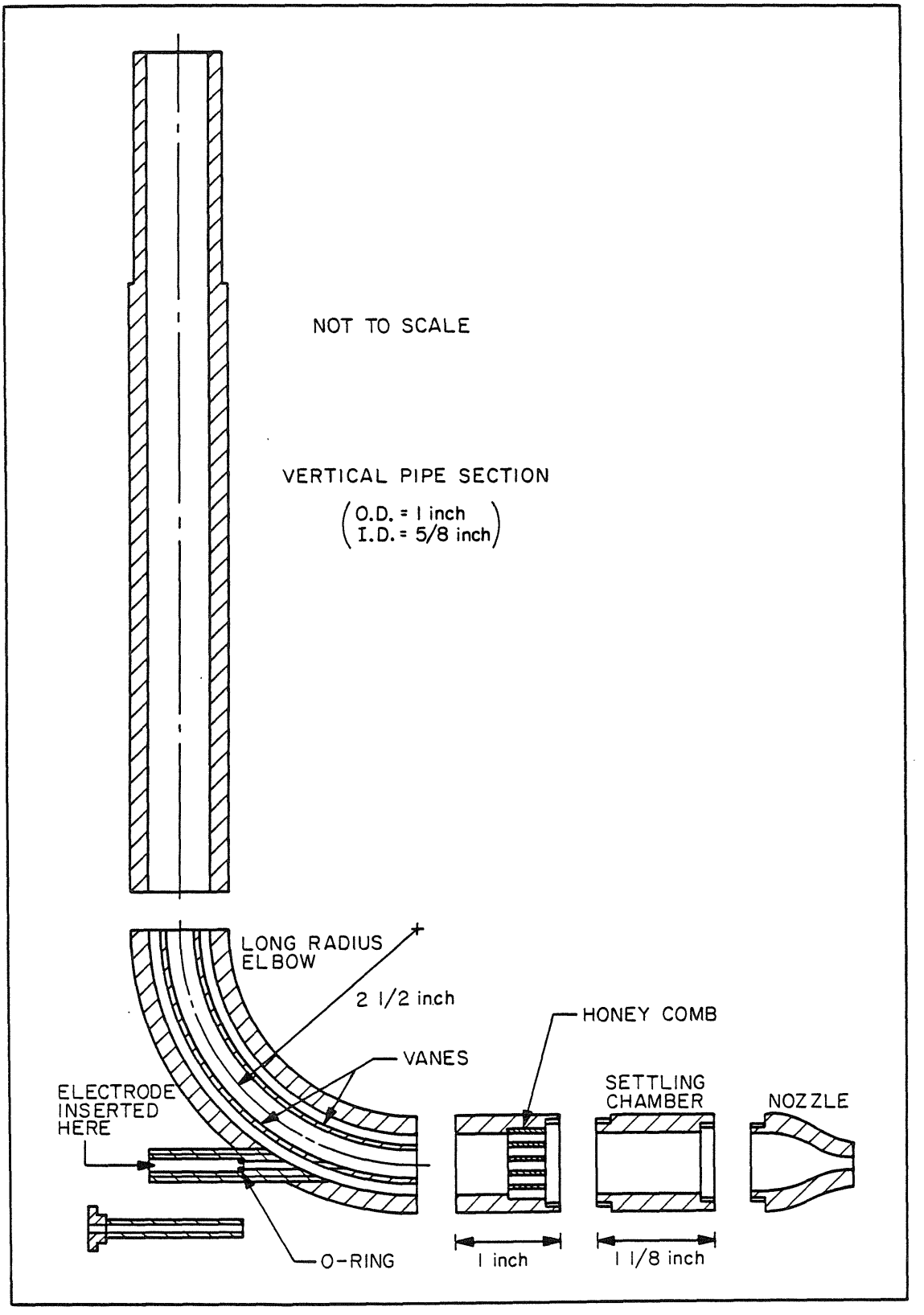

Fig. 2.4. Diagram showing the geometrical details of the nozzle assembly.

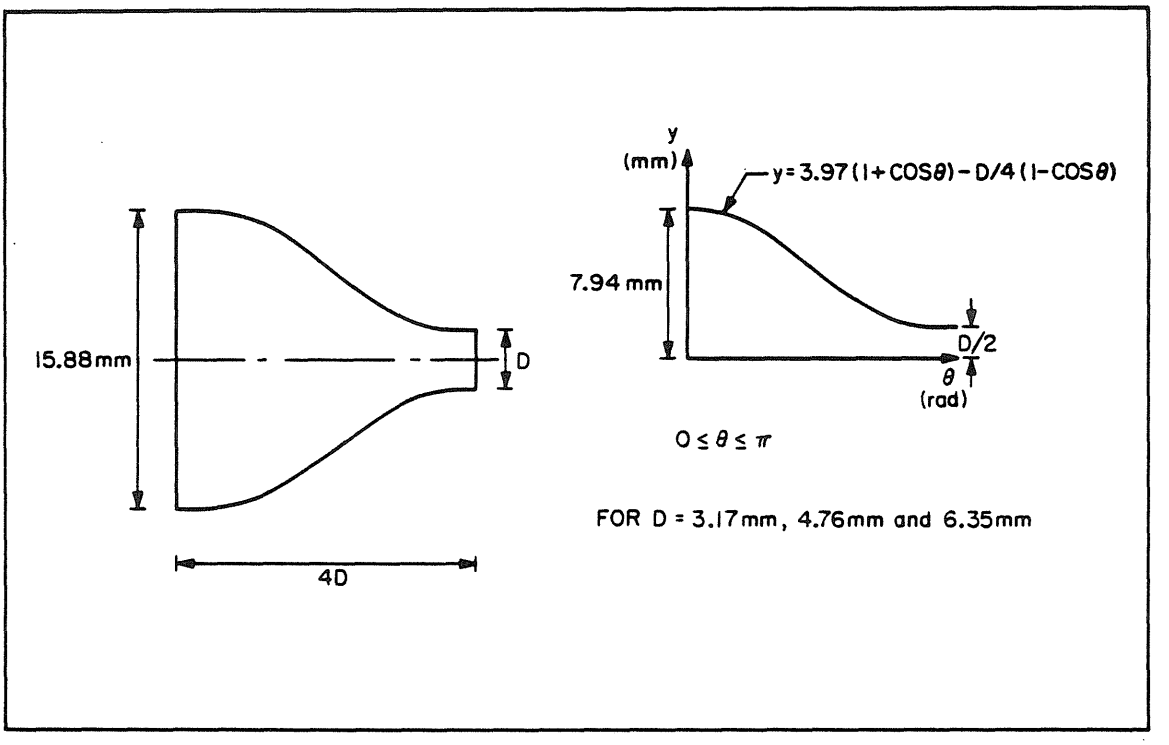

Fig. 2.5. Diagram illustrating the geometrical shape of the nozzle.

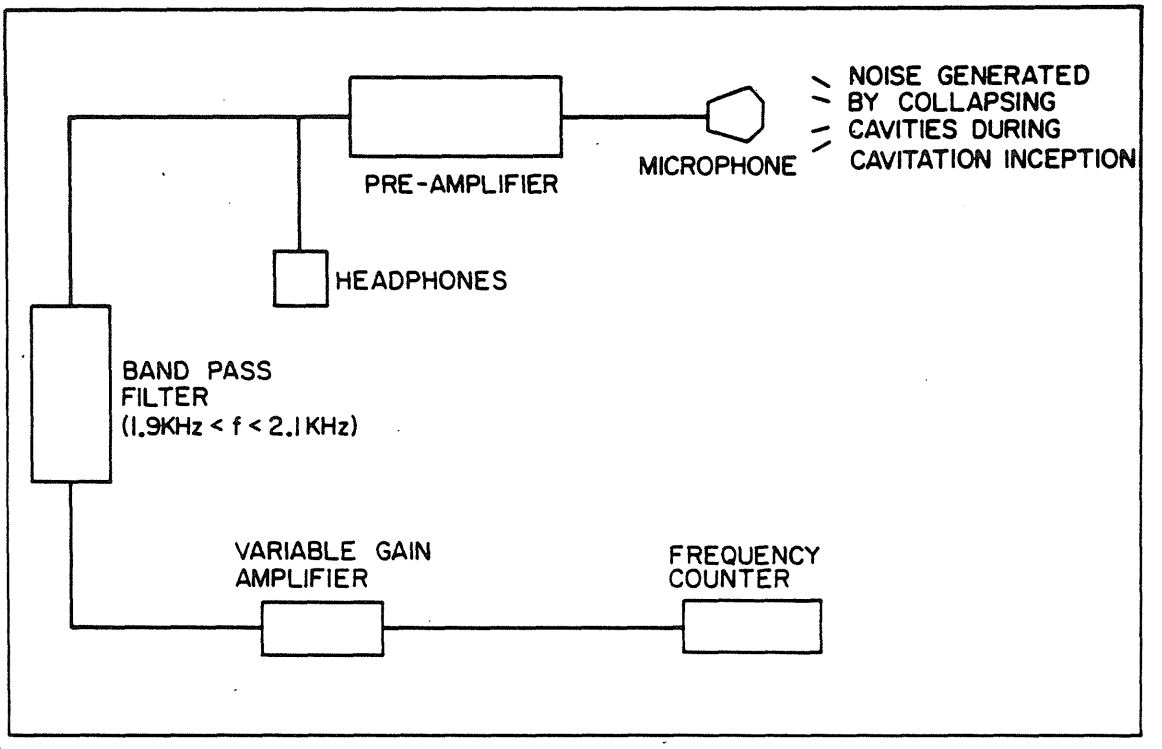

Fig. 2.6. Schematic drawing of the cavitation inception detection system.

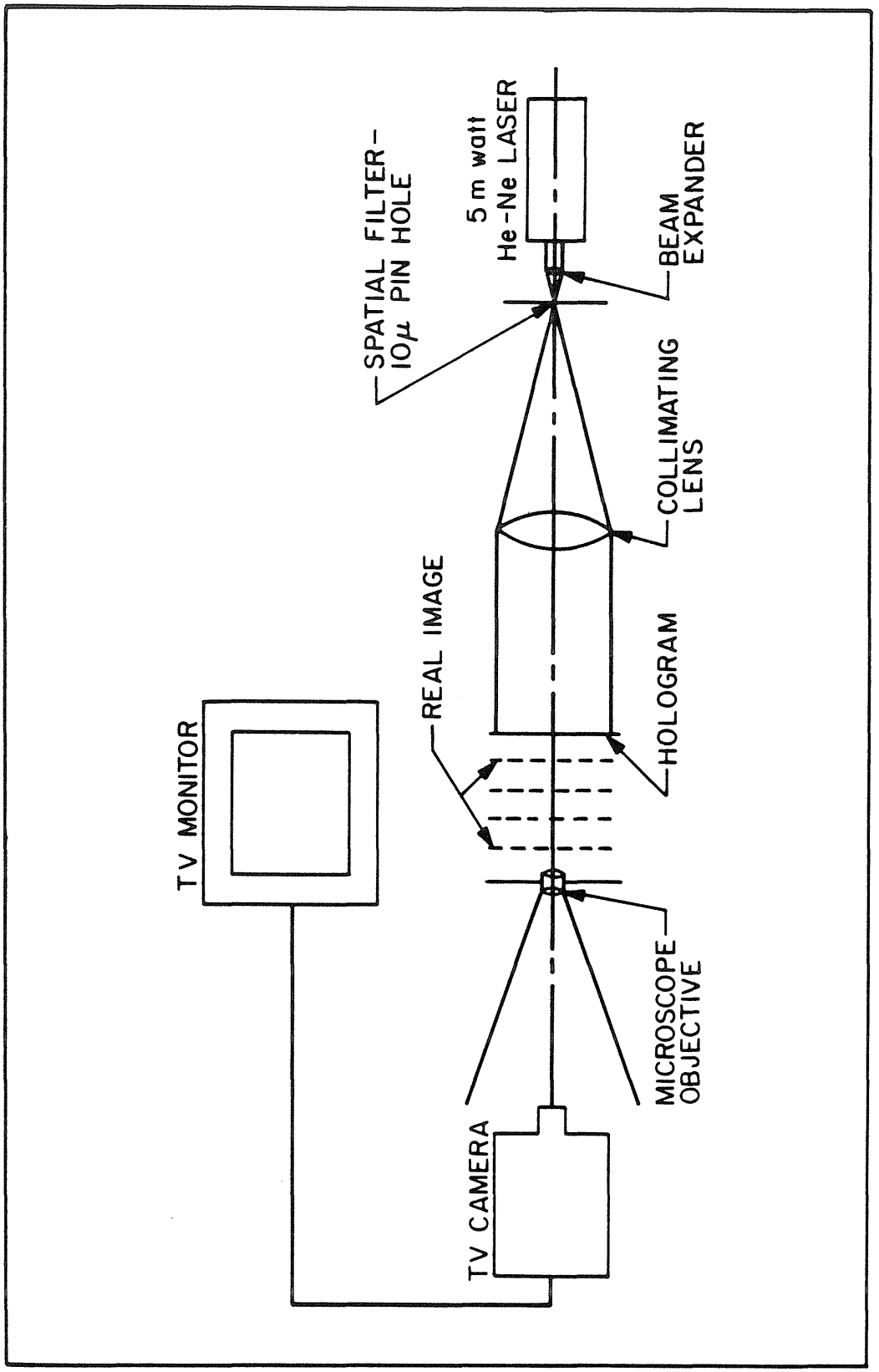

Fig. 2.7. Diagram of the holographic reconstruction system.

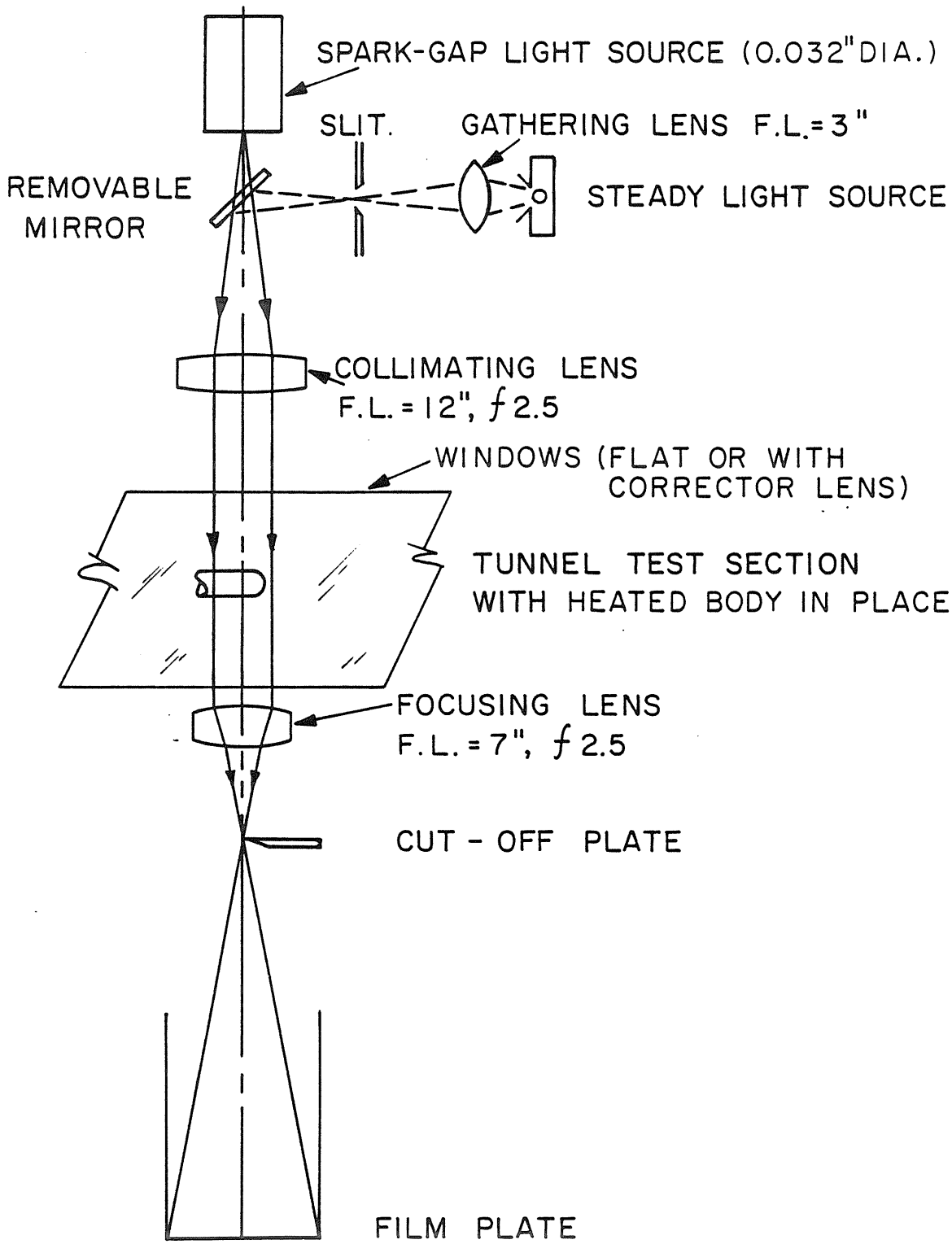

Fig. 2.8. Schematic drawing of the schlieren system (Gates 1977).

3. EXPERIMENTAL PROCEDURES AND MEASUREMENT TECHNIQUES

3.1 Introduction

The experimental procedures followed during the course of the present studies are described in this chapter. The experimental objectives called for the measurement of the incipient cavitation indices under different flow conditions. For each nozzle size, the cavitation index was measured as a function of (a) the dissolved air content of the water, (b) the exit velocity of the jet and (c) the nuclei population in the jet. The nuclei population in the jet was altered by seeding the flow. Three nozzle sizes were investigated. They were 3.17 mm, 4.76 mm and 6.35 mm in diameter.

Flow visualization was also carried out. This was accomplished by holography and schlieren photography. Furthermore, the flow was observed under strobe light. In addition, the effect of the dissolved air content on the nuclei population density was studied with the aid of the holocamera. Prior to the actual data acquisition and flow observation, several preliminary preparations had to be performed. These preliminary steps taken are described first, followed by a description of the measurement techniques employed.

3.2 Preliminary Preparations

The nozzle assembly was mounted on the top window of the test section of the LTWT as shown in Figure 3.1. It was positioned such that the axis of the nozzle was on the center line of the water tunnel.

The tungsten electrode used for "electrolysis seeding" was inserted into the elbow of the nozzle assembly, and was adjusted until the tip was about four nozzle diameters from the lip of the nozzle. The tunnel water was then filtered for six hours. This was followed by deaerating the water to the desired test condition. The microphone used for cavitation detection was placed against the window of the tunnel such that it was directly above the cavitating regime of the jet.

On completion of these preliminary preparations, the data acquisition process began.

3.3 Measurement of the Incipient Cavitation Index

Some water from the water tunnel was pumped into the pressure vessel. Pressurization of the vessel was accomplished with the Institute compressed air supply. The inlet pressure to this vessel was regulated with a pressure regulator. A jet of water was then discharged into the stationary tunnel sitting at an ambient pressure of approximately 0.9 atmospheres (13 psia). The pressure in the tunnel was then quickly lowered until cavitation inception in the jet occurred. As explained earlier, inception was called at the instant 5 events per second or more were indicated by the detection system. The pressure in the tunnel and the exit velocity of the jet at inception were noted. From these measurements, the incipient cavitation index was calculated from the expression below:

$$\sigma_i = \frac{(P_T - P_V)}{\frac{1}{2}\rho V_j^2}$$

where P_T = the pressure in the tunnel when inception was called

P_V = vapor pressure of water evaluated at the bulk temperature of the water

ρ = density of water

and V_j = exit velocity of the jet.

The tunnel pressure was raised to its initial value and allowed to sit at that pressure for about 30 seconds before similar runs were performed.

The incipient index was also measured when the flow was seeded. Seeding was done by electrolysis of the water and the following currents were used to create different nuclei populations: 0.05 mA, 0.1 mA, 0.2 mA, 0.4 mA, 0.6 mA, 1.0 mA, 2.0 mA, and 5.0 mA.

All the above tests were repeated over a range of jet velocities. Different velocities in the jet were realized through pressurization of the vessel to different values and not by flow throttling.

For each nozzle size, the above-mentioned tests were carried out sequentially with the tunnel water at different levels of air saturation. Jet water with the following dissolved air content was investigated: 14.1 ppm, 10.9 ppm, 7.7 ppm and 4.2 ppm. (Saturation is at 15 ppm.)

The incipient cavitation index corresponding to a particular flow condition was obtained by averaging the results of ten similar runs.

3.4 Flow Visualization and Nuclei Measurements

The flow was observed under stroboscopic light as the jet was brought to cavitation inception and beyond. In addition, schlieren photography was also employed to give a permanent record of the flow observation. Two sets of schlieren photographs were obtained. The first set was taken with the cutting edge of the cutoff plate parallel to the direction of flow, while the second set was with the edge perpendicular. Although these photographic records gave valuable information such as the spread rate of the jet and the location of the cavities of inception, they provided no clue to the miroscopic nuclei population in the jet. This is a major setback since such information would definitely give a better insight into the cavitation phenomena in jets on a whole. This shortcoming was overcome with holographic studies.

As a result of some preliminary work, it was found that with the present in-line holography setup, holograms of heated jets could not be reconstructed and studied. This was because the reference beam itself was scattered by the density field, even though the water in the jet was heated to only 1/2° C above the surrounding water. (Ooi and Katz [88]) Consequently only holograms of unheated jets were obtained and analyzed.

The three flow visualization techniques employed above were performed for all the flow conditions previously mentioned in Section 3.3.

A new method was devised to measure the pressure fluctuation in the present jets. The motivation for this study and the measurement techniques used are presented in the next chapter.

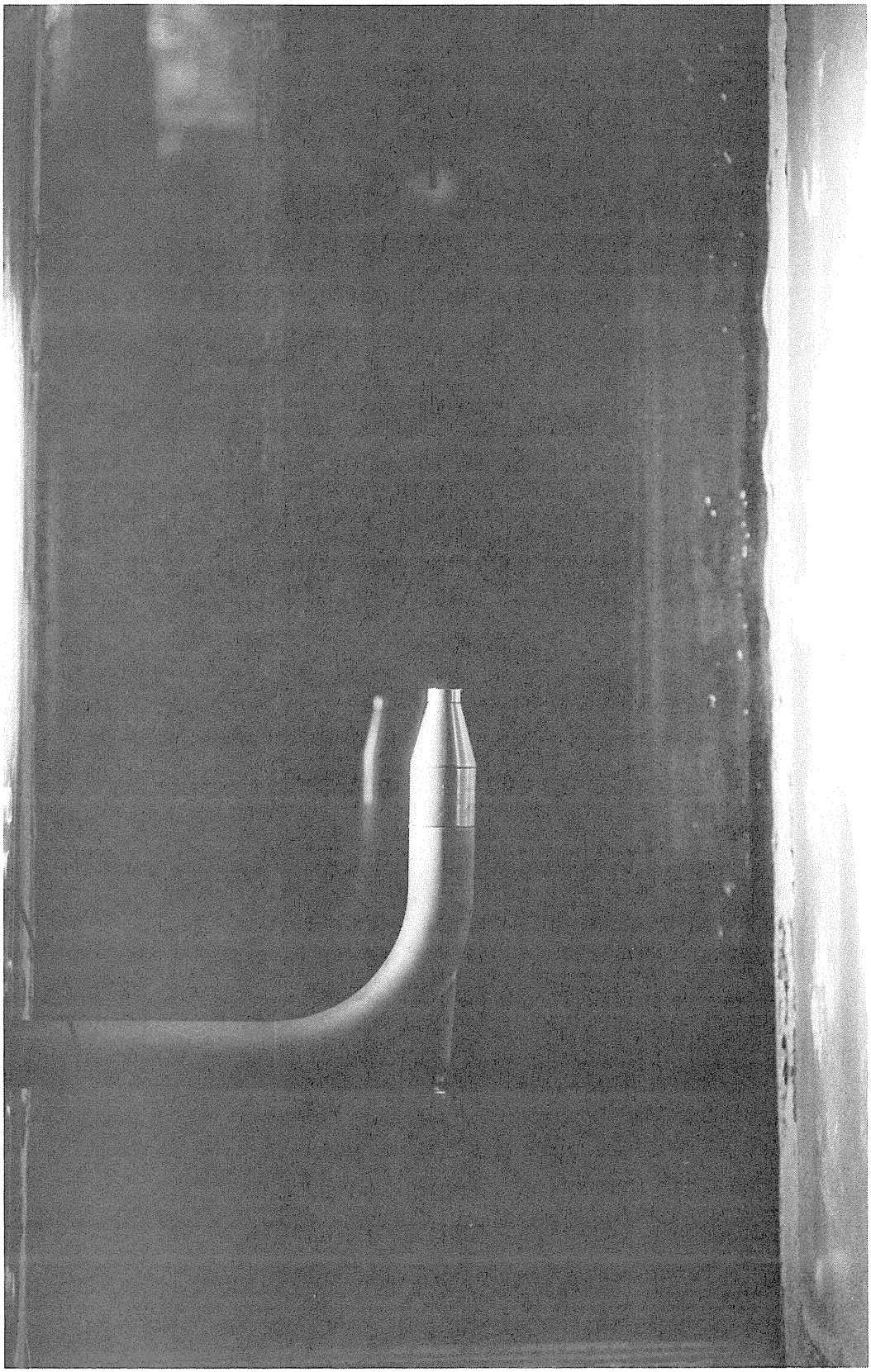

Fig. 3.1. Photograph showing the mounted nozzle assembly on the top window of the water tunnel.

4. MEASUREMENT OF PRESSURE FLUCTUATIONS IN WATER JETS

4.1 Introduction

Since the pioneering work of Rouse [103], the study of cavitation in water jets have been actively pursued. The cavitation inception numbers have been measured by numerous investigators, for example, Hoyt [58], Lienhard and Goss [79] and Jorgensen [63]. Although the measured indices were quantitatively different, the results of these researchers nevertheless indicated that cavitation inception always occurred at a mean pressure which was considerably higher than the vapor pressure of the liquid. Obviously, this observed fact was in direct contradiction to the long held belief that cavitation would only occur if the pressure is at or below the vapor pressure. To explain this discrepancy, it was postulated that local pressures at numerous positions in the jet dip to or below the vapor pressure due to pressure fluctuations. This will consequently give rise to cavitation inception. If this is indeed the case, the departure of the instantaneous local pressure from the mean would be enormous.

One of the first attempts to experimentally determine the pressure fluctuations in axisymmetric jets was carried out by Rouse [103]. His work was later extended by Sami et al [105]. Barefoot [16] made similar measurement and although his measured values were substantially different from those reported by Sami et al [105], the data followed the same general trend. Other workers who have reported work on pressure fluctuations or spectra measurements include Fuchs [41, 42], Arndt and George [10] and Lau et al [76]. All the above

measurements were made in air jets by introducing a pressure transducer or a microphone into the flow.

The highest rms pressure fluctuations ever recorded was about 22 percent of the dynamic head of the jet (Sami et al [105]). These measurements are themselves insufficient to account for cavitation inception in some jets, where it has been reported that the measured incipient index could be as high as 3 in a 13 cm jet (Lienhard and Goss [79]). In other jets, the occurrence of inception could only be explained if the peak pressure fluctuations are at least several factors higher than the measured rms values. Arndt and George [10] have stated that the peak to peak values of pressure fluctuations could be as much as ten times the measured rms.

In view of the above discussion, it is understandable that there is a need to determine if such high pressure fluctuations occur in the jets that are presently investigated. Since these jets are relatively small in size (the largest is only 6.35 mm), the normal approach of measuring with a pressure transducer is not suitable. Hence there is a need to devise a way to measure the pressure fluctuations.

It is known that when a bubble is subjected to a pressure field, it will deform in shape and volume accordingly. If this bubble is designed to meet certain requirements, which will be considered shortly, it can serve as a good pressure sensor. In principle, the pressure field in the jet could then be mapped out by following the bubble as it traverses the jet. The theory behind the idea of using

such a bubble as a static pressure sensor is considered in the next section.

4.2 Theory Behind Static Pressure Measurements Using Bubbles as Pressure Sensors

The equation governing the motion of a spherical bubble is given by the familiar Rayleigh-Plesset equation (Plesset and Prosperetti [98]) viz,

$$R\ddot{R} + 3/2\dot{R}^2 = \frac{1}{\rho}\left[P_g(T) + P_v(T) - P_\infty(t) - \frac{2S}{R} - \frac{4\nu\dot{R}}{R}\right]$$

Rewriting, we have

$$P_\infty(t) = \left[P_g(T) + P_v(T) - \frac{2S}{R} \frac{4\nu\dot{R}}{R}\right] - \rho\left[R\ddot{R} + 3/2\dot{R}^2\right] \qquad (1)$$

For a given bubble size, the static pressure in the jet at any instant can then be computed from the above equation once $\dot{R}$ and $\ddot{R}$ are known. In addition, if the bubble is designed to have a response time that is short in comparison to the time scale of the typical pressure fluctuations, then the inertia and the viscous terms in the Rayleigh-Plesset equation can be neglected as shown in Appendix 1. Equation (1) then simplifies to:

$$P_\infty(t) = P_g(T) + P_v(T) - \frac{2S}{R} \quad . \qquad (2)$$

In theory, the instantaneous pressure at various positions in the jet can then be computed from a continuous photographic record of the size of a bubble as it crosses the jet from a reference point. In practice this is more difficult to achieve since the events are occurring at a high speed. Furthermore, even if somehow one succeeded in tracing the path of the bubble under observation, the pressures indicated by the bubble correspond to different instants in time. Consequently, one would not have the true view of the pressure field in the jet at any one instant.

Consider a string of bubbles always of the same size at the point of injection, which is being continuously introduced into the jet at a reference position. An instantaneous photograph would then reveal the sizes of the bubbles at various positions in the jet. Any change in the bubble size from the reference size could be interpreted to be due to deviation of pressures from the mean. If P_{g_o} is taken to be pressure of the gas in the bubble at the point of injection, then the pressure of the gas at some position, x, is given by

$$P_{g_x} = P_{g_o} \left(\frac{R_o}{R_x}\right)^{3\gamma}$$

where R_o and R_x are the radii of the bubble at the reference point and at position x , respectively, and γ is the polytropic index. The instantaneous pressure at point x can then be computed from:

$$P_{\infty_x}(t) = P_{g_o} \left(\frac{R_o}{R_x}\right)^{3\gamma} + P_V - \frac{2S}{R_x} \qquad (3)$$

In this manner, an instantaneous record of the presssure field across the entire jet could be determined. Furthermore, this measuring technique has the added advantage that the "probes" do not cause a significant flow disturbance.

As mentioned earlier, the bubbles can serve as good pressure sensors only if they are tailored to meet certain requirements. These requirements are summarized below.

4.3 Summary of Requirements

It has been mentioned that the technique adopted required a string of bubbles of a uniform referenced size. Also, in order for the bubbles to be good indicators of the instantaneous pressure, there should be no lag time in the response to a sudden pressure change. This implies that the response time of the bubble should be at least an order of magnitude faster than the typical time scale of the pressure fluctuations.

The bubbles are also required to be small enough so that the pressures they see are a good approximation of the local "point" pressures. However, they should not be so small that the change in volume could not be easily and accurately determined. Fuchs [43], Michalke and Fuchs [82], and Lau *et al* [76] were among the relatively few who have measured the pressure spectra in jets. Their work demonstrated that the dominant portion of the spectra was shifted to lower frequencies with increasing distance from the nozzle exit. The results of the three groups of investigators mentioned above also showed that the normalized power spectra peaked at a Strouhal number

(defined as $\frac{fD}{V_j}$) of 0.45, and beyond that the spectra dropped rapidly to insignificant values. Barefoot [16] also reported comparable results. This meant that in the present jets, the frequency of the dominant portion of the pressure fluctuations is of the order of a kilohertz which translated into a time scale of one millisecond.

Arndt and George [10] have derived an equation for a characteristic bubble response time namely

$$T_B = 1.06\left(\frac{\rho R_o^3}{S}\right)^{\frac{1}{2}} \qquad (4)$$

where R_o is the radius of the bubble and S, the surface tension. Therefore for a bubble of 100 μm radius, the response time is of the order of a tenth of a millisecond. This is an order of magnitude shorter than the time scale for the pressure fluctuations. In addition, any change in volume of the bubble caused by the fluctuation of pressures can be easily detected. Hence, a 100 μm bubble was taken to be an ideal size for the present investigation.

With the preferred bubble size determined, steps were taken to create these bubbles. This is discussed in the next section.

4.4 Preliminary Work

It was believed that the desired bubble size could be generated by electrolysis. Trials carried out in a beaker of water using an electrode which was similar in description to that employed in the flow seeding process have shown that the size of the bubbles was

determined by the magnitude of the electrolysis current. For example when the current was 5 mA, bubbles as big as 1 mm in size were observed. Consequently we thought that the required bubble size could be achieved by a suitable combination of the flow velocity and the electrolysis current. This desired condition, of course, was to be obtained through a trial and error process.

However, when the tests were carried out in the nozzle with the electrode inserted in the elbow as before, it was found that the size of the generated bubbles when there was a flow past the electrode was only about 10 μm. Furthermore, neither the magnitude of the flow velocity nor the electrolysis current appeared to have any major effect on the size of these electrolyzed hydrogen bubbles. Different sizes and shapes of the tips of the electrodes were tried too but to no avail. It was suggested that a larger size of bubbles could be obtained if the electrode was placed normal to the direction of flow. However, based on Kuiper's work [75], it was inferred that a relatively broad spectrum of bubble sizes would be produced in such a configuration. This is undesirable since we want only one particular referenced size. It was finally decided to try a new approach.

Air injection was considered next. A length of stainless steel tubing with an internal diameter of 100 μm was used as the injector. It was found that although the bubbles created were approximately of the right size, they were not very spherical. This was because the orifice at the exit of the tubing was not perfectly circular, as a

result of it being partially squashed during the cutting of the tubing to the prescribed length. Since this shortcoming could not be easily avoided, it was decided that a circular glass nozzle be used as the injector instead. This nozzle was made by drawing a small glass tubing down to the necessary dimensions. This method eventually proved to be successful. The bubble generator and the accompanying injection system is described below.

4.5 Description of the Bubble Generator and the Injection System

A diagram of the injection system is illustrated in Figure 4.1. Compressed air supply, regulated to 4 psig, was filtered before being fed to the bubble generator to prevent clogging of the small orifice of the glass nozzle. A "Nupro" meter valve ("S series") located downstream of the air filter allowed the small air flow rate through the system to be adjusted until a tiny stream of bubbles was seen. A shutoff valve was also provided to stop the flow of air into the bubble generator in between runs, without having to tamper with the setting of the meter valve. A by-pass line permitted any back flow of liquid into the bubble generator to be quickly expelled prior to an actual run.

The bubble generator consisted of a glass nozzle drawn from a 1.6 mm O.D. glass tubing. The inner diameter at exit was designed to be approximately 100 μm (0.004"). The glass nozzle was attached to a length of brass tubing and was held together by "intra medic tubing" as shown in Figure 4.2. This whole unit was introduced into

the jet in the same manner as for the electrode used in electrolysis bubble generation. This has been described in Section 2.4 of Chapter 2.

The tip of the bubble generator was positioned on the center line at approximately four diameters upstream of the nozzle exit. A length of 1.6 mm I.D. "intra medic tubing" connected the other end of the bubble generated to the air supply. This completed the air injection system.

4.6 Test Procedures

For a given jet velocity, the air flow rate through the injector was adjusted until a stream of individual bubbles was seen under stroboscopic lighting. A hologram of the flow field was then taken. In this way, a series of holograms were obtained. The procedure was repeated for all three nozzle sizes. It should be mentioned at this point that the bubbles generated were actually less than 100 μm, but we shall still assume that they are of this size in our argument.

In all the above tests, the ambient pressure was kept at approximately 16 psia. The tests were carried out at a jet exit velocity of 13 m/s (≃ 40 ft/s). This velocity was chosen because the resulting pressure fluctuations would be large enough to be easily detected. On the other hand, the fluctuations would not be so intense to cause cavitation in the jet. All the measurements were made using water with a dissolved air content of approximately 11 ppm (saturation is at 15 ppm).

The sizes of the bubbles as a function of the jet position was then measured from the reconstructed images of the holograms and tabulated.

4.7 Data Reduction

Before the instantaneous pressures at various locations in the jet could be computed from the tabulation of bubble sizes, two aspects of the flow had to be considered. The first of these had to do with the "ringing" effect of the bubbles as they were accelerated through the flow nozzle. The other dealt with the rate at which the injected bubbles were dissolving into the water. Both of these will be considered in turn.

Following an argument similar to that presented by Franklin and McMillan [36], it can be assumed that the motion of the bubble after exiting from the flow nozzle is governed by the equation:

$$R(t) = R_e \, e^{-\beta t} \cos \tau$$

where R_e = initial radius of the bubble after exiting from the nozzle,

β = damping constant

ω_o = natural frequency of the bubble and

$\tau = \omega_o t$.

Devin [30] has determined theoretically that the damping constant for a 100 μm bubble is 0.1. He showed that his results compare favorably with the experimental findings of several investigators although his theoretical value was slightly lower. The same value

for β was also reported by Clay and Medwin [115]. As a conservative estimate, the numerical value of β was thus taken to be 0.1 in the present work. Hence the time that elapsed before the injected bubbles acquired steady state could be determined from a plot of $e^{-\beta t} \cos \tau$ vs τ. Such a plot is shown in Figure 4.3. It can be inferred from this plot that the oscillations would have died down for $\tau \geq 40$. This implied that equilibrium was reached after about 30 μs. That is, at a jet exit velocity of 13 m/s, the oscillations would have virtually stopped at distances greater than about 0.5 mm. This has been confirmed from holographic records of the injected bubbles near the nozzle lip which showed no evidence of any oscillations in the string of bubbles. A photographic evidence of this is shown in Figure 4.4.

We shall now direct our attention to the question of the rate at which the injected bubbles were dissolving. We would expect a huge error in the measured volumes of the bubbles if the bubbles were going into solution at a rate comparable to the time they took to traverse the region under observation. By interpolating the results of Epstein and Plesset [34] we have found that it would take about 460 seconds for a 100 μm bubble to completely dissolve in water that is 75% saturated (a dissolved air content of 11 ppm). In addition, it has been estimated that the traverse time of the bubble in the current investigation was of the order of milliseconds. Hence it can be concluded that the dissolved volume of the bubbles would be

negligible and can be ignored.

As was discussed in Section 4.2, the instantaneous pressure at any position is given by

$$P_{\infty_x}(t) = P_{g_o}\left(\frac{R_o}{R_x}\right)^{3\gamma} + P_v - \frac{2S}{R_x} \tag{3}$$

Since dry air was used in the present tests, the vapor pressure inside the bubble was neglected. We believe this is justified because in the extremely short traverse time involved, little or no evaporation was expected to occur. Thus equation (3) reduces to

$$P_{\infty_x}(t) = P_{g_o}\left(\frac{R_o}{R_x}\right)^{3\gamma} - \frac{2S}{R_x} \tag{5}$$

It can be seen from equation (5) above that once P_{g_o} is known then $P_{\infty_x}(t)$ at any position could be calculated using the tabulation of the bubble sizes.

The injected bubbles have been shown to acquire steady state conditions very soon after emerging from the flow nozzle. Therefore, the initial gas pressure P_{g_o} can be obtained from the reduced Rayleigh-Plesset equation, that is

$$P_{g_o} = P_o + \frac{2S}{R_o} \tag{6}$$

where P_o = mean ambient pressure in the jet and

R_o = the radius of the injected bubble at the reference position.

On substitution of P_{g_o} into Equation (3), the equation becomes

$$P_{\infty_x}(t) = \left(P_o + \frac{2S}{R_o}\right)\left(\frac{R_o}{R_x}\right)^{3\gamma} - \frac{2S}{R_x} \qquad (7)$$

Observations of reconstructed images of holograms revealed that in the region beyond the potential core of the jet, some of the bubbles did not retain their spherical forms but were ellipsoidal in shape. An example of this situation is shown in Figure 4.5. The question that came to mind at this point was whether these bubbles still served as good pressure sensors. To answer this question, we have to rely on the findings of Strasberg [108]. He reported that the natural frequency of an ellipsoidal bubble could be very accurately estimated from the response time of a spherical bubble of the same volume. His calculations showed that the natural frequency of bubbles of this shape was only slightly dependent on the ratio of the major to the minor axis of the ellipsoid. In the present measurements, the largest change in volume ever detected was about 3.5 times the original. This translated into an increase of about 50 percent in the initial bubble size or a bubble of 150 μm radius. It can easily be shown from Equation (4) that a bubble of this size still has a relatively short response time. Hence it can be concluded that all the bubbles remained as good indicators of the instantaneous pressure.

In order to determine the volume of these ellipsoidal bubbles, both the semi-minor and semi-major axis need to be measured. However, it is not possible to get the third dimension of the bubble from the reconstructed image. It was thought that this dimension could be determined theoretically. However, it has been pointed out by Barthés-Biesel and Acrivos [17] that "the problem of determining theoretically the shape of a single droplet freely suspended in an unbounded incompressible liquid undergoing a shearing motion is very complex and no general solution is at present available." Most of the work done in this area has been on very simplified linearized models in creeping flows but even then tedious mathematical manipulations were involved. Therefore to circumvent this problem, we assumed that the length of the third axis was given by the geometric mean of the other two measured lengths. In brief, the volume of the ellipsoid was taken to be proportional to the cube of the geometric mean radius, R_m. Hence an equivalent expression of equation (7) for the ellipsoidal bubbles is:

$$P_{\infty_x}(t) = (P_o + \frac{2S}{R_o}) (\frac{R_o}{R_m})^{3\gamma} - \frac{2S}{R_m} \quad . \tag{8}$$

Before we leave this topic, we would like to point out that the error in the measurement of lengths associated with the bubbles was less than 2 μm.

It has always been difficult to decide on the value of the polytropic constant γ to be used. For convenience, many researchers, for

example, Franklin and McMillan [36,37], Plesset and Prosperetti[98], have traditionally taken γ to be 4/3. This value was also used in the present computation. In order to have an idea on the lower bound of the calculated results, the isothermal case was also considered.

Before this chapter comes to a close, it should be mentioned that in all the holograms that were analyzed, no fragmentation of the bubbles was seen. However, a few badly sheared bubbles were observed, as illustrated in Figure 4.6, but they occur very infrequently. The volumes of these sheared bubbles were difficult to determine accurately and were omitted in the computation. It has also been discovered that the bigger bubbles have a greater tendency of being badly sheared than the smaller ones.

Results obtained for the pressure fluctuations are presented and discussed in the next two chapters.

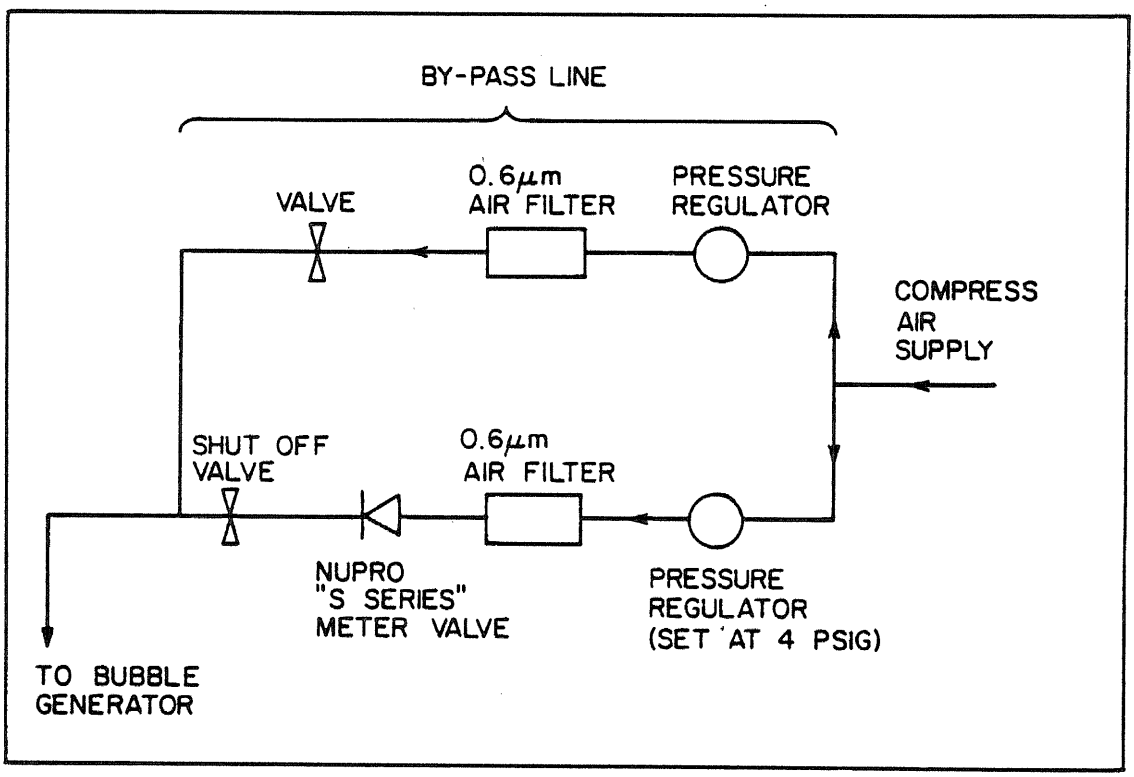

Fig. 4.1. Diagram of the air bubble injection system.

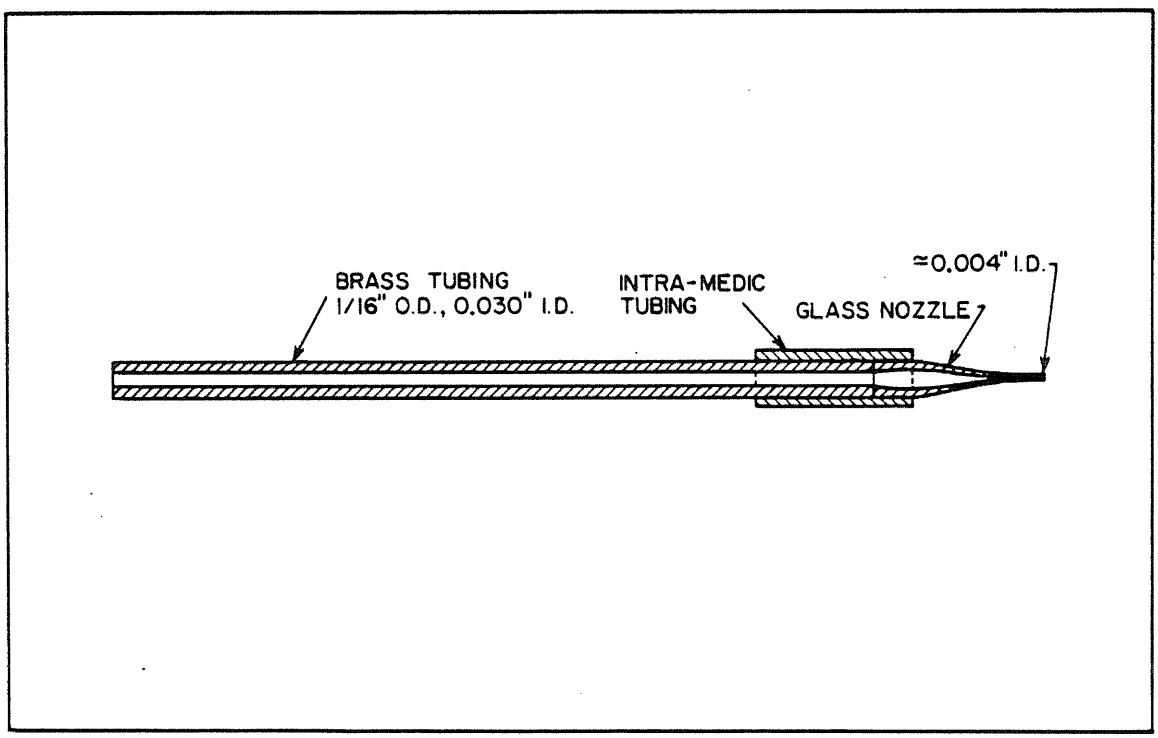

Fig. 4.2. Diagram showing the geometrical details of the bubble generator.

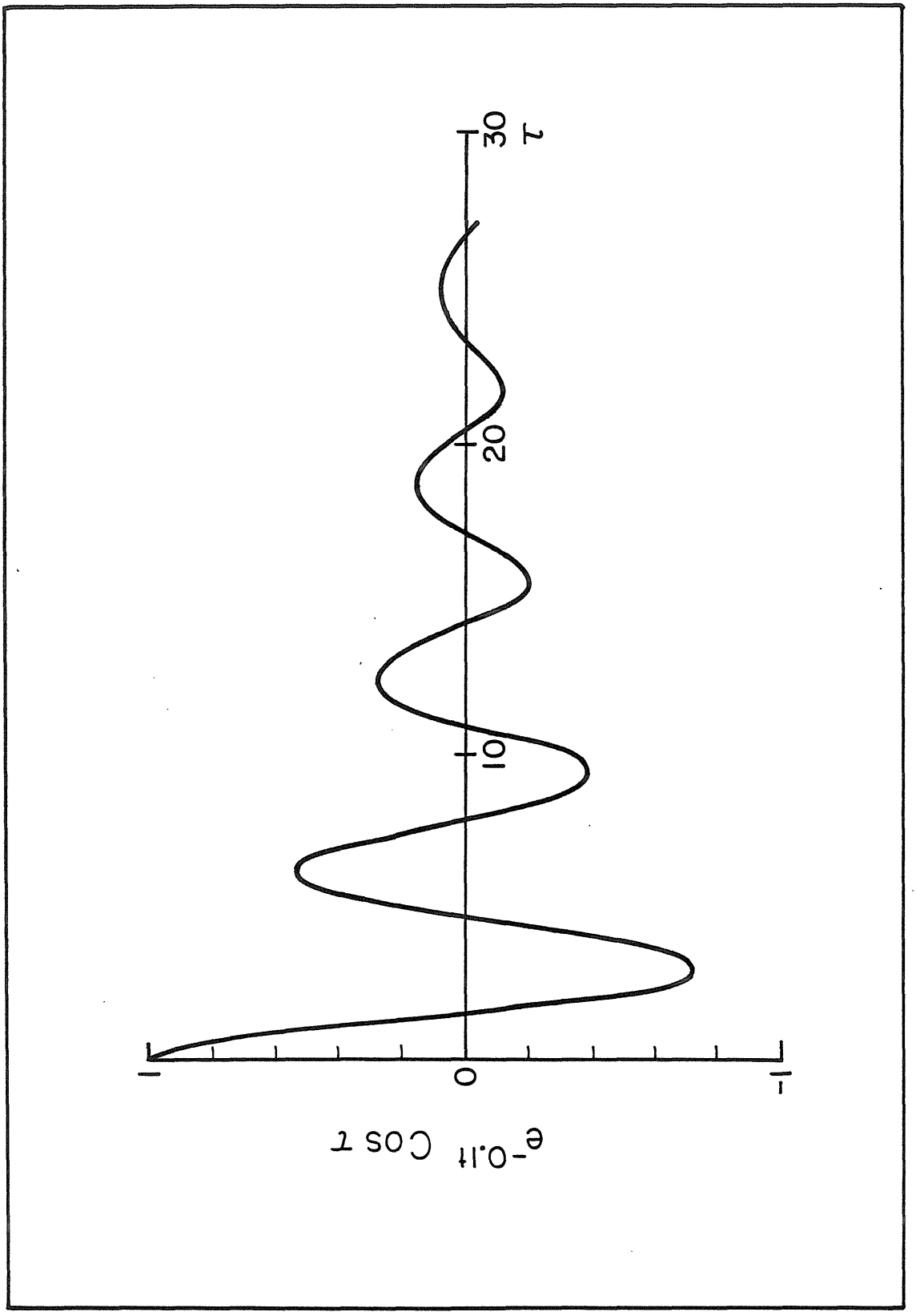

Fig. 4.3. Plot of $e^{-0.1t}$ Cos τ versus τ .($\tau = \omega_0 \tau$).

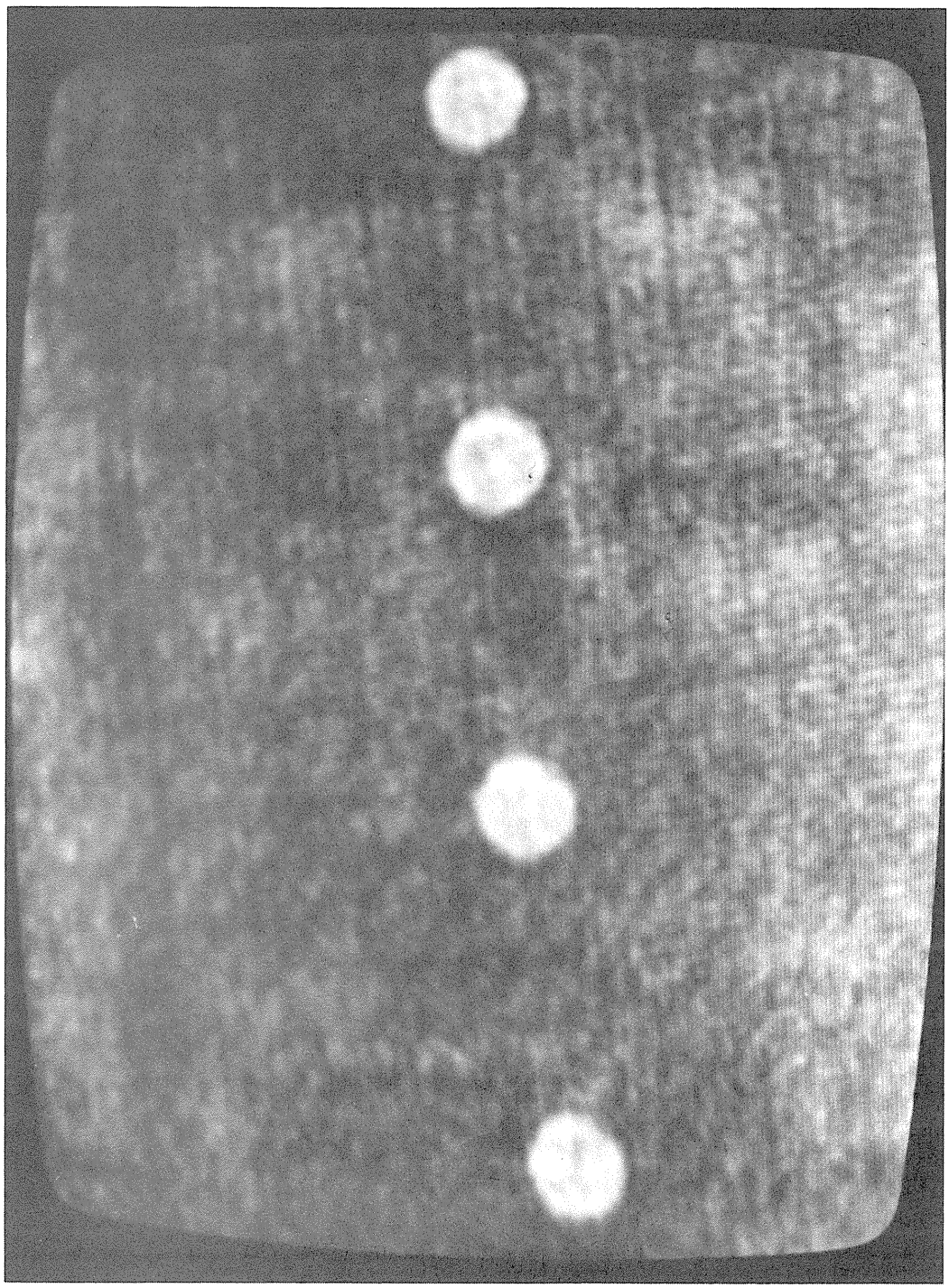

Fig. 4.4. Photograph of the reconstructed image of a string of injected bubbles in the potential core of the jet, near the nozzle exit. The bubbles are 128 μm in diameter.

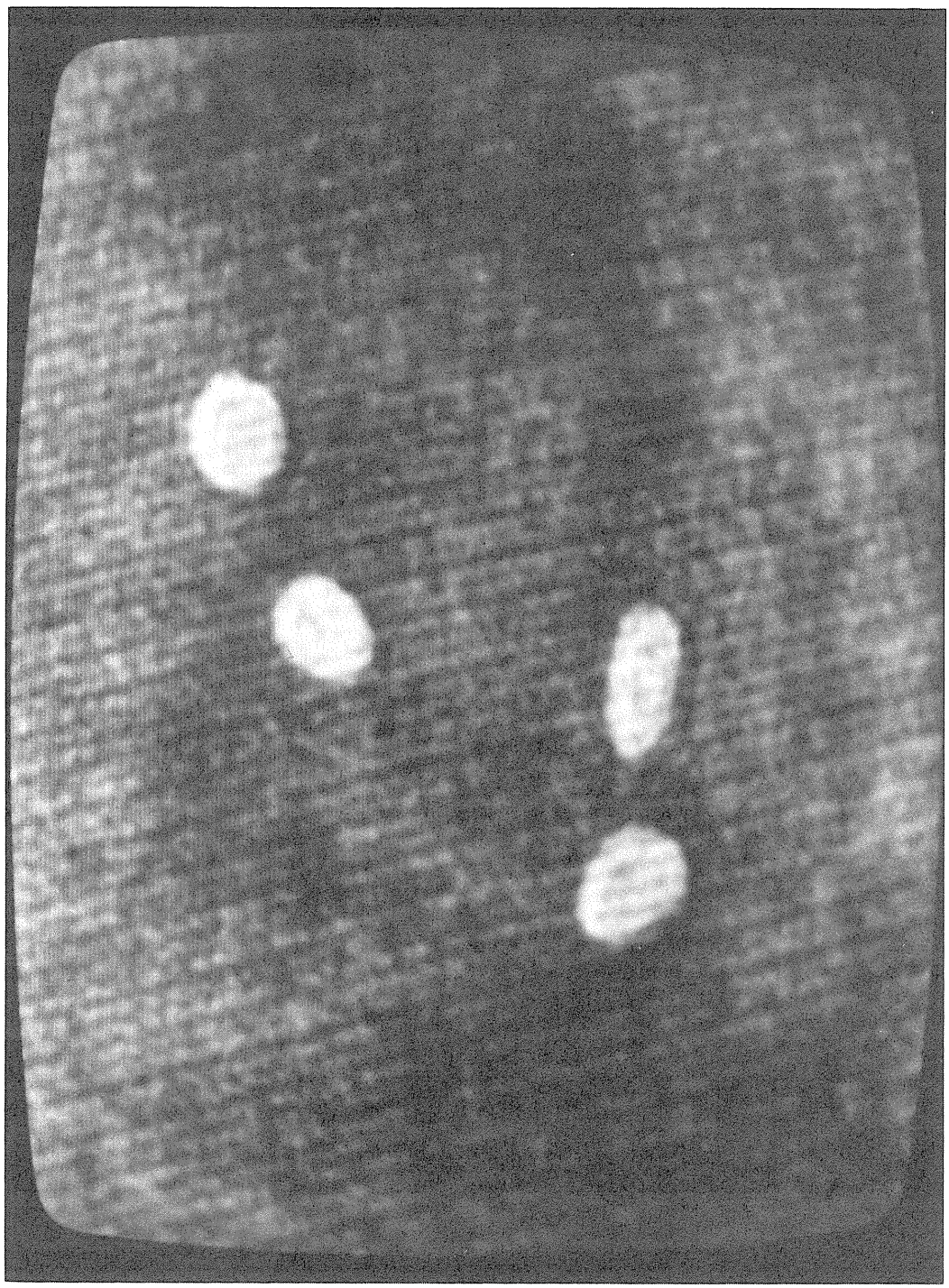

Fig. 4.5. Photograph of the reconstructed image of ellipsoidal bubbles in the transition region of the jet.

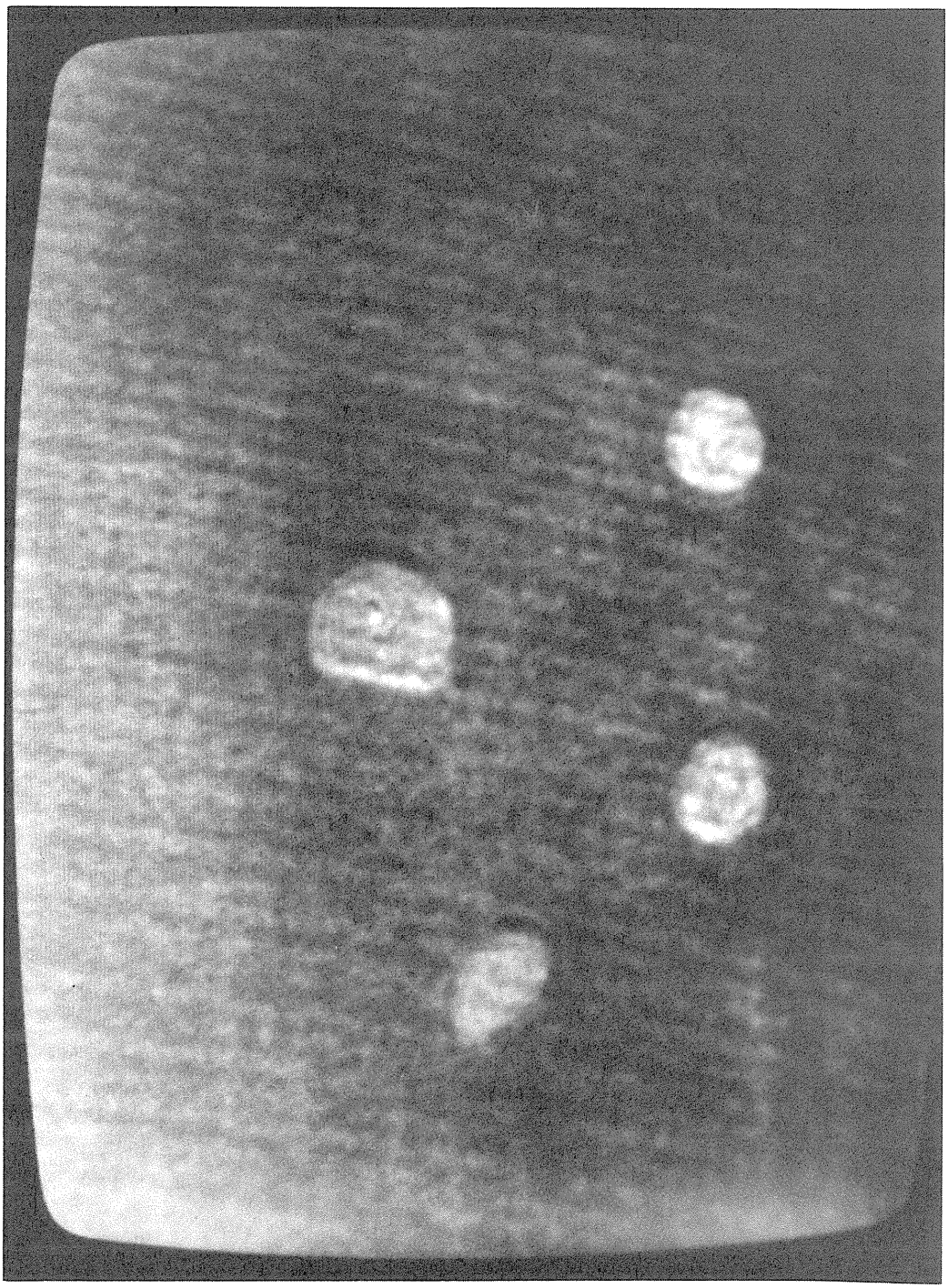

Fig. 4.6. Photograph of the reconstructed image of a badly sheared bubble in the transition region of the jet.

5. PRESENTATION OF RESULTS

5.1 Introduction

The results of the measured cavitation indices and flow visualization are presented in this chapter. Also included are the nuclei population and pressure fluctuation measurements in the three jets investigated. The main features of the various plots and figures are pointed out. However, no attempt is made to explain these features until the next chapter where a complete discussion is presented.

5.2 Measured Scale Effects

The results of the measured scale effects under the various flow conditions were plotted with the incipient cavitation index as the abscissa and the jet exit Reynolds number as the ordinate. These are shown in Figures 5.1 to 5.24.

Figures 5.1 to 5.4 show the effect of jet size at different dissolved air content, α, in the water when the flow is unseeded. An immediate observation is that for a particular nozzle size, the incipient index is independent of the Reynolds number. It can also be seen that while the two smaller jets differ only slightly in their measured indices, at the same degree of air saturation, the largest jet exhibits an incipient index which is significantly higher than the other two. These observations are true over the entire range of dissolved air contents used presently. It should be pointed out that the data points on the graphs are the average measured value and the bars denote the scatter. Furthermore, the reason why relatively few data

points were obtained for the cases when the air content was less than 8 ppm was because the jet could not be made to cavitate at the lower velocities.

The above data are replotted as shown in Figures 5.5 to 5.7 to demonstrate the effect of the dissolved air content on the susceptibility of the jet to cavitation inception, for a constant nozzle size. These plots clearly illustrate the suppression of the inception index with decreasing air content. This effect is much more pronounced for the 3.17 mm and 4.76 mm jets than for the 6.35 mm jet.

The results for the above series of test are summarized in Table 5.1 below to provide a convenient reference.

Size of Jet (/mm)	Measured Value of Incipient Cavitation Index Dissolved Air Content (/ppm)				Comments
	14.1	10.9	7.7	4.2	
3.17	0.16	0.08	0.06	0.03	Independent of Jet Exit Reynolds Number
4.76	0.15	0.11	0.07	0.06	
6.35	0.27	0.24	0.23	0.22	

Table 5.1. Summary of the measured cavitation indices for cavitating jets.

One objective of the present study was to determine the effect of nuclei population on cavitation inception. This was accomplished by seeding the flow with electrolysis bubbles. Electrolysis currents ranging from 0.05 to 5 mA were used to artificially create different nuclei populations. The results of this study are presented in Figures 5.8 to 5.10. For comparison, the inception data obtained at the same

dissolved air content but with no flow seeding are also included in the plots. It can be seen from these plots that the inception number, σ_i, for both the 4.76 mm (Figure 5.9) and 6.35 mm jets (Figure 5.10) exhibit a similar behavior. This is to say that for a constant nozzle size, the σ_i display an increasing dependence on Reynolds number with increasing electrolysis current, I. This dependence of σ_i on Reynolds number does not go on indefinitely with increasing I, but approaches a limit when the current exceeds a certain value. This limit is reached when $I \gtrsim 0.4$ mA for the 4.76 mm jet, and $I \gtrsim 0.6$ mA for the largest jet. As for the smallest jet, it can be seen from Figure 5.8(a) that the behavior described above for the other two jets is duplicated here at an air content of 14 ppm, with the Reynolds number dependence flattening out at $I \gtrsim 0.2$ mA. At the other three air contents (Figures 5.8(b) to 5.8(d)), the inception number of the 3.17 mm jet does not show any significant dependence on Reynolds number, over the range of electrolysis currents used. However, the measured incipient index increases with increasing current. At this juncture, it should be pointed out that the scatter on the measured inception number for all the tests with flow seeding is approximately $\pm$ 0.02. It is also worth noting that the experimental data for a particular nozzle size were measured over as wide a range of jet velocities (or Reynolds number) as possible; the limit was imposed by the operating range of pressures in the LTWT which was approximately 0.2 to 1.0 atmospheres.

The experimental data are replotted as shown in Figures 5.11 to 5.16 to elucidate the effect of the dissolved air content on σ_i at a constant "seeding rate". These plots clearly demonstrate that when the flow is seeded, the influence on σ_i is determined by the electrolysis current I, and does not depend on the dissolved air content. Exceptions to this observation occur for the largest jet at $I \leq 0.6$ mA (Figures 5.15(a) to 5.15(d)) and at I = 5.0 mA (Figure 5.16(d)). In these instances, the amount of dissolved air in the jet water appear to have some effect on the measured inception number, although no regular pattern could be observed.

Figures 5.17 to 5.24 were plotted with the intention of presenting the experimental results in such a way that the influence of jet size on σ_i for jets operating under similar conditions (some dissolved air content and electrolysis current) could be easily grasped. On examination of Figures 5.17 and 5.18, it can be seen that at an air content of approximately 14 ppm and low values of I, the inception data for the smallest jet (3.17 mm) appear to serve as an extension to the results of the 4.76 mm jet in the lower Reynolds number range. However, as I is increased, these data begin to deviate from the data of the 4.76 mm jet and begin to approach those of the largest jet at lower Reynolds number.

At an air content of 10.9 ppm, the inception data for the two smaller jets again show signs of supplementing each other over the range of Re_D investigated, as shown graphically in Figures 5.19 and 5.20. This observation is especially true for $I < 0.6$ mA. At the

same time, the largest jet exhibits a higher value of σ_i than the two smaller jets at corresponding Reynolds number. It is also interesting to note that the slope of the experimental results for the two larger nozzles are nearly the same in the range of electrolysis current between 0.05 mA to 2.0 mA (Figures 5.19(a) to 5.20(c)).

On close inspection of Figures 5.21 to 5.24, it can be inferred that at both air content of 7.7 ppm and 4.2 ppm, there are instances when the data of the two smaller jets supplement each other. At other instances, the jets portray different behavior. In any event, the measured σ_i for the largest nozzle is always higher than for the other two, at the same Reynolds number.

In addition to the observations described above, flow visualization, nuclei population density and pressure fluctuation measurements in the jets were also carried out. These were made in the hope that the information obtained would provide some probable explanations for the observed scale effects. The results for these tests are presented in the next three sections of this chapter.

5.3 Flow Visualization

5.3.1 Observation under Stroboscopic Lighting

As the jet was made to cavitate, the following sequence of events was observed under stroboscopic lighting.

Small irregular shaped cavities were seen in the jet at inception. Schlieren photographs corresponding to this situation are shown in Figures 5.25, 5.26 and 5.27

where the cavities appear in the form of black, unevenly shaped spots. It should be pointed out that the direction of flow of the jet in the above-mentioned figures is from left to right. These cavities were transient in nature and they collapsed and new ones were formed randomly in the jet, within an axial range of 6 to 16 jet diameters downstream of the nozzle lip. In some runs, cavities were seen to appear as near as four jet diameters and as far as twenty diameters downstream but their occurrences were relatively infrequent. Inception was accompanied by "intermittent crepitant sound" caused by the random exploding and collapsing cavities. The "intermittent crepitant sound" continued for a short duration, but with increasing frequency, as the pressure in the tunnel was reduced beyond the inception point, until an almost "continuous popping sound" was heard. Such a situation is recorded in Figure 5.28. The cavities were now more extensive and much larger in size than at inception.

With further reduction in pressure, the almost "continuous popping sound" gave way to a steady roar. The jet was then said to be fully cavitating since no more changes in the appearance of the cavitating jet were observed beyond this point. At this stage, almost the entire region of the jet between one to twenty diameters downstream were covered by cavities. These cavities have been observed to collapse into a cloud of very fine "mist" at distances greater than about twenty diameters. All these features are clearly depicted in Figures 5.29(a) and (b).

The sequence of events described above was true when the jet was nearly saturated with air or when the flow was seeded. However, at an air content of less than 9 ppm and with no flow seeding, the cavitation process was quite different. Inception occurred in a violent burst of cavities, as recorded in Figures 5.30(a), (b) and (c). A comparison with the corresponding cases of the high air content jets revealed that these cavities were more extensive. It was observed that the cavities normally lasted for a very short time, and collapsed soon after formation. If the pressure in the water tunnel was kept at the inception condition for a prolonged period or lowered past this point, a second and subsequent bursts of cavities would result. There appeared to be no regular time interval between bursts, when the jet was effectively a single phase water jet.

On further reduction in pressure, an instant arose when the jet became fully cavitating. This was seen only when $V_j \gtrsim 25$ m/s. (for the two smaller jets). However, there was a difference between this case and the high air content jet described earlier. The low air content jet did not remain fully cavitating over a continuous period but alternated between a fully cavitating and a non-cavitating single phase jet. Again these alternating actions of the jet occurred at irregular intervals.

All the above description was true of the sequence of events that was exhibited by the three jets under investigation, with the exception that in the 6.35 mm jet, cavities at inception were concentrated in the region of two to fourteen diameters from the nozzle exit.

It should also be mentioned that in some test runs at a dissolved air content of 4 ppm, the two smaller jets could not be made to cavitate at all, below a jet exit velocity of 27 m/s, even when the jets were kept at the lowest attainable tunnel pressure over a period of approximately sixty seconds. However, when the flow was seeded by passing a very small amount of current (0.01 mA) through the electrode, cavitation in the jet occurred. The cavitation ceased almost instantly when the current was turned off. This clearly demonstrated the role of nuclei in the inception process.

5.3.2. Flow Observation with Schlieren Photography

Schlieren photography was utilized as a means to give a permanent record of the appearance of the cavitating and non-cavitating jets. The photographic records of the jets at and beyond the inception point confirmed the observations made under stroboscopic lighting.

As mentioned in Section 3.4, schlieren photographs were taken with the knife edge at two different positions. This was done to ensure that all the features in the jet were revealed. Figures 5.31(a) - (d) are a series of schlieren photographs of the 6.35 mm (0.25 inch) jet at different exit velocities, taken with the knife edge parallel to the direction of flow. An obvious observation is that the jets are laminar at exit and the length of the laminar region retreats towards the nozzle lip as the velocity in the jet increases. Another striking feature of the jets is the appearance of cellular shaped structures at the end of the laminar region just upstream of the turbulent regime. On closer inspection, it can be seen that the size

of these structures decreases with increasing velocity.

Figures 5.32(a) - (d) are of the same jet but recorded with the cut-off edge perpendicular to the flow direction. All the above described features are again seen here except that in the turbulent region of the jet, the scale of the grainy structures is a little finer. In addition, the jet taken with this knife edge position has a "flat" appearance, whereas in the earlier situation it appears more "tubular" in form.

Corresponding sets of figures are also presented for the 4.76 mm (0.188 inch) and 3.17 mm (0.125 inch) jets. These are found in Figures 5.33(a) - (d) and 5.34(a) - (d) for the 4.76 mm jet and Figures 5.35(a) - (d) and 5.36(a) - (d) for the smallest jet. A careful examination of these figures shows that the features exhibited by the 6.35 mm jet are also displayed by these two smaller jets, but are correspondingly smaller in scale.

Two types of measurements were obtained from the schlieren photographs. The first of these measurements was the determination of the non-dimensional length of the laminar portion, L_j/D, of the jet as a function of the jet exit Reynolds number. These results are summarized graphically in Figures 5.37(a), (b) and (c). It can be inferred from these plots that for the two larger jets, L_j/D decays exponentially with increasing Reynolds number while the smallest jet shows a linear dependence, at least over the range of Re_d currently investigated. Secondly, the spread rate of the jets was determined. This was done, for each jet, by measuring the width of the jet at various down-

stream stations in the jet, from the photographic records. The results were plotted in a non-dimensional form as shown in Figures 5.38(a) - (c). It is evident from these graphs that the spread of the two smaller jets is independent of the jet velocity. However, there are indications that the spread of the largest jet, especially near the nozzle exit, is affected by the exit velocity. It should be mentioned that each data point on the plots corresponded to the average of three measurements made from identical runs.

5.3.3 Flow Visualization with Holography

Holographic studies of the non-cavitating jet at various cavitation number revealed that, irrespective of the dissolved air content in the water, no nuclei greater than 40 μm in diameter were found in any region of the three jets investigated. This observation was even true at flow conditions approaching the cavitation inception point. It should be noted that the size of the holograms permitted only 5 cm of the downstream distance of the jet to be scrutinized.

When the flow was seeded, a large amount of bubbles of approximately 10 μm in diameter were detected in the jet. Apparently, the size of these bubbles was not significantly affected by either the jet velocity or the magnitude of the electrolysis current.

A careful examination of holograms of jets at inception confirmed that the cavities were contained in the same distance range mentioned in earlier sections of this chapter. However, it was also found that the cavities could occur at any region across the width

of the jet favoring no particular radial position. The above findings were obtained through the analysis of 18 holograms.

5.4. Nuclei Population Density Measurements by Holography

The nuclei populations in the jets were measured from holograms of the non-cavitating jet at different values of σ and at four different dissolved air content. In a typical hologram where the nuclei population was to be determined, the jet was divided into four different regions labelled 1, 2, 3 and 4 as shown schematically in Figure 5.39. The nuclei count in each of these regions was reduced to a number density distribution function $N(\overline{R})$ defined as follows:

$$N(\overline{R}) = \frac{\text{number of nuclei per unit volume with radii between } R_1 \text{ and } R_2}{(R_2 - R_1)}$$

where the mean bubble radius, $\overline{R}$, is given by $(R_1 + R_2)/2$. Note that R_1 and R_2 correspond to the lower and upper limits of a certain size range. The nuclei were sorted into the following categories: $5\ \mu m < R \leq 10\ \mu m$, $10\ \mu m < R \leq 20\ \mu m$ and $R > 20\ \mu m$. Although nuclei less than 5 μm in radius were observed, they were not recorded in the present work, because they could not be counted with the same degree of certainty as the bigger size nuclei due to optical noise. In all the nuclei measurements made presently, the control volume that was used was defined as

$$\text{Control Volume} = D \times D \times D$$

where D is the jet size.

Figures 5.40(a) - (d), 5.41(a) - (d) and 5.42(a) - (c) are plots of the number density distribution of the 3.17 mm, 4.76 mm and the 6.35 mm jet, respectively. The plots in each set represent the density functions in the designated regions of the jet and are labelled accordingly on the graphs. It can be seen from these plots that there is a definite dependence of the number density function on the dissolved air content, α. Also, it can be inferred from the figures that the data points corresponding to a specific air content do not show a regular pattern with which the measured $N(\overline{R})$ varies with the cavitation number. In addition, a comparison of the data from plots of similarly labelled regions in the three jets indicated that at a constant air content, the measured values of $N(\overline{R})$ for a particular size category fall approximately in the same range of values. Consequently, the value of $N(\overline{R})$ for a specific air content was obtained by averaging the results of all the jets at that air content. In so doing, it was assumed that the density function did not depend on the cavitation number. This appears to be a fair assumption since as pointed out earlier, the dependence of $N(\overline{R})$ on σ does not follow a uniform pattern. It should be mentioned that documentation of the nuclei population in Region 4 of the largest jet was not possible because that region was not contained in the holographic record, due to the small size of the hologram.

Table 5.2 summarizes the results of the present nuclei population density distribution measurements. The entries in this tabulation will be analyzed and discussed in the next chapter. For now, it suf-

	Region 1		Region 2		Region 3		Region 4	
α (ppm)	$N(\bar{R})$	(m^{-4})	$N(\bar{R})$	(m^{-4})	$N(\bar{R})$	(m^{-4})	$N(\bar{R})$	(m^{-4})
	A	B	A	B	A	B	A	B
14.3	3.04×10^{13}	2.48×10^{12}	4.39×10^{13}	2.85×10^{12}	3.41×10^{13}	2.72×10^{12}	4.26×10^{13}	3.02×10^{12}
11.0	1.48×10^{13}	1.46×10^{12}	1.99×10^{13}	1.62×10^{12}	1.35×10^{13}	1.64×10^{12}	1.62×10^{13}	1.62×10^{12}
7.7	4.81×10^{12}	8.21×10^{11}	5.58×10^{12}	9.53×10^{11}	4.30×10^{12}	7.89×10^{11}	4.73×10^{12}	7.03×10^{11}
4.2	1.06×10^{12}	2.14×10^{11}	1.12×10^{12}	2.95×10^{11}	1.07×10^{12}	2.00×10^{11}	1.12×10^{12}	3.18×10^{11}

$A \equiv 5\ \mu m < R \leq 10\ \mu m$ $\qquad$ $B \equiv 10\ \mu m < R \leq 20\ \mu m$

Table 5.2. Summary of the number density function of nuclei measurements in jets.

fices to say that no nucleus with a radius greater than 20 μm was sighted in any of the jets.

When electrolysis bubbles were introduced into the flow, it was found that the nuclei were so numerous that the number could not be counted with any degree of certainty. Hence the effort was abandoned. However, an attempt was made to estimate the number of bubbles that were generated by the electrolysis current. This estimate was based on the work of Kuiper [75] and is considered in Chapter 6.

5.5 Measurements of Pressure Fluctuation

The motivation behind the desire to measure the pressure fluctuations in a jet and the techniques employed to achieve this objective have already been discussed in Chapter 4. The results are presented below.

Figures 5.43 and 5.44 are examples of the instantaneous pressure fluctuations in the 3.17 mm and 4.76 mm jets, respectively. The data for the 6.35 mm jet are not presented because, as pointed out earlier, the size of the hologram prevented any detail mapping of the pressure field. In these graphs, the pressure fluctuation P' is expressed as a fraction of the dynamic head at the exit of the jet and is plotted against the non-dimensional axial position. The lines on the graphs join data points at constant radial position in the jet. The plots were made on a predetermined radial grid spacing as shown on the graph and all the data points that fell within a value of ±0.1 of a particular non-dimensional radial position were

assumed to be at that position. These graphs clearly show that a whole spectrum of pressure fluctuations ranging from 0 percent to 160 percent of the dynamic head is present at any one instant in the jet.

Figure 5.45 is a probability histogram which shows the distribution of the intensities of pressure fluctuations in the jet. This curve was obtained by incorporating all the data from 17 holograms and was plotted in a non-dimensional form as shown, N_b being the number of data points in a certain category and N_b^* ($\simeq$130) corresponds to the maximum number recorded on the probability histogram. It should be pointed out that only the data on pressure fluctuations outside of the potential core region of the jet were used in the present plot. This was because within the potential core little or no pressure fluctuations were registered. Hence, if these data points were included in the histogram, they would have caused an unfair bias towards the lowest pressure fluctuation intensity category. It can be inferred from this graph that the pressure fluctuation has an almost Gaussian distribution, but is skewed somewhat. Notice also that the fluctuations peak at a higher positive value than a negative one. Figure 5.46 is the distribution curve when the data are replotted as a function of the modulus of the dimensionless pressure fluctuation intensity. Both Figures 5.45 and 5.46 are for the case when the pressure calculations were made with a polytropic index of 4/3. For comparison, corresponding plots for the isothermal case are found in Figures 5.47 and 5.48.

The results of flow visualization, pressure measurements and nuclei population measurements presented here will now be correlated to the observed scale effects. This is carried out in the next chapter.

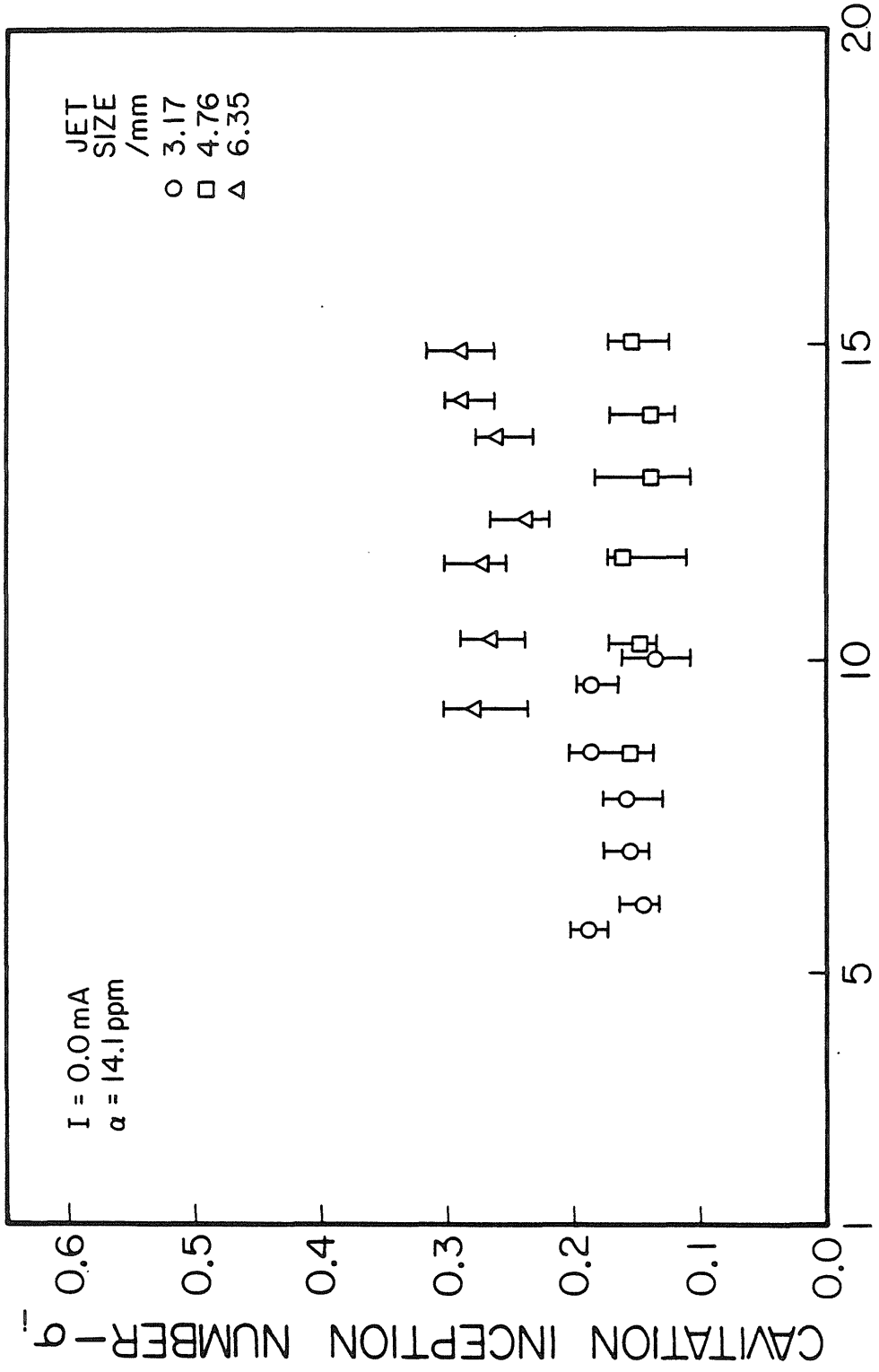

Fig. 5.1. Variation of the incipient cavitation index with jet exit Reynolds number for the 3.17mm, 4.76mm and 6.35mm jet at a dissolved air content of 14.1ppm.

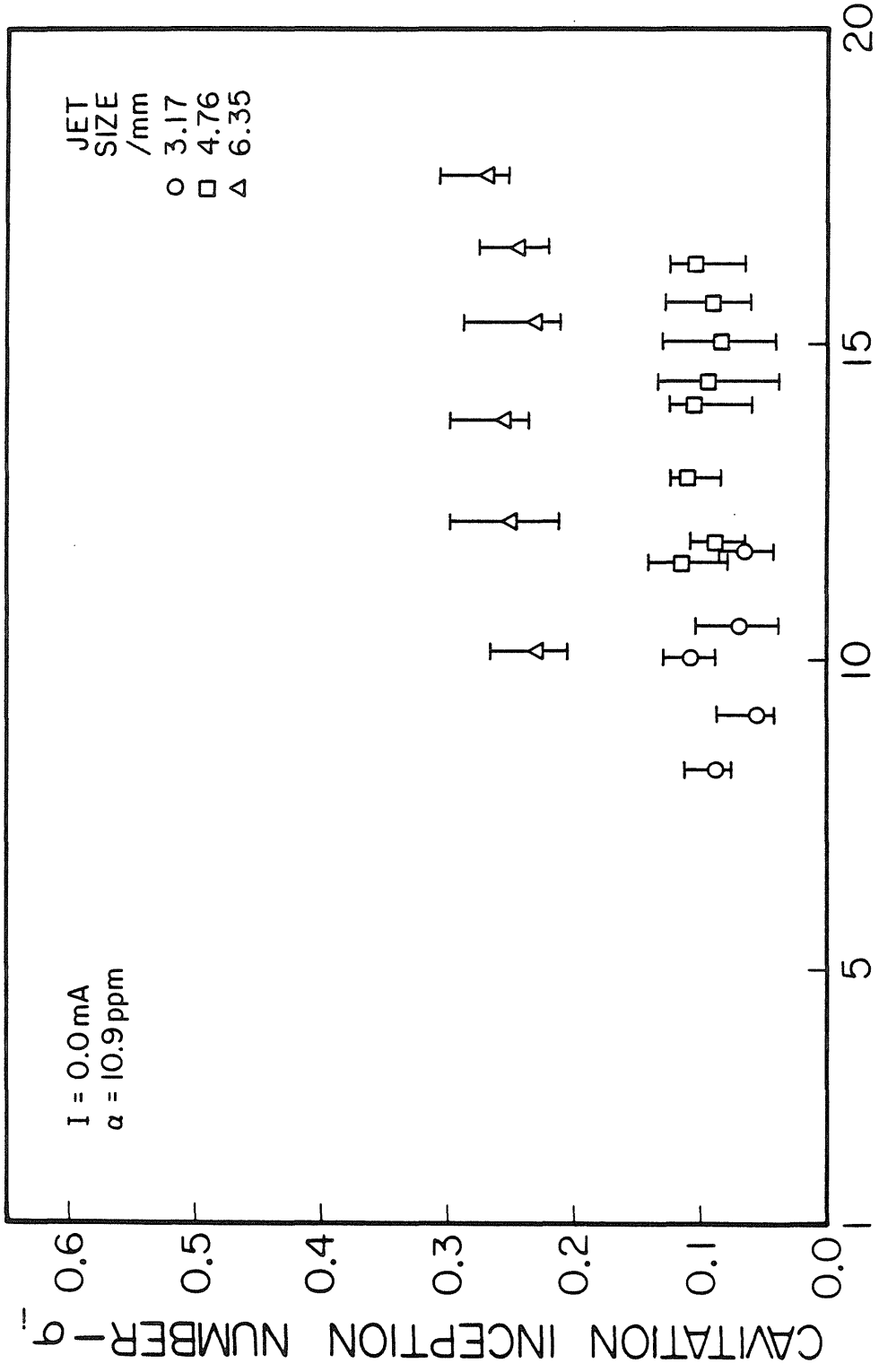

Fig. 5.2. Variation of the incipient cavitation index with jet exit Reynolds number for the 3.17mm, 4.76mm and 6.35mm jet at a dissolved air content of 10.9ppm.

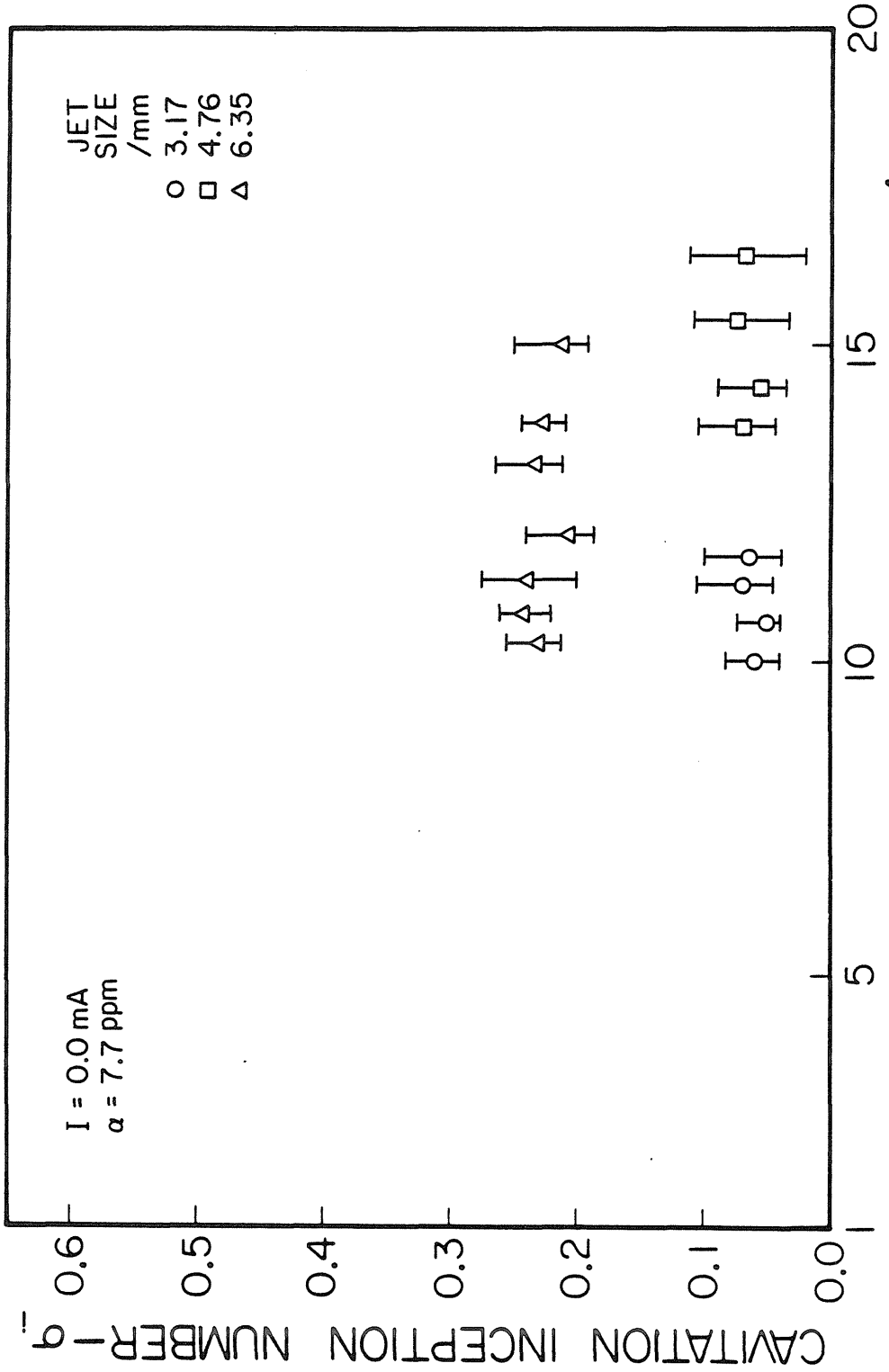

Fig. 5.3. Variation of the incipient cavitation index with jet exit Reynolds number for the 3.17mm, 4.76mm and 6.35mm jet at a dissolved air content of 7.7ppm.

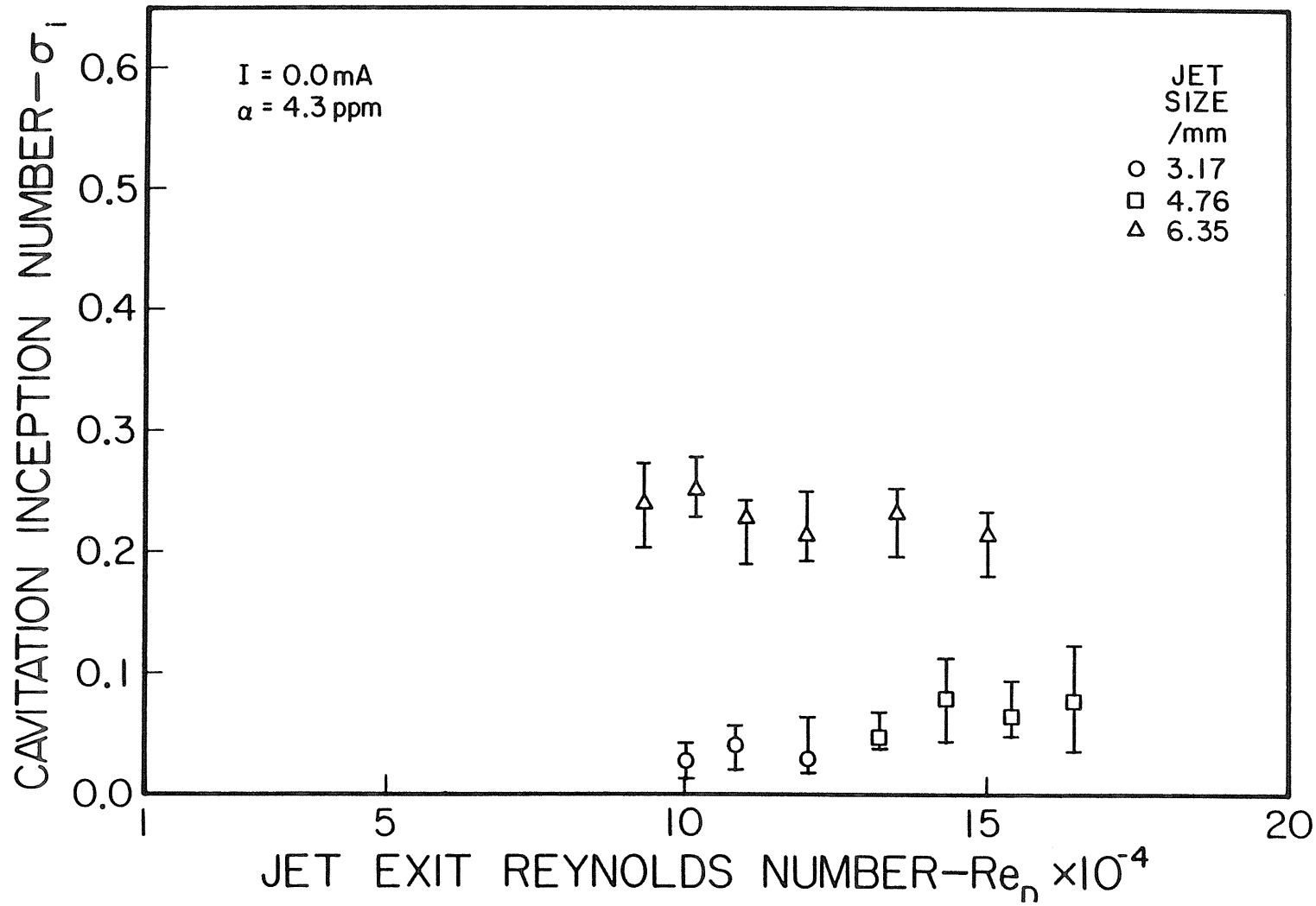

Fig. 5.4. Variation of the incipient cavitation index with jet exit Reynolds number for the 3.17mm, 4.76mm and 6.35mm jet at a dissolved air content of 4.3ppm.

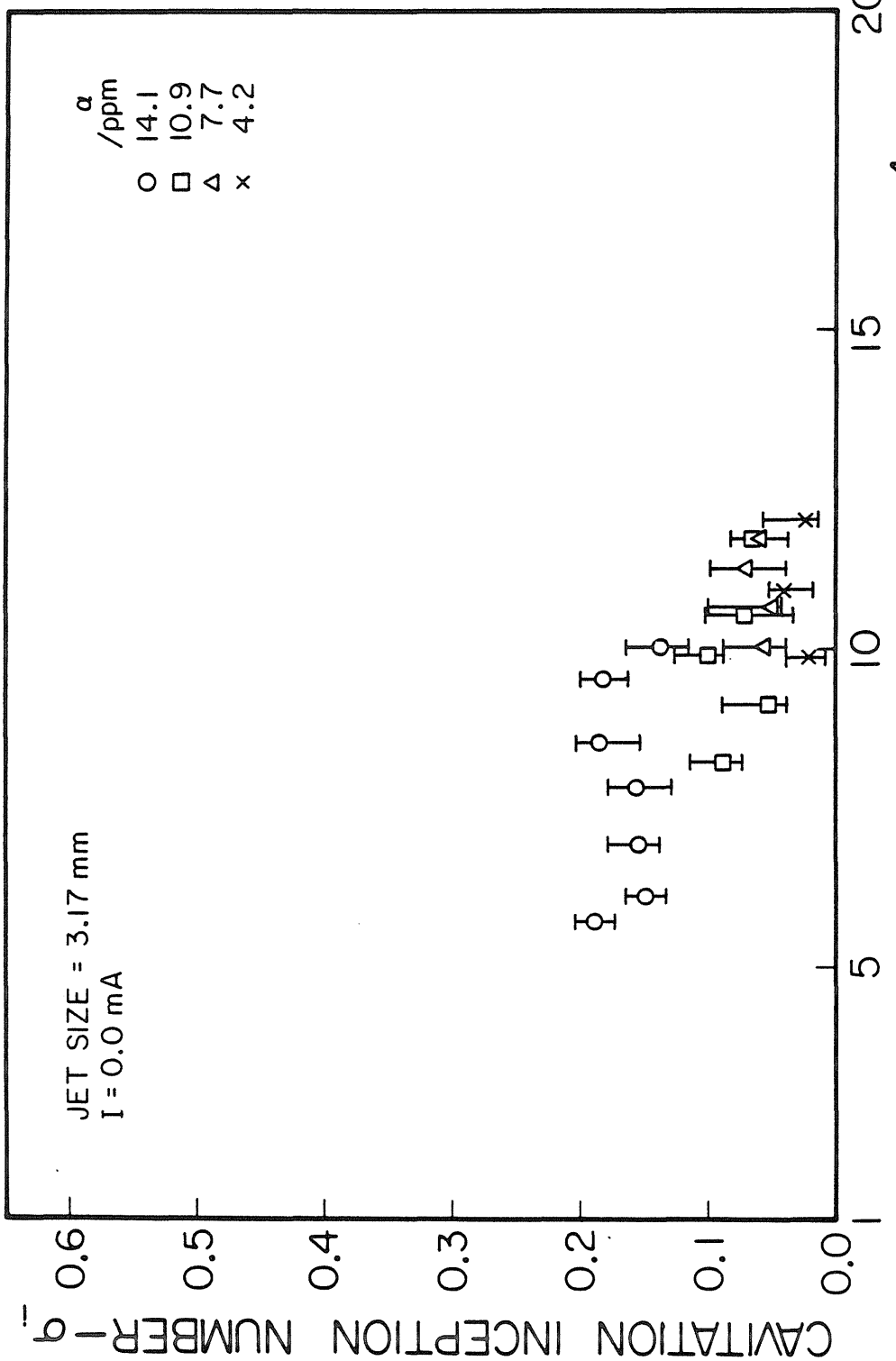

Fig. 5.5. Summary of the variation of the incipient cavitation index with Reynolds number at different dissolved air contents for the 3.17mm jet.

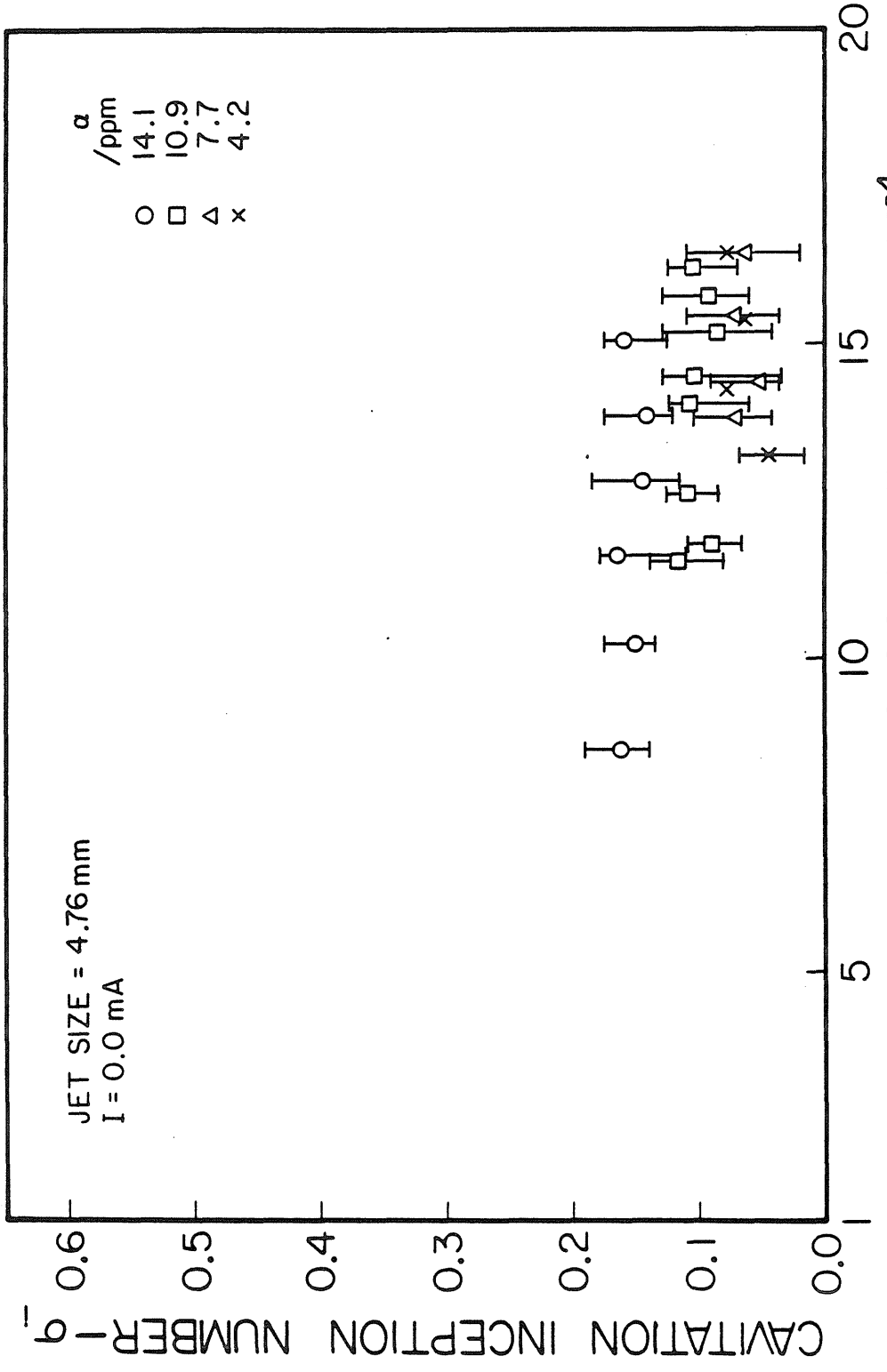

Fig. 5.6. Summary of the variation of the incipient cavitation index with Reynolds number at different dissolved air contents for the 4.76mm jet.

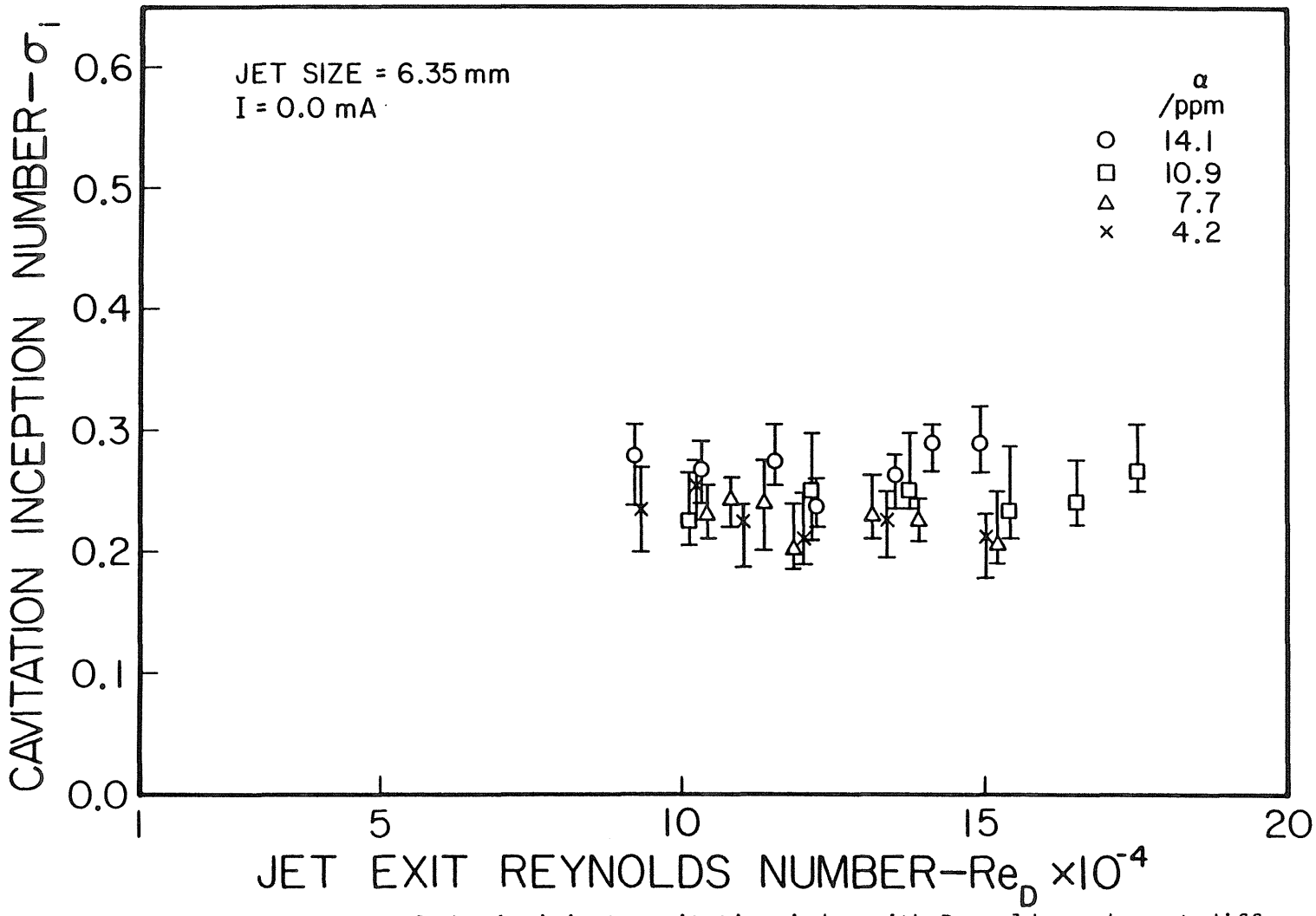

Fit. 5.7. Summary of the variation of the incipient cavitation index with Reynolds number at different dissolved air contents for the 6.35mm jet.

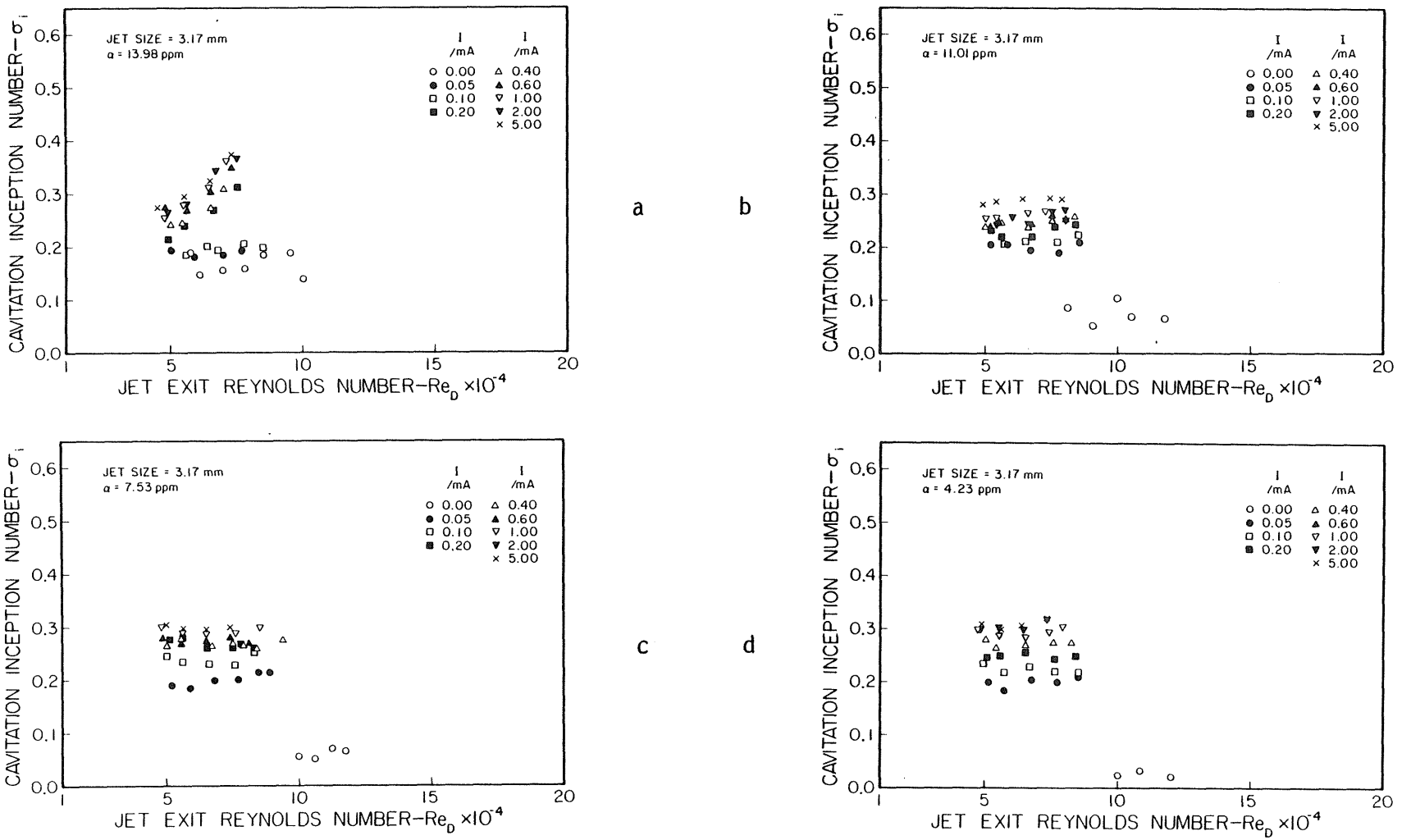

Fig. 5.8. Variation of the incipient cavitation index with Reynolds number at different electrolysis currents for the 3.17mm jet: (a) α = 13.98ppm, (b) α = 11.01ppm, (c) α = 7.53ppm, and (d) α = 4.23ppm.

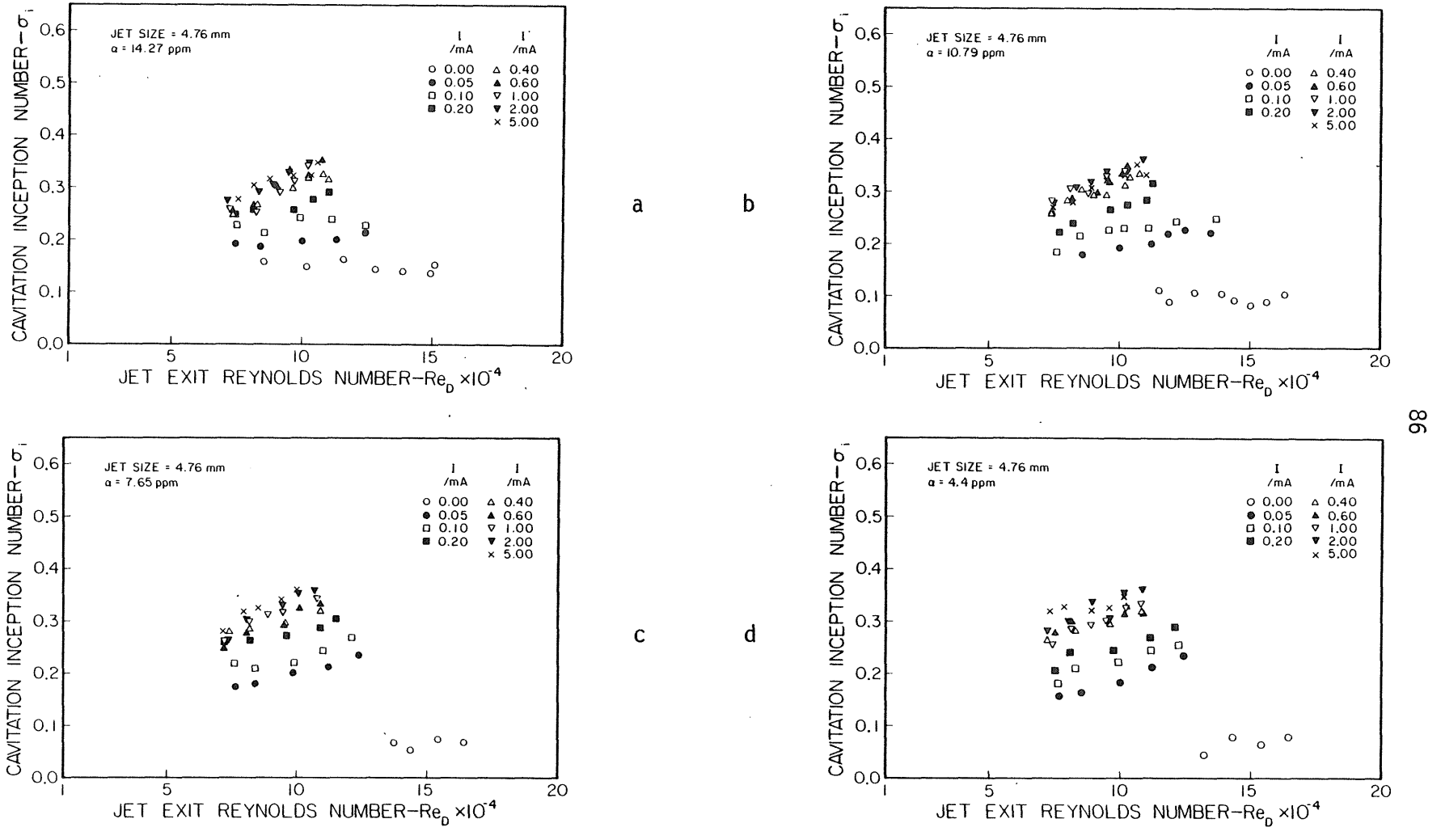

Fig. 5.9. Variation of the incipient cavitation index with Reynolds number at different electrolysis currents for the 4.6mm jet: (a) α = 14.27ppm, (b) α = 10.79ppm, (c) α = 7.65ppm, and (d) α = 4.40ppm.

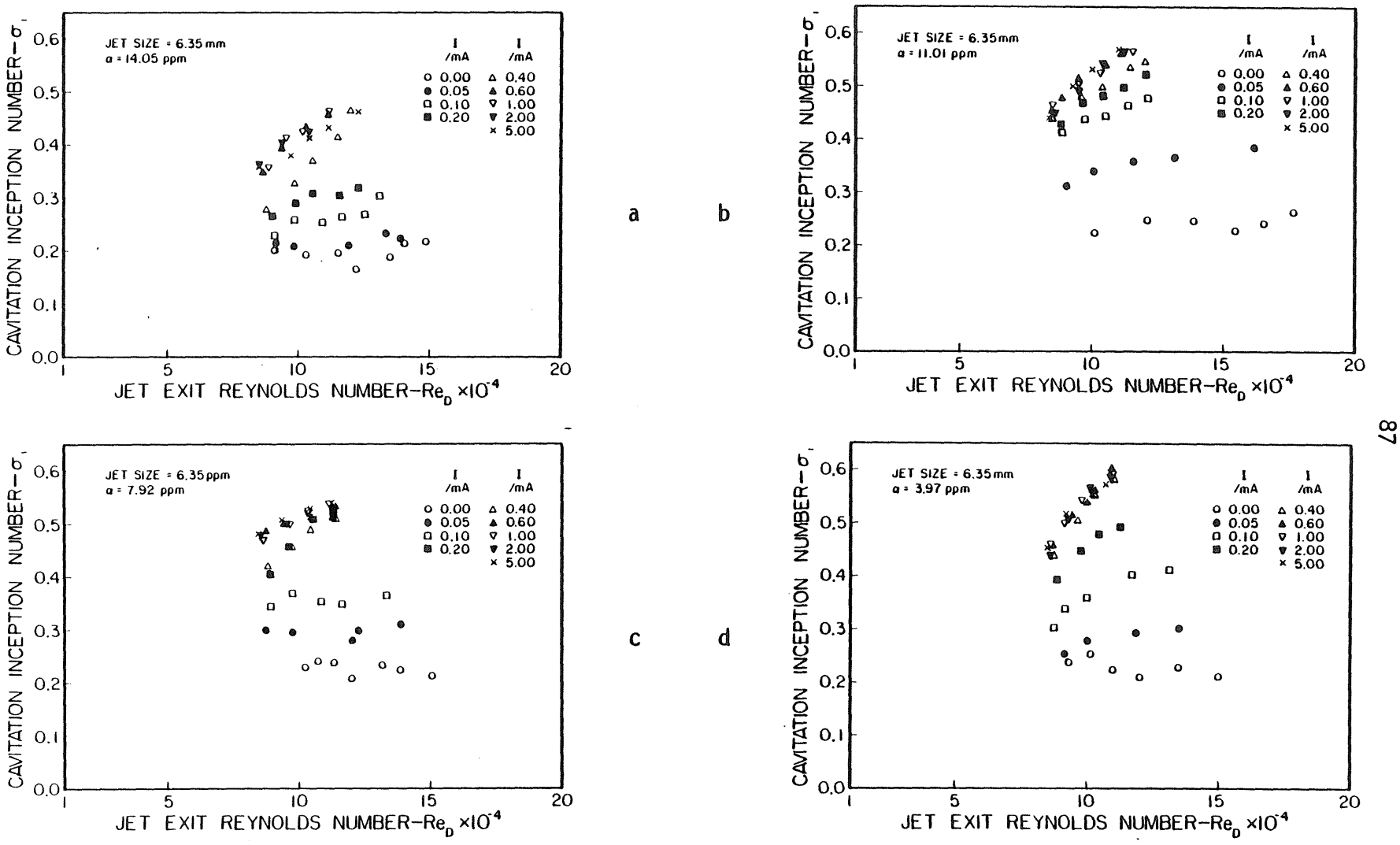

Fig. 5.10. Variation of the incipient cavitation index with Reynolds number at different electrolsis currents for the 6.35mm jet: (a) $\alpha = 14.05$ppm, (b) $\alpha = 11.01$ppm, (c) $\alpha = 7.92$ppm, and (d) $\alpha = 3.97$ppm.

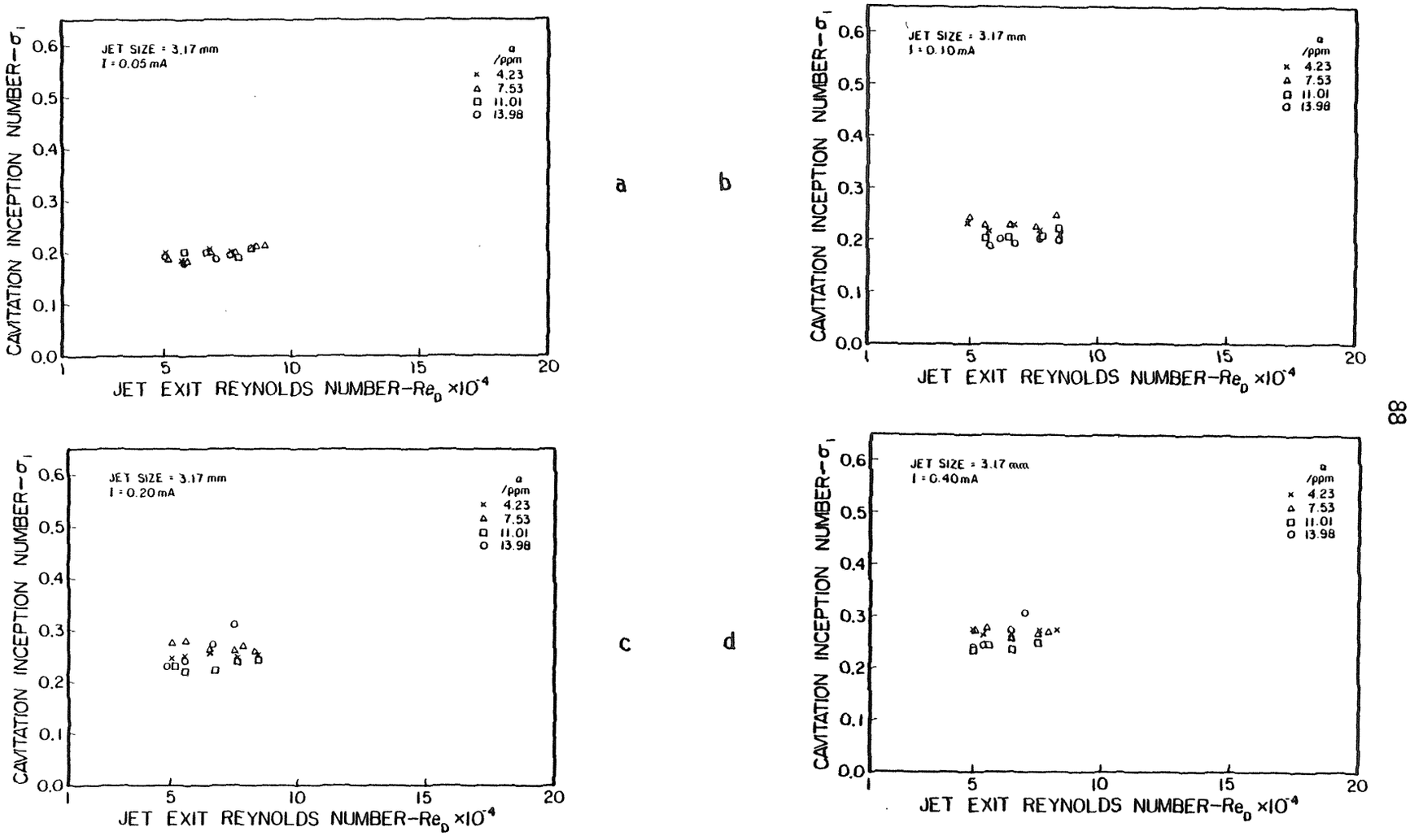

Fig. 5.11. A plot of σ_i versus Re_D illustrating the effect of dissolved air content on the incipient cavitation index when the 3.17mm jet was seeded: (a) I = 0.05mA, (b) I = 0.10mA, (c) I = 0.20mA, and (d) I = 0.40mA.

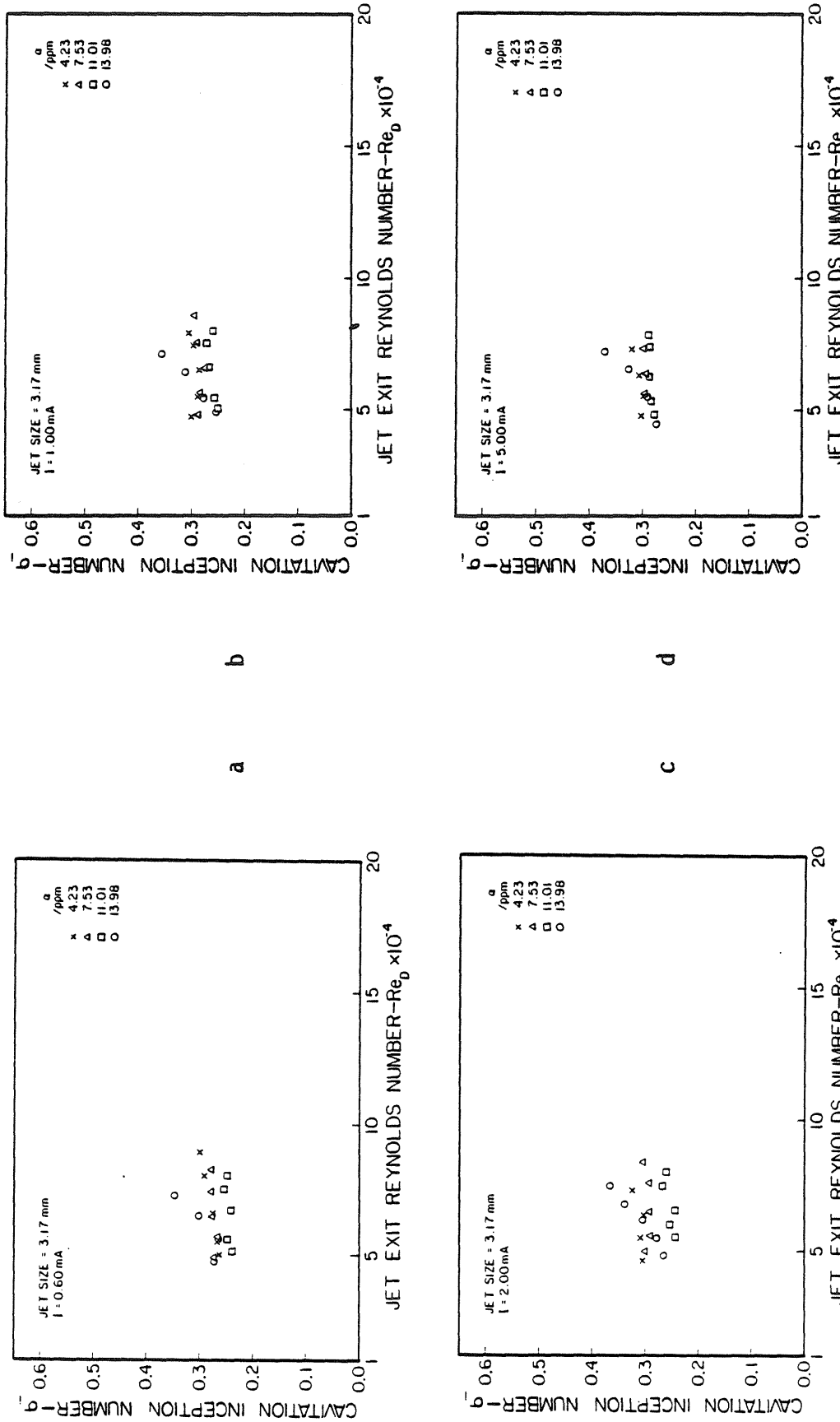

Fig. 5.12. A plot of σ_i versus Re_D illustrating the effect of dissolved air content on the incipient cavitation index when the 3.17mm jet was seeded: (a) I = 0.6mA, (b) I = 1.0mA, (c) I = 2.0mA, and (d) I = 5.0mA

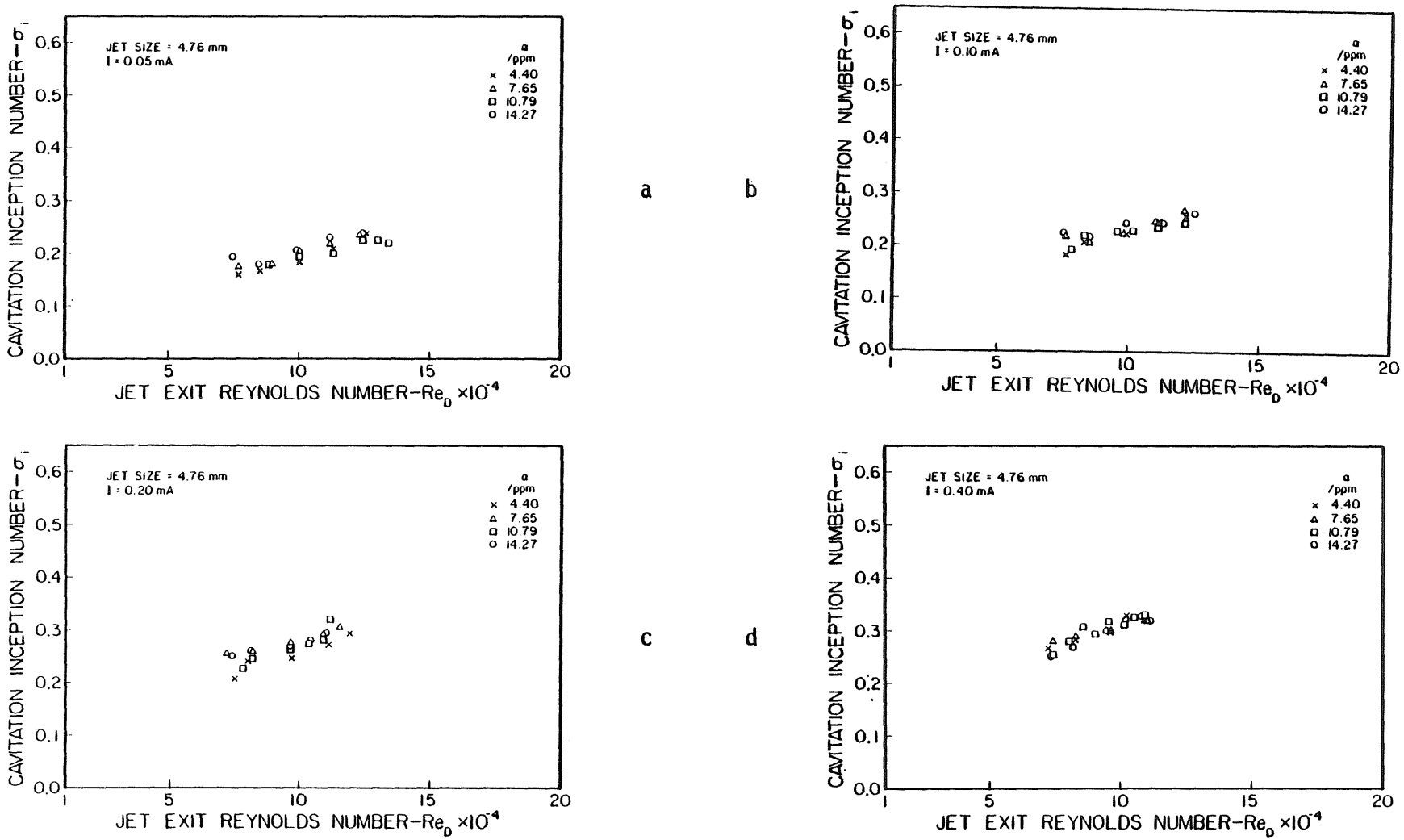

Fig. 5.13. A plot of σ_i versus Re_D illustrating the effect of dissolved air content on the incipient cavitation index when the 4.76mm jet was seeded: (a) I = 0.05mA, (b) I = 0.10mA, (c) I = 0.20mA, and (d) I = 0.40mA.

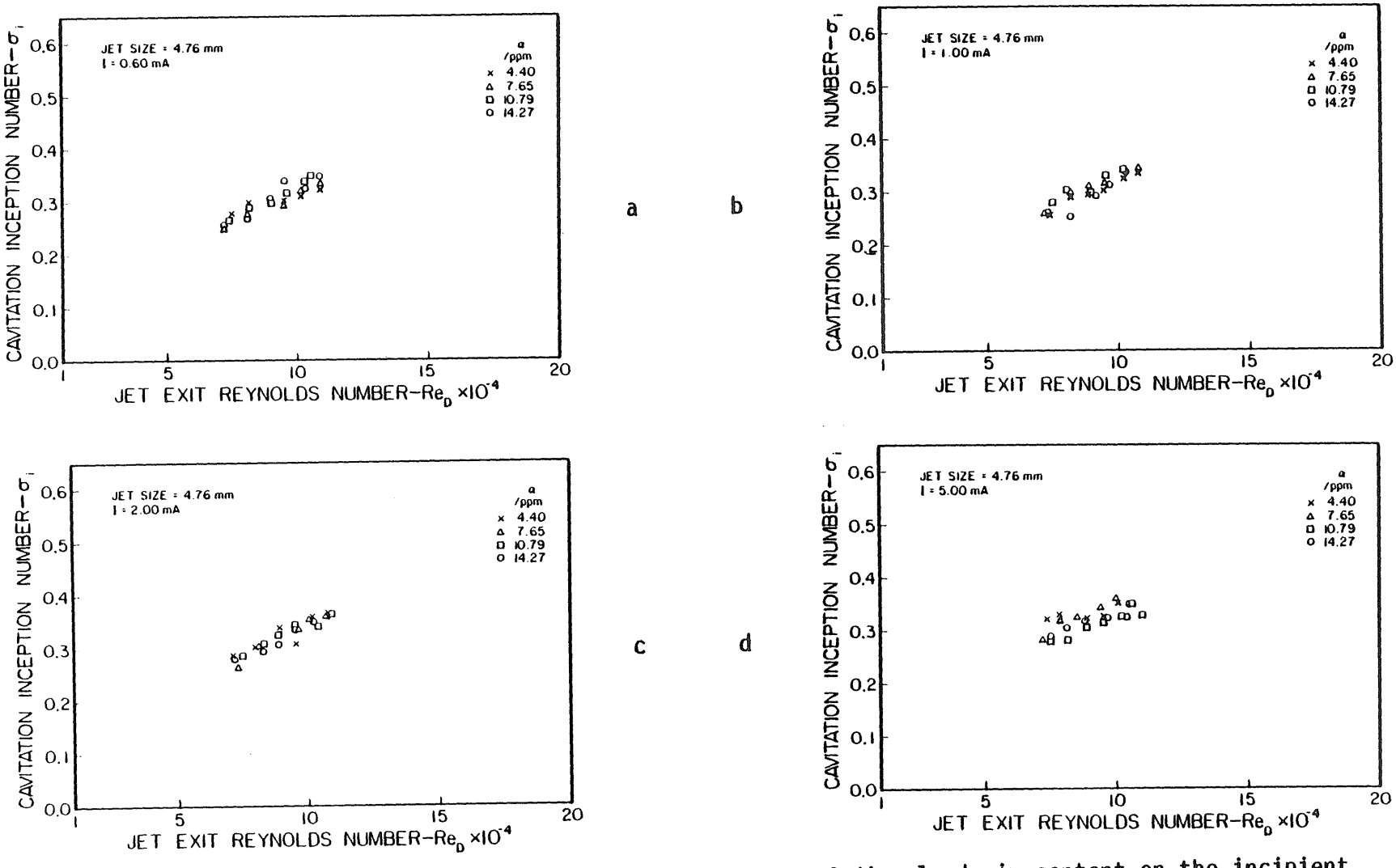

Fig. 5.14. A plot of σ_i versus Re_D illustrating the effect of dissolved air content on the incipient cavitation index when the 4.76mm jet was seeded: (a) I = 0.6mA, (b) I = 1.0mA, (c) I = 2.0mA, and (d) I = 5.0mA.

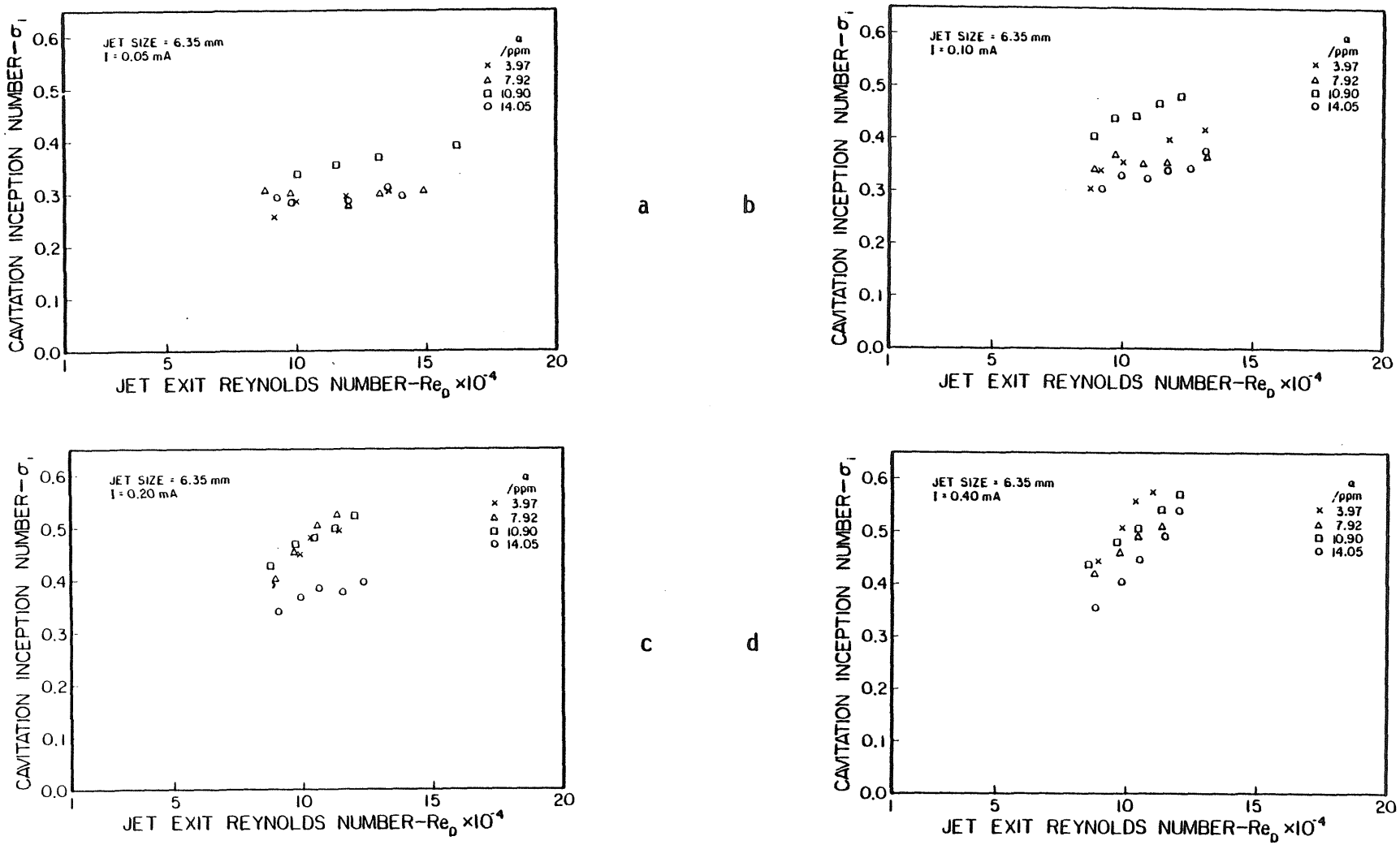

Fig. 5.15. A plot of σ_i versus Re_D illustrating the effect of dissolved air content on the incipient cavitation index when the 6.35mm jet was seeded: (a) I = 0.05mA, (b) I = 0.10mA, (c) = 0.20mA, and (d) I = 0.40mA.

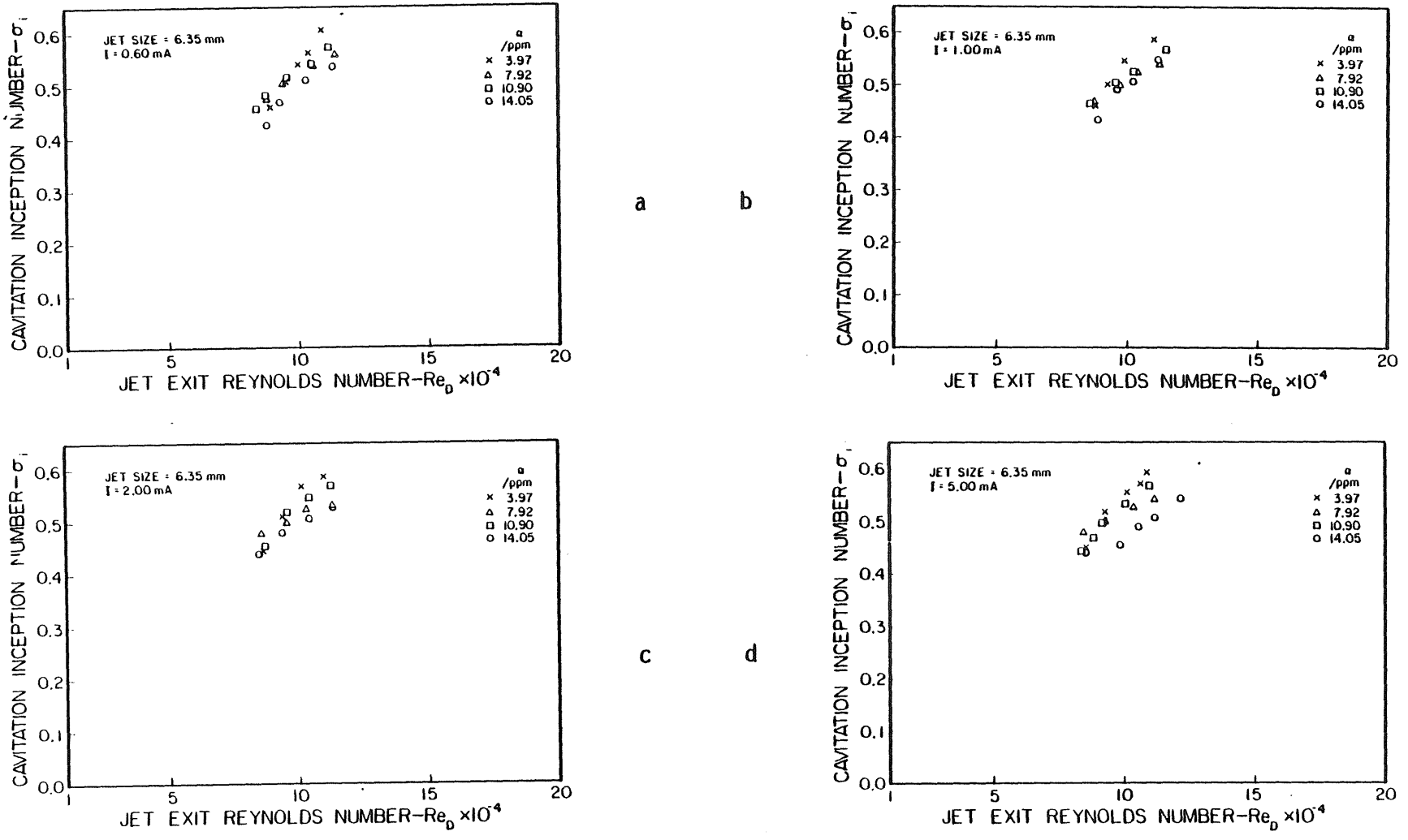

Fig. 5.16. A plot of σ_i versus Re_D illustrating the effect of dissolved air content on the incipient cavitation index when the 6.35mm jet was seeded: (a) I = 0.6mA, (b) I = 1.0mA, (c) I = 2.0mA, and (d) I = 5.0mA.

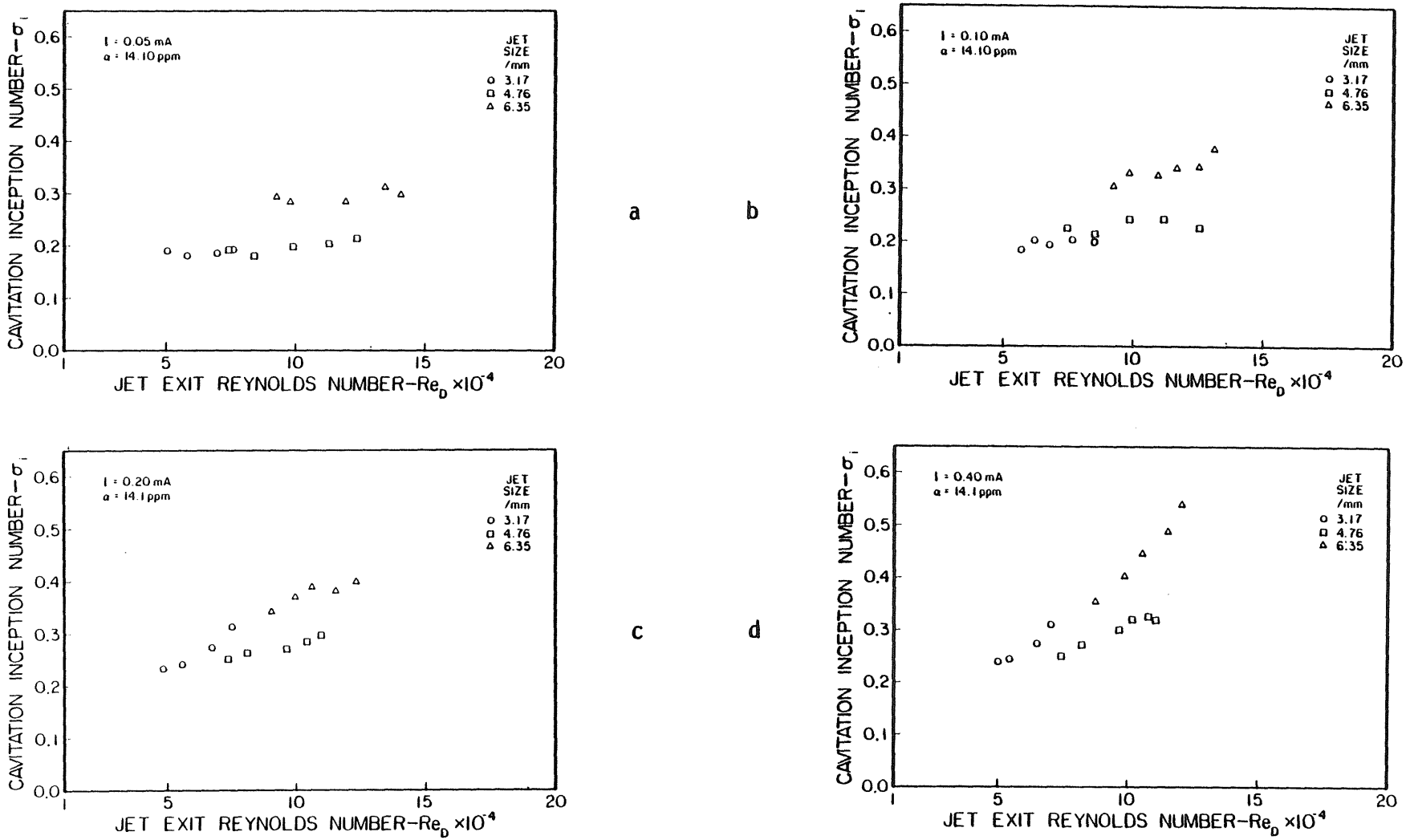

Fig. 5.17. Graph of σ_i versus Re_D showing the influence of jet size on the incipient cavitation index at α = 14.1ppm: (a) I = 0.05mA, (b) I = 0.10mA, (c) I = 0.20mA, and (d) I = 0.40mA.

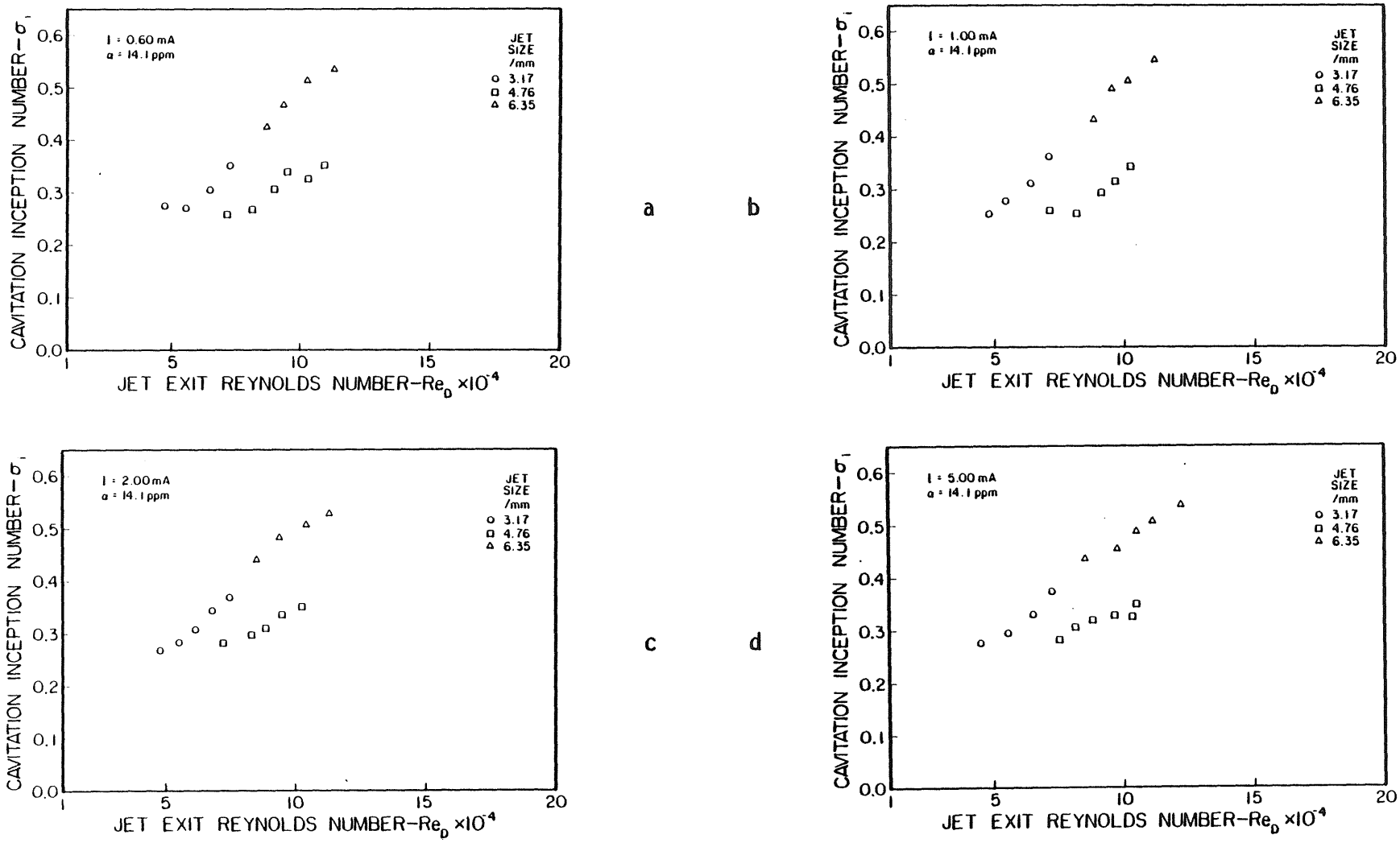

Fig. 5.18. Graph of σ_i versus Re_D showing the influence of jet size on the incipient cavitation index at $\bar{\alpha}$ = 14.1ppm: (a) I = 0.6mA, (b) I = 1.0mA, (c) I = 2.0mA, and (d) I = 5.0mA.

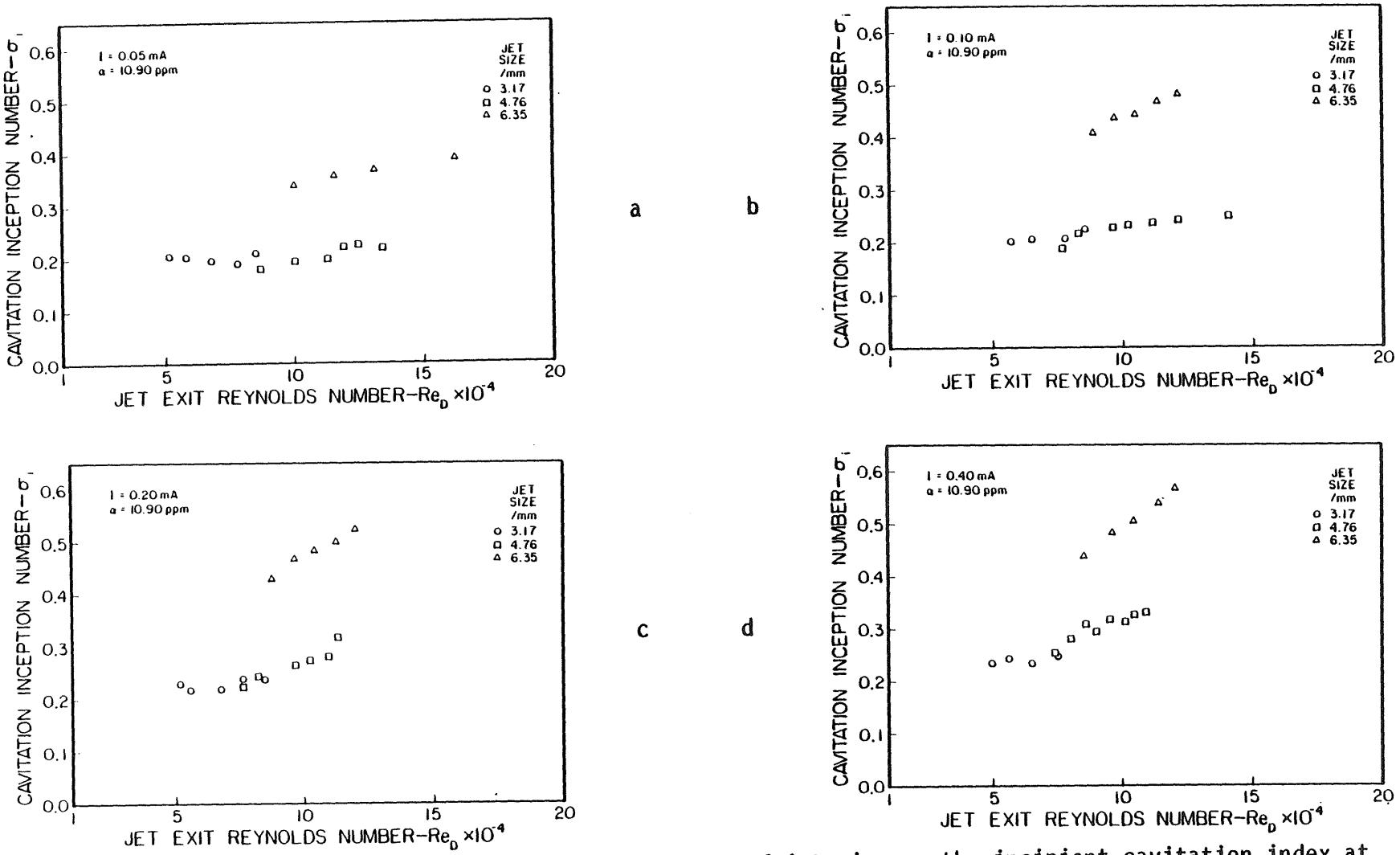

Fig. 5.19. Graph of σ_i versus Re_D showing the influence of jet size on the incipient cavitation index at α = 10.9ppm: (a) I = 0.05mA, (b) I = 0.10mA, (c) I = 0.20mA, and (d) I = 0.40mA.

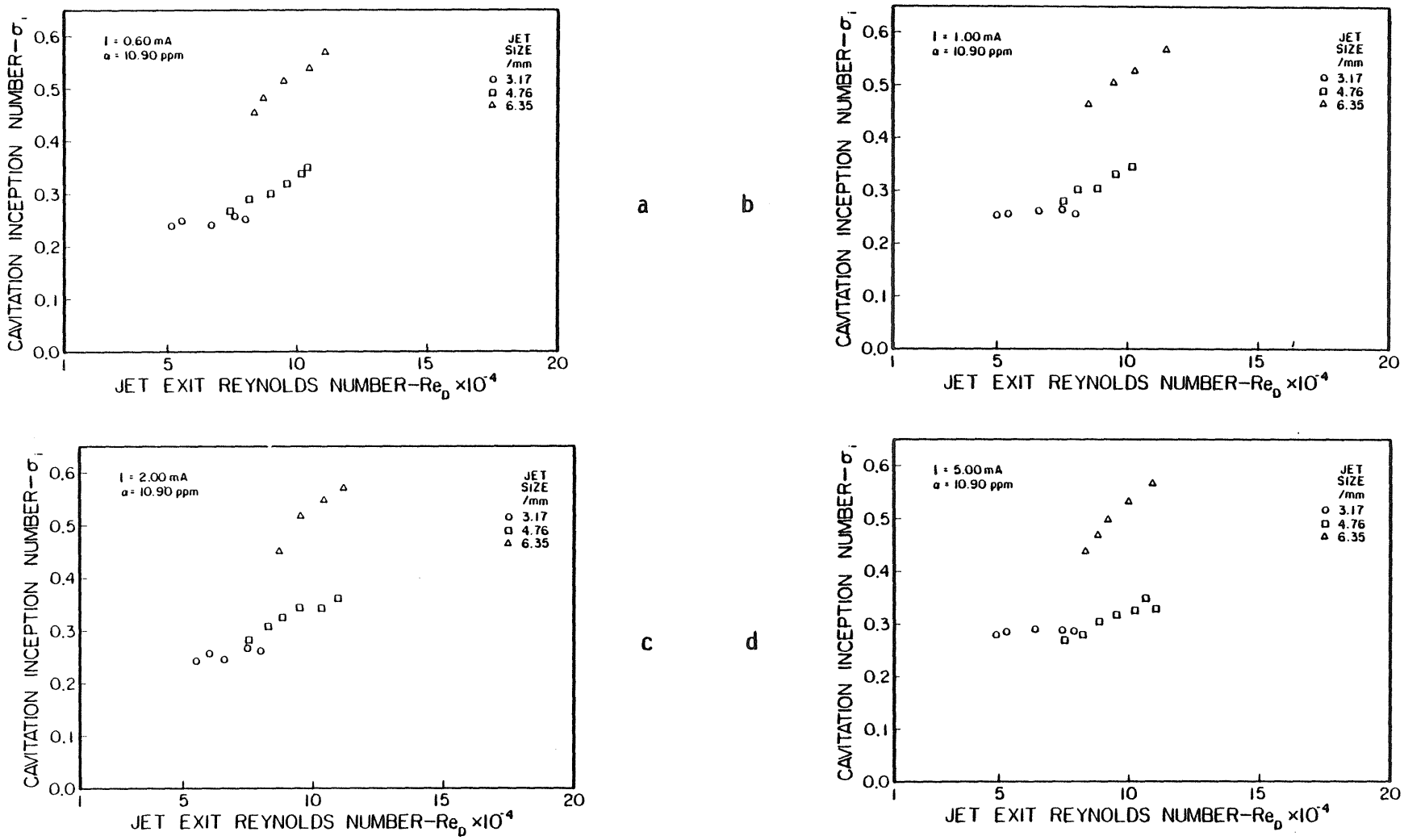

Fig. 5.20. Graph of σ_i versus Re_D showing the influence of jet size on the incipient cavitation index at $\bar{\alpha}$ = 10.9ppm: (a) I = 0.6mA, (b) I = 1.0mA, (c) I = 2.0mA, and (d) I = 5.0mA.

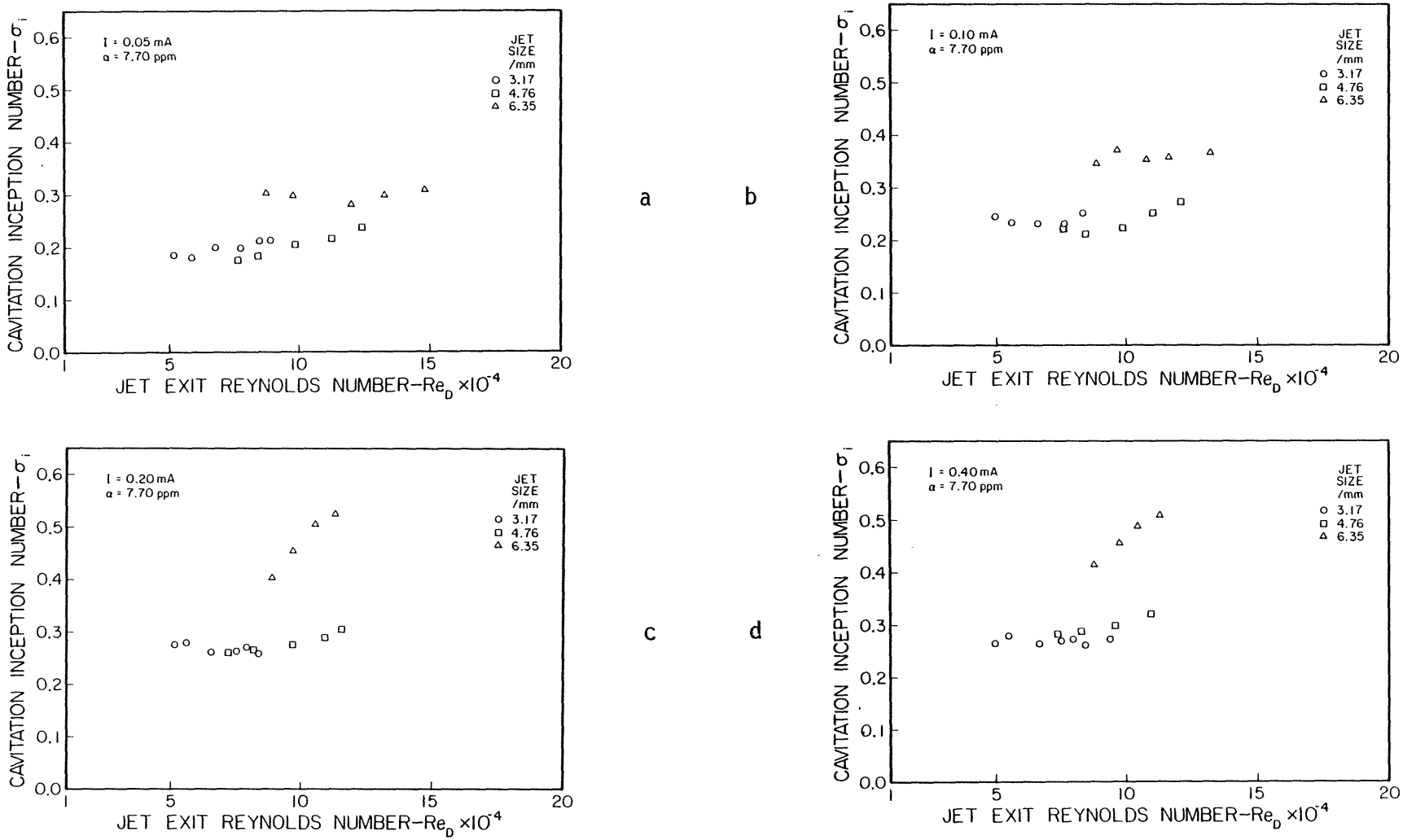

Fig. 5.21. Graph of σ_i versus Re_D showing the influence of jet size on the incipient cavitation index at $\overline{\alpha} = 7.7$ppm: (a) I = 0.05mA, (b) I = 0.10mA, (c) I = 0.20mA, and (d) I = 0.40mA.

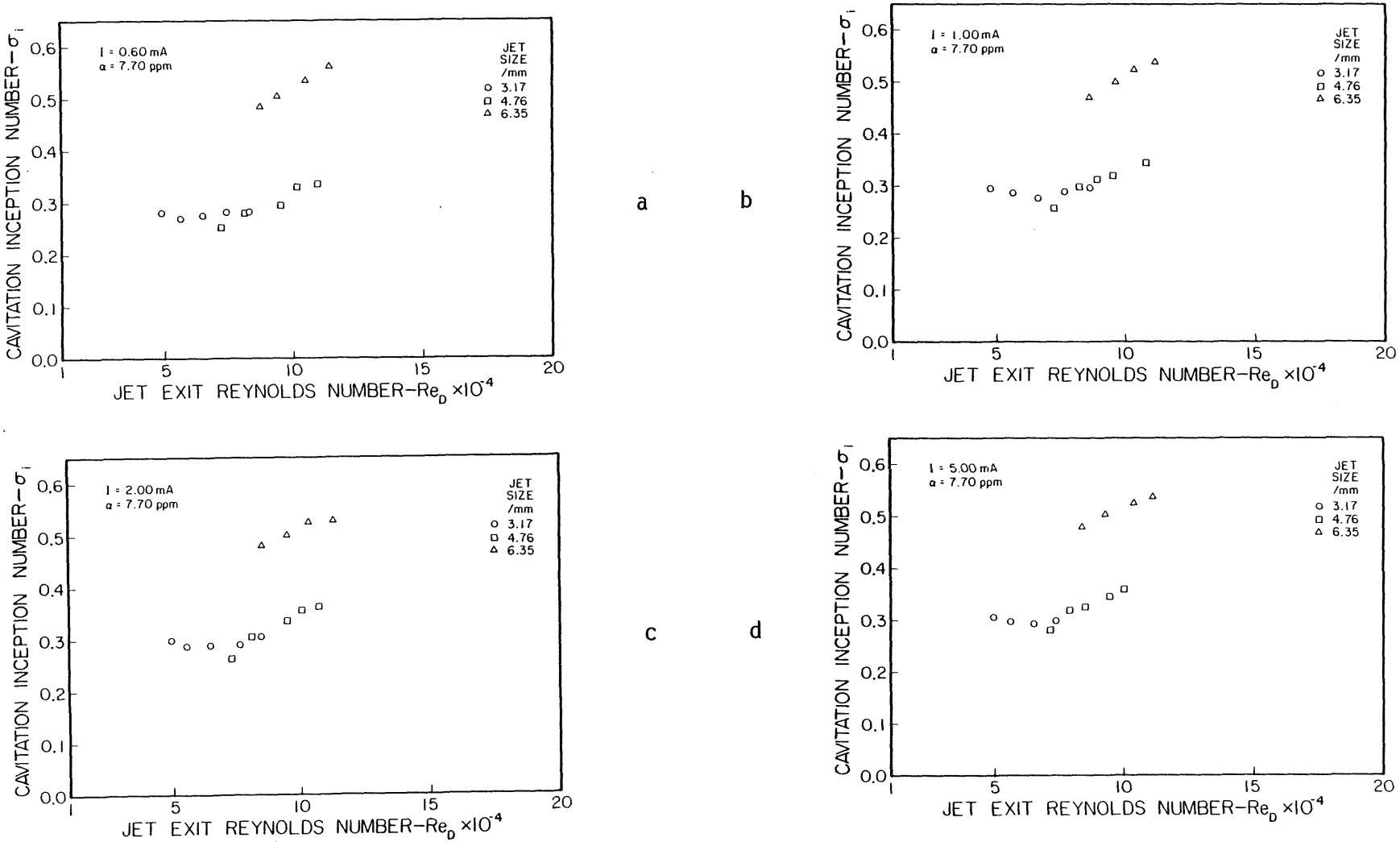

Fig. 5.22. Graph of σ_i versus Re_D showing the influence of jet size on the incipient cavitation index at $\overline{\alpha} = 7.7$ppm: (a) I = 0.6mA, (b) I = 1.0mA, (c) I = 2.0mA, and (d) I = 5.0mA.

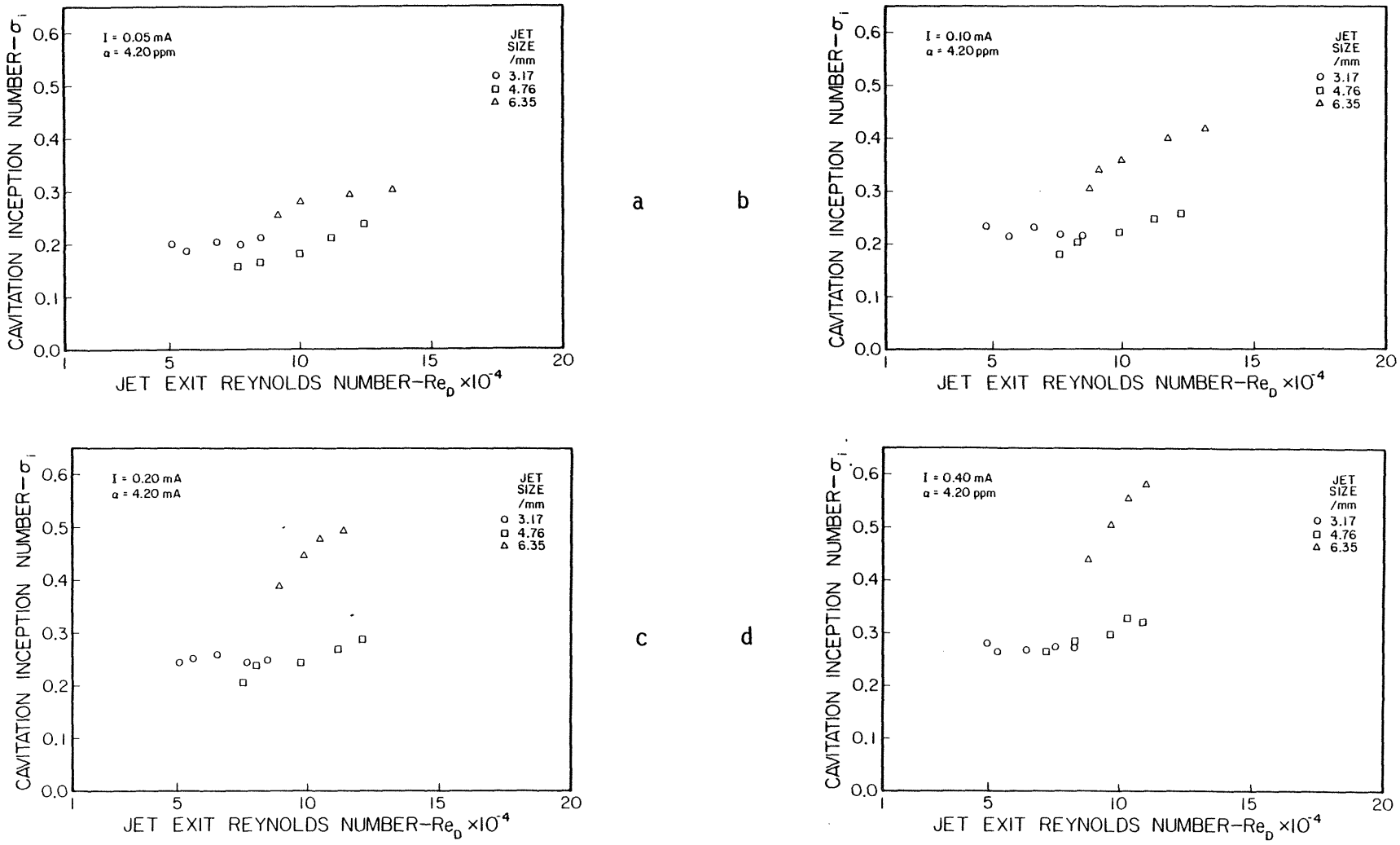

Fig. 5.23. Graph of σ_i versus Re_D showing the influence of jet size on the incipient cavitation index at α = 4.2ppm: (a) I = 0.05mA, (b) I = 0.10mA, (c) I = 0.20mA, and (d) I = 0.40mA.

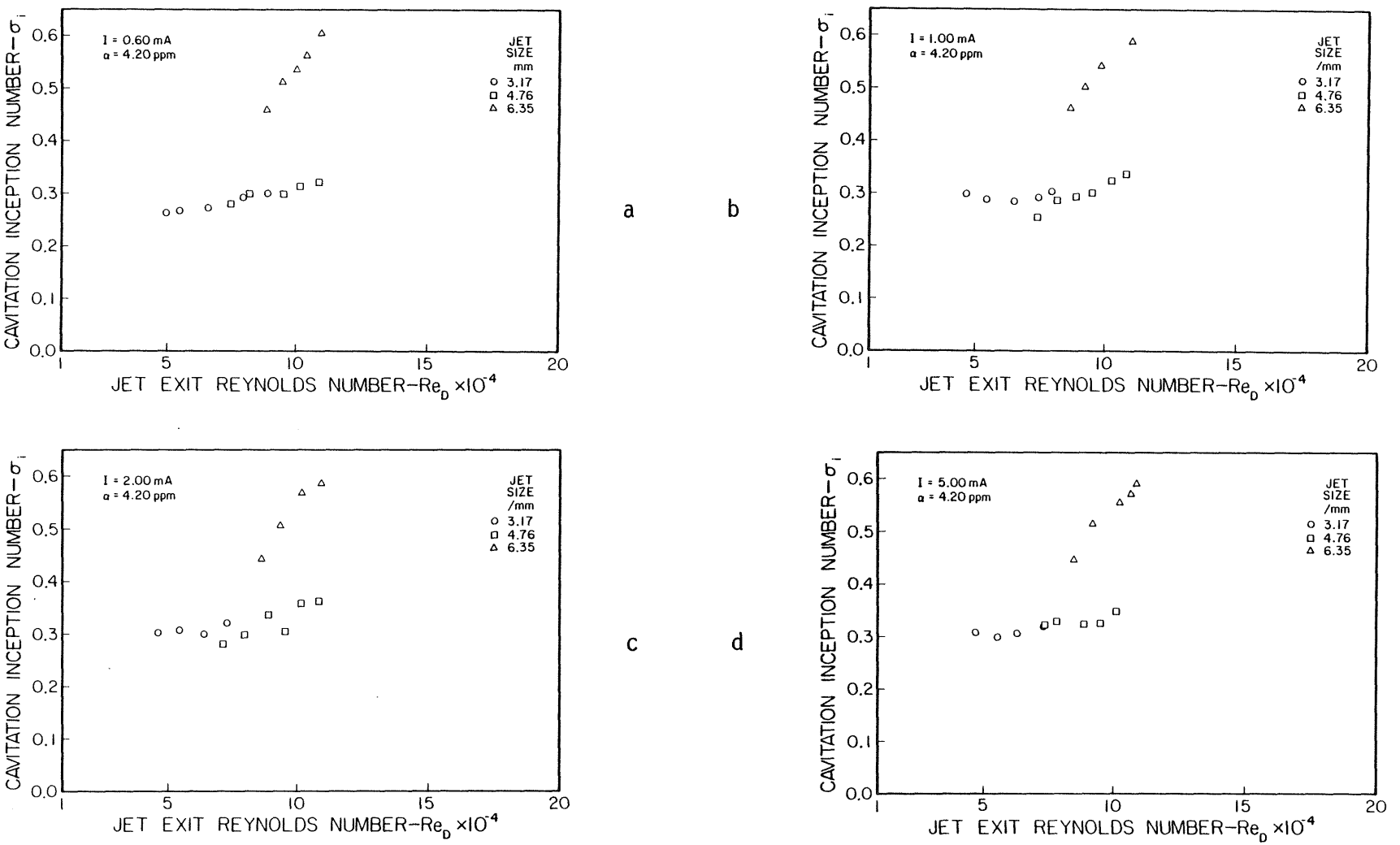

Fig. 5.24. Graph of σ_i versus Re_D showing the influence of jet size on the incipient cavitation index at $\alpha = 4.2$ppm: (a) I = 0.6mA, (b) I = 1.0mA, (c) I = 1.0mA, and (d) I = 5.0mA.

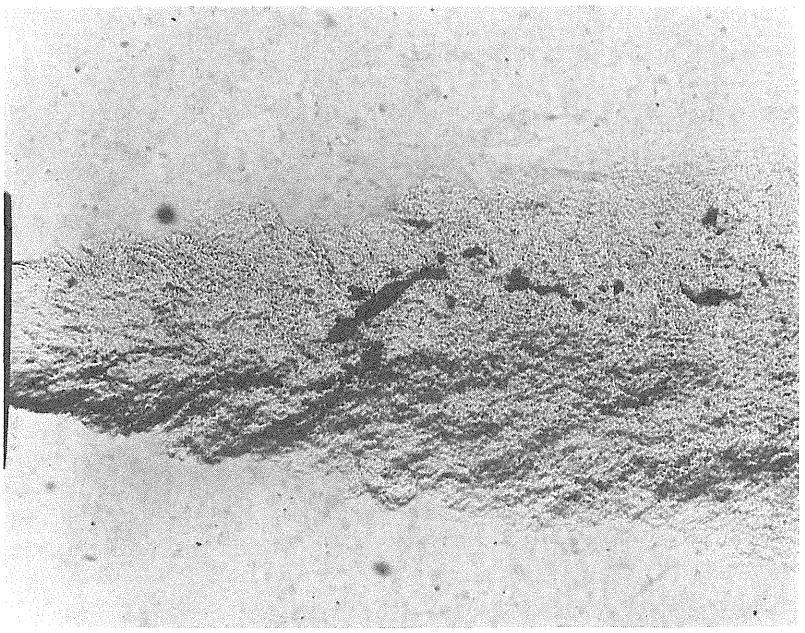

Fig. 5.25. Schlieren photograph of cavitation inception in the 6.35mm diameter jet at $Re_D = 1.63 \times 10^5$ and $\sigma_i = 0.25$.

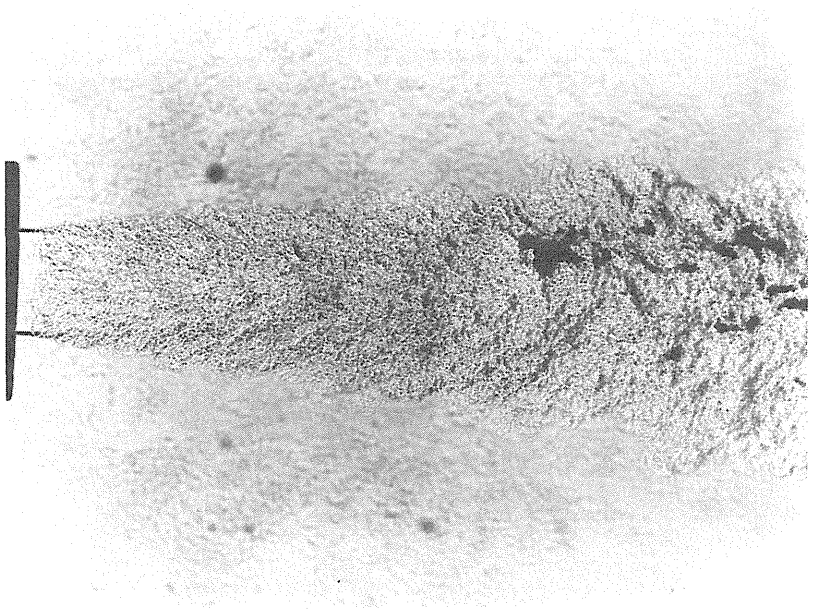

Fig. 5.26. Schlieren photograph of cavitation inception in the 4.76mm diameter jet at $Re_D = 1.40 \times 10^5$ and $\sigma_i = 0.16$.

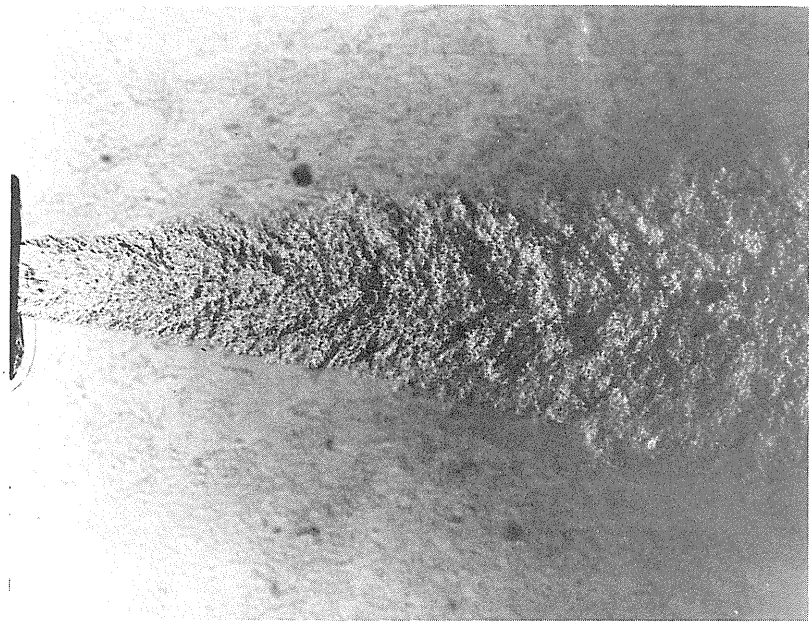

Fig. 5.27. Schlieren photograph of cavitation inception in the 3.17mm diameter jet at $Re_D = 1.02 \times 10^5$ and $\sigma_i = 0.15$.

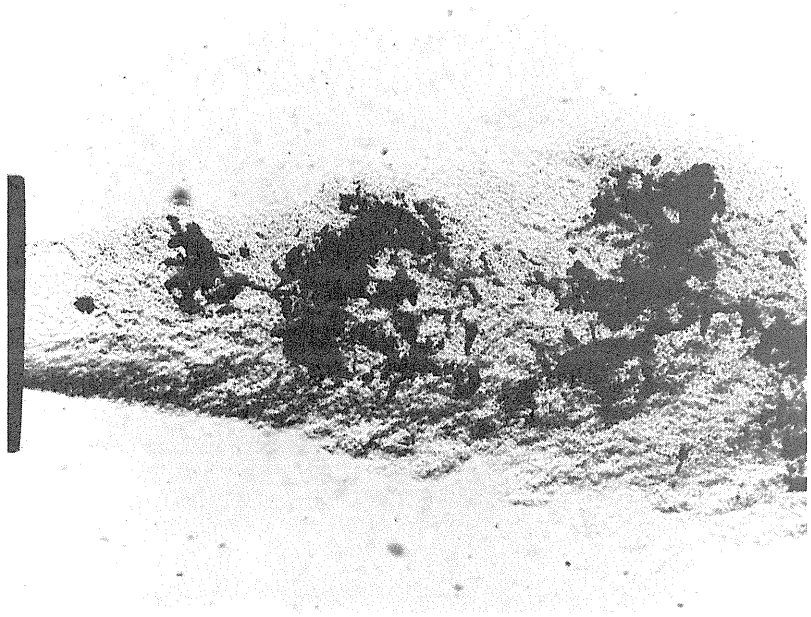

Fig. 5.28. Schlieren photograph taken at the onset of the almost "continuous popping sound" state of cavity development in the 6.35mm jet at $Re_D = 1.29 \times 10^5$ and $\sigma = 0.19$.

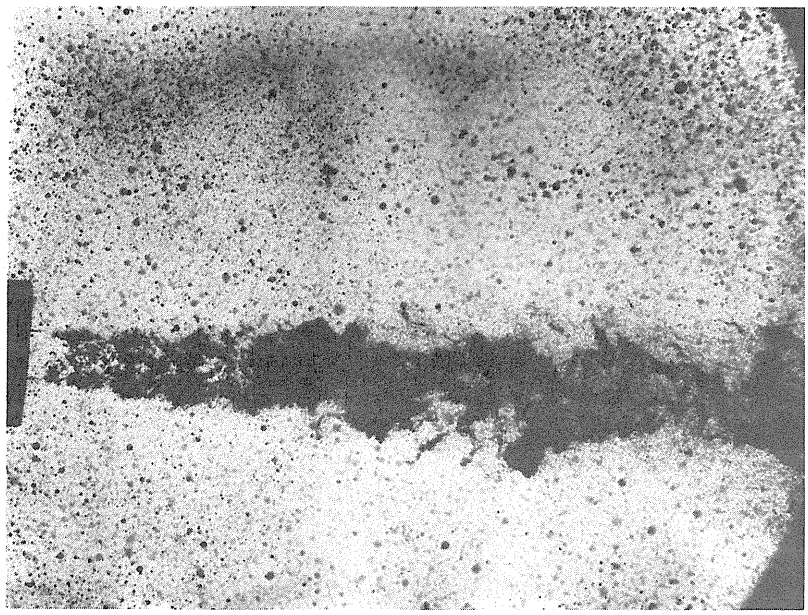

Fig. 5.29(a). Schlieren photograph of a fully cavitating 3.17mm diameter jet at a $Re_D = 1.04 \times 10^5$ and $\sigma = 0.04$.

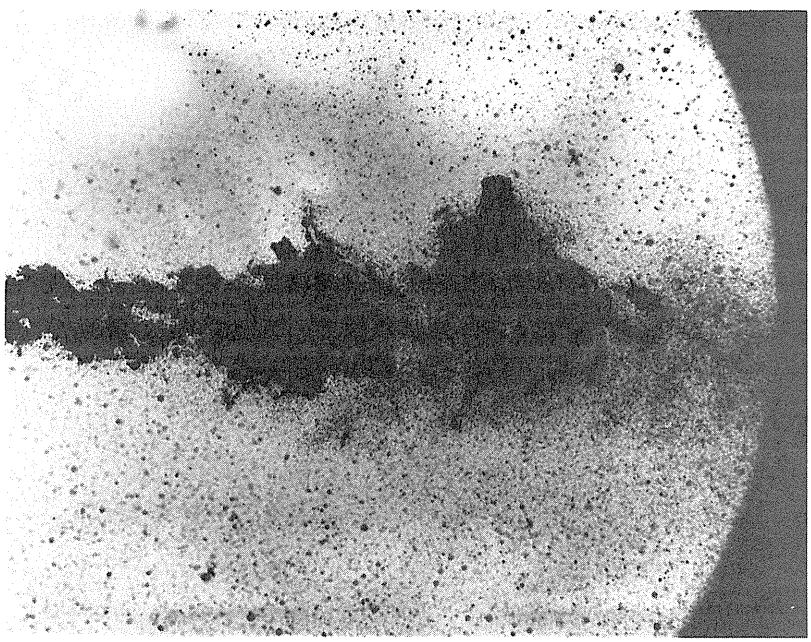

Fig. 5.29(b). Schlieren photograph of the same jet as in (a) above showing the region where the cavity collapsed.

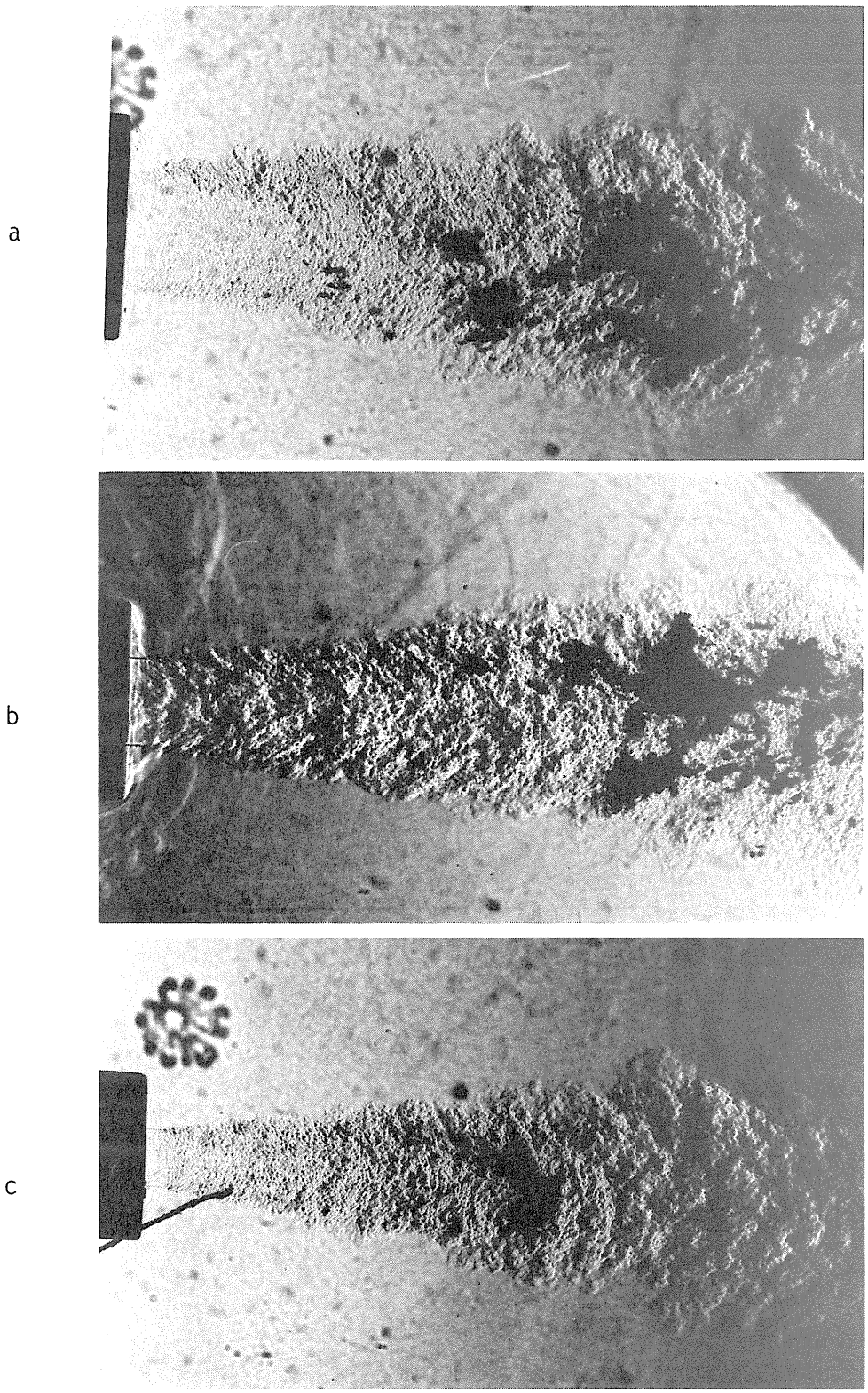

Fig. 5.30. Schlieren photographs of cavitation inception in (a) 6.35mm jet at $Re_D = 2.06 \times 10^5$ and $\sigma_i = 0.22$, (b) 4.76mm jet at $Re_D = 1.47 \times 10^5$ and $\sigma_i = 0.09$, (c) 3.17mm jet at $Re_D = 8.35 \times 10^4$ and $\sigma_i = 0.08$. The dissolved air content is 7.7ppm.

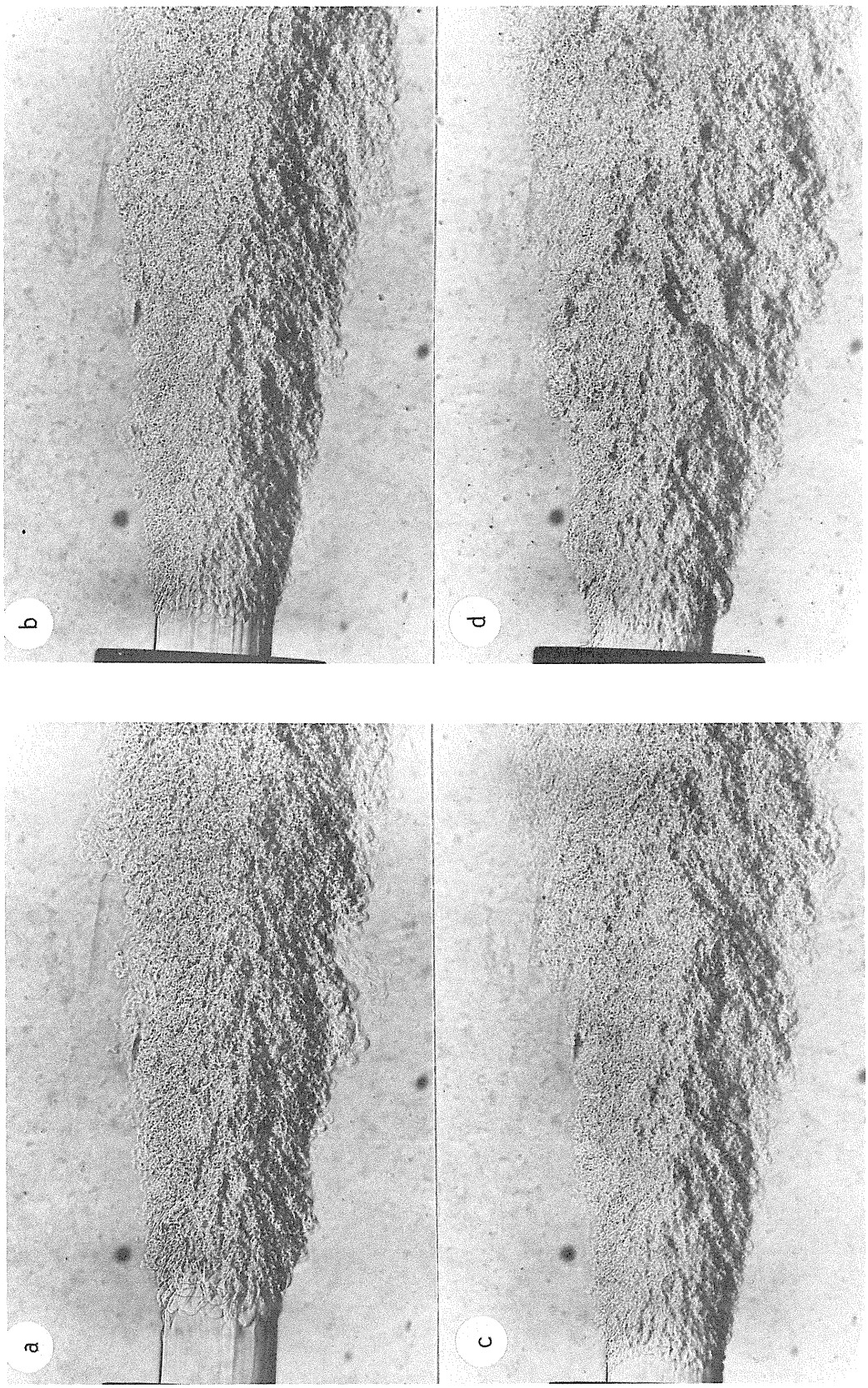

Fig. 5.31. Schlieren photographs of the non-cavitating 6.35 jet taken with knife edge parallel to the flow direction: (a) $Re_D = 3.03 \times 10^4$, (b) $Re_D = 7.20 \times 10^4$, (c) $Re_D = 1.00 \times 10^5$, (d) $Re_D = 1.57 \times 10^5$.

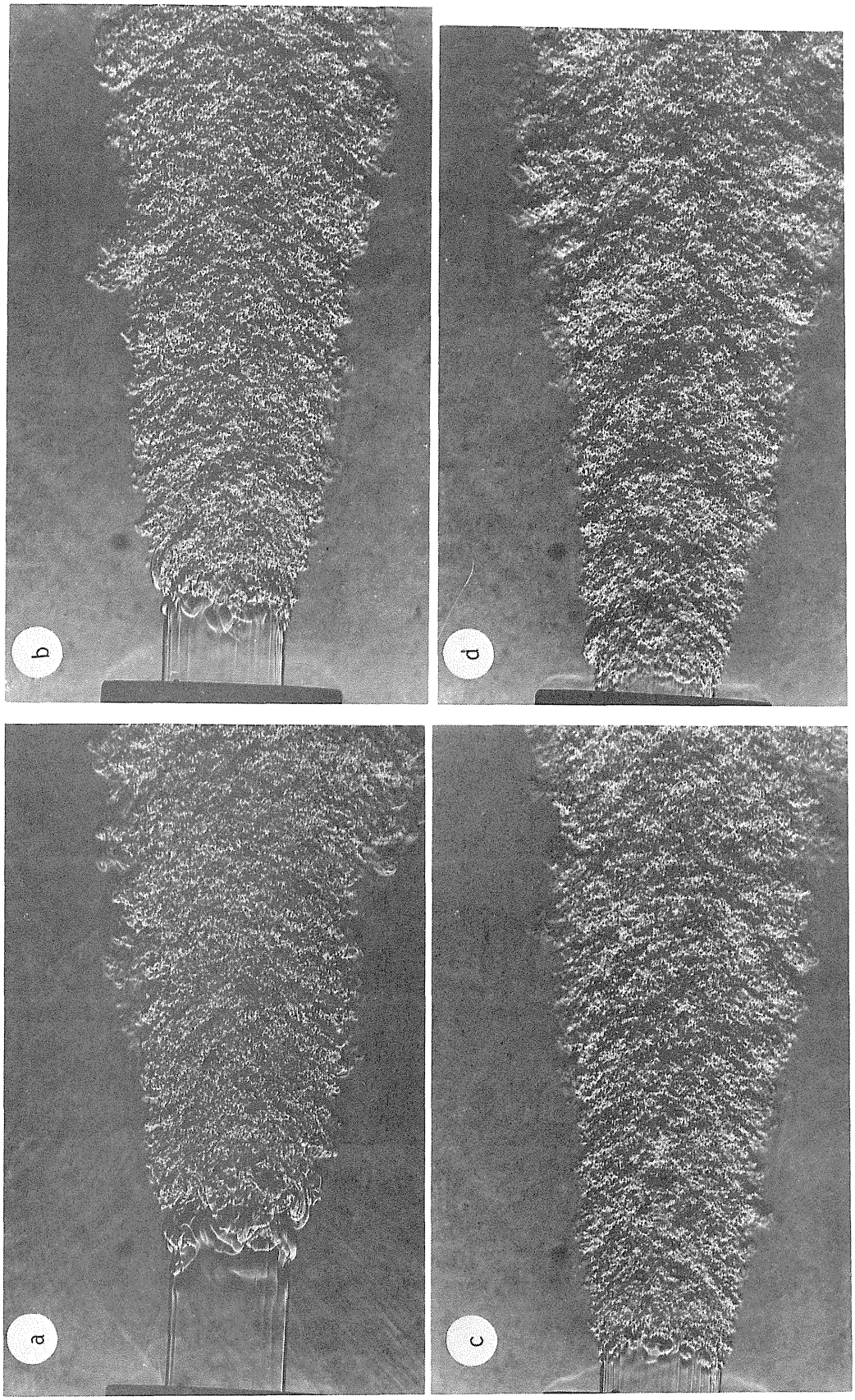

Fig. 5.32. Schlieren photographs of the non-cavitating 6.35 jet taken with the knife edge perpendicular to the flow direction: (a) $Re_D = 1.06 \times 10^4$, (b) $Re_D = 3.20 \times 10^4$, (c) $Re_D = 6.81 \times 10^4$ (d) $Re_D = 1.64 \times 10^5$.

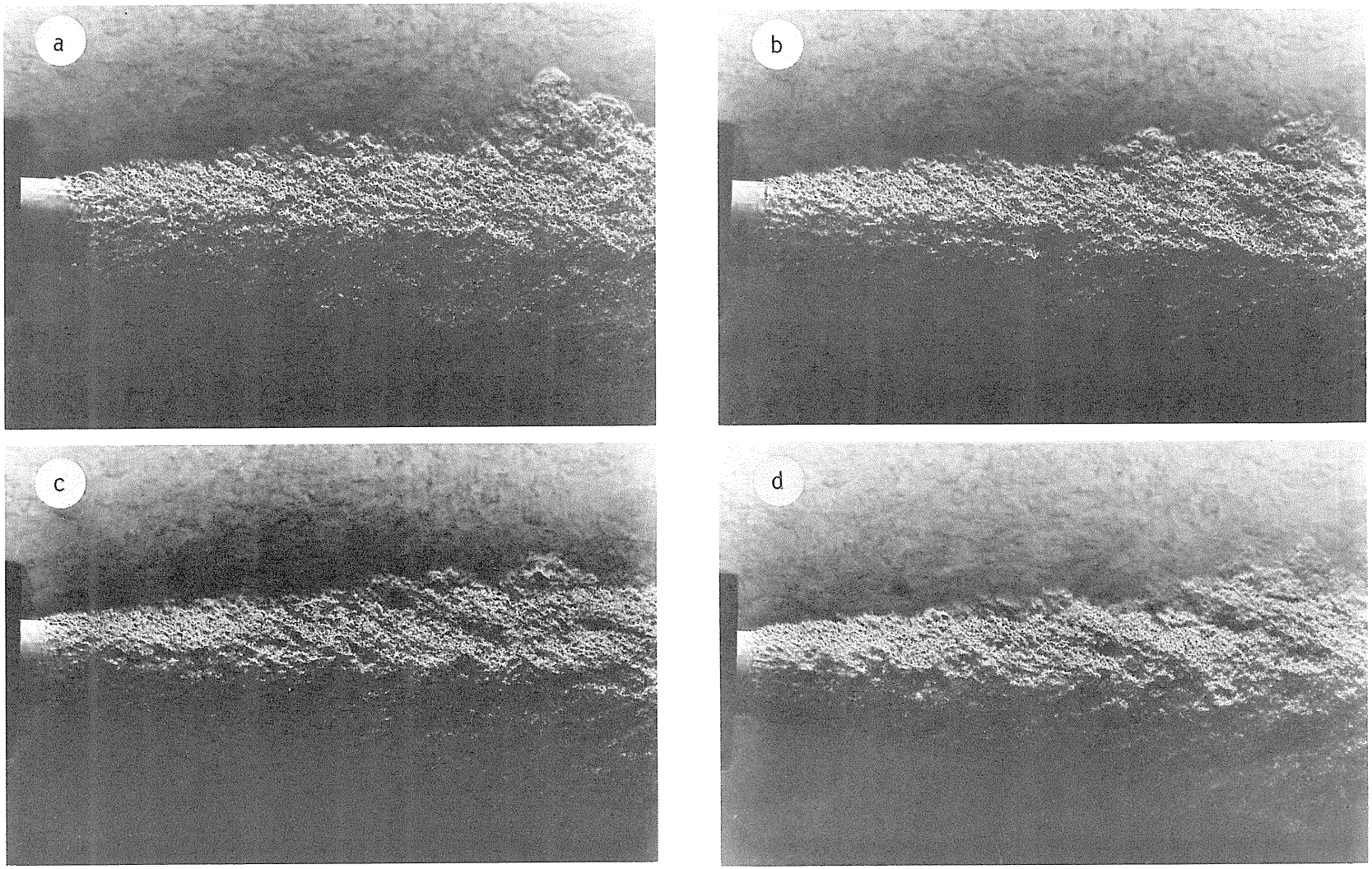

Fig. 5.33. Schlieren photographs of the non-cavitating 4.76mm jet taken with the knife edge parallel to the flow direction: (a) $Re_D = 3.14 \times 10^4$, (b) $Re_D = 5.94 \times 10^4$, (c) $Re_D = 8.2 \times 10^4$, (d) $Re_D = 1.58 \times 10^5$.

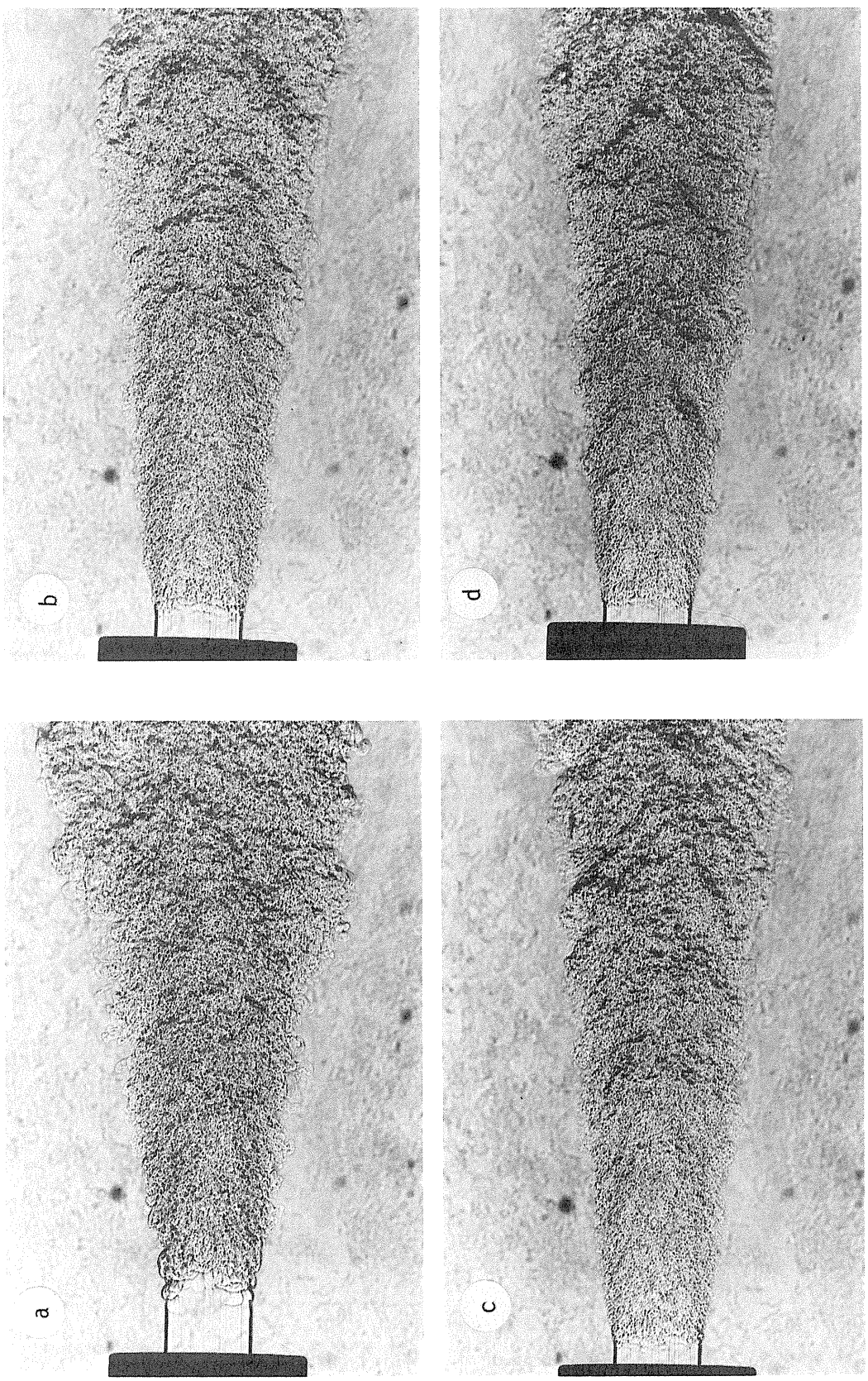

Fig. 5.34. Schlieren photographs of the non-cavitating 4.76mm jet taken with the knife edge perpendicular to the flow direction: (a) $Re_D = 2.3 \times 10^4$, (b) $Re_D = 5.08 \times 10^4$, (c) $Re_D = 8.14 \times 10^4$, (d) $Re_D = 1.01 \times 10^5$.

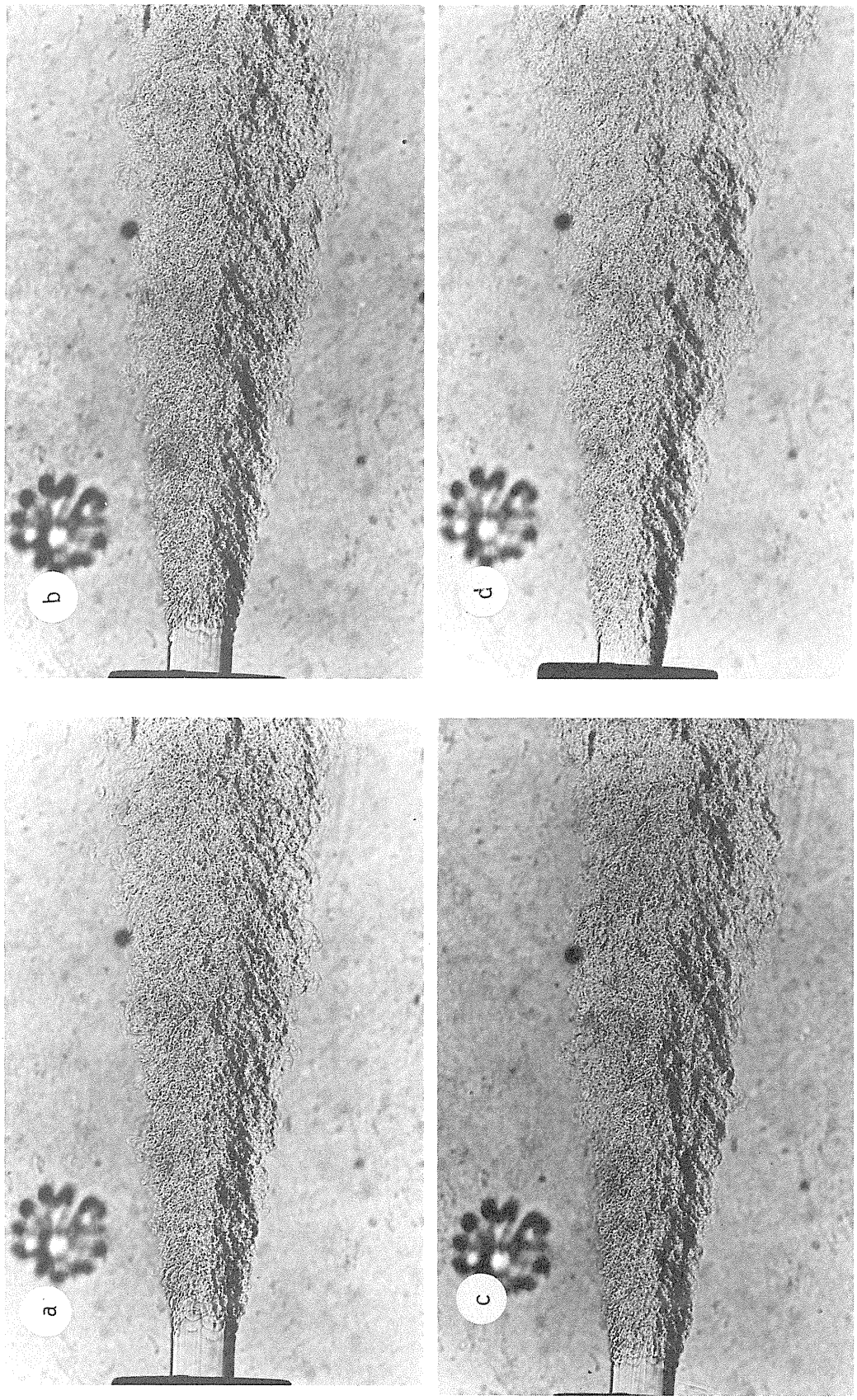

Fig. 5.35. Schlieren photographs of the non-cavitating 3.17mm jet taken with the knife edge parallel to the flow direction: (a) $Re_D = 1.50 \times 10^4$, (b) $Re_D = 3.57 \times 10^4$, (c) $Re_D = 4.48 \times 10^4$, (d) $Re_D = 7.67 \times 10^4$.

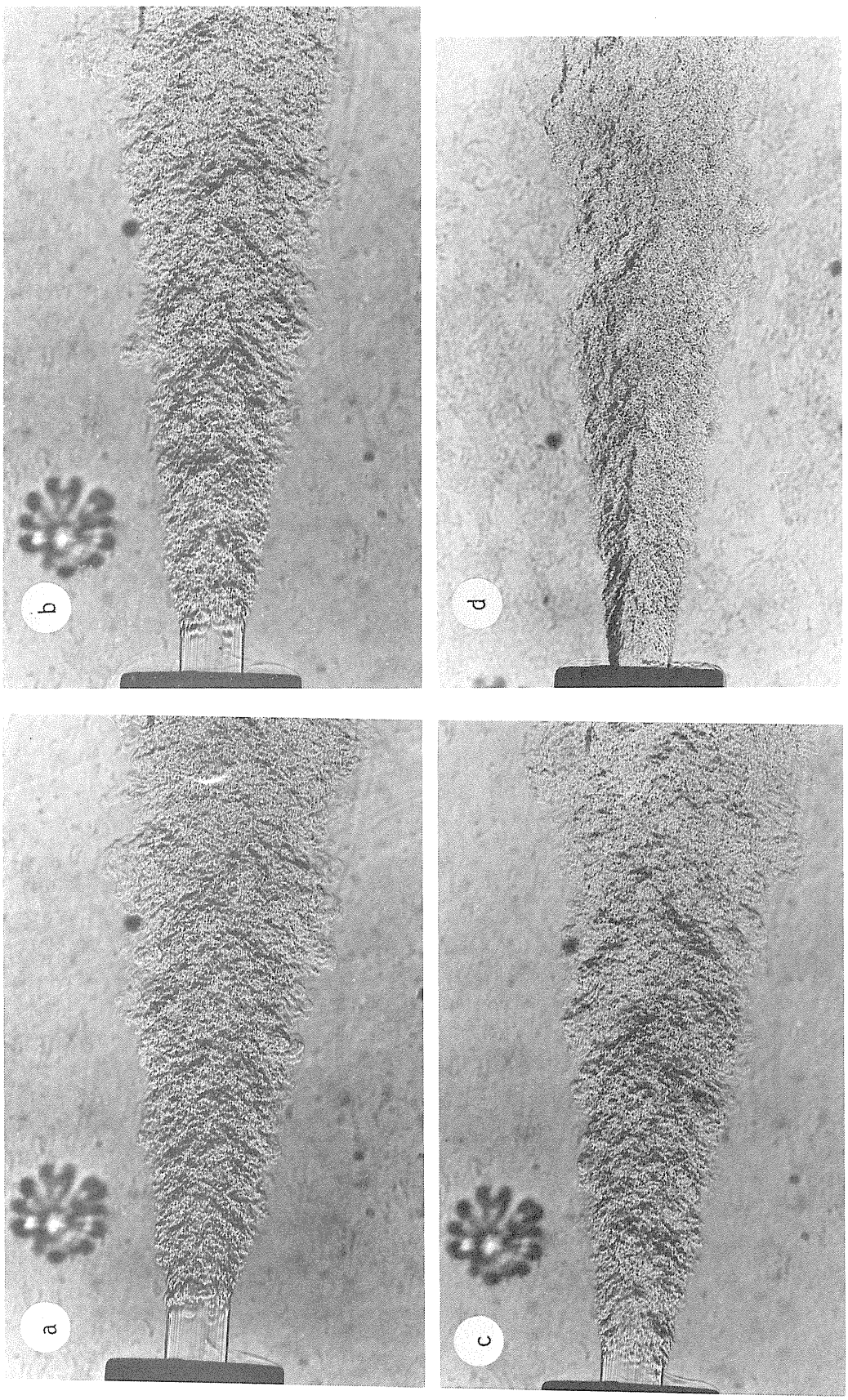

Fig. 5.36. Schlieren photographs of the non-cavitating 3.17mm jet taken with the knife edge perpendicular to the flow direction: (a) $Re_D = 1.41 \times 10^4$, (b) $Re_D = 3.36 \times 10^4$, (c) $Re_D = 7.32 \times 10^4$, (d) $Re_D = 9.53 \times 10^4$.

a

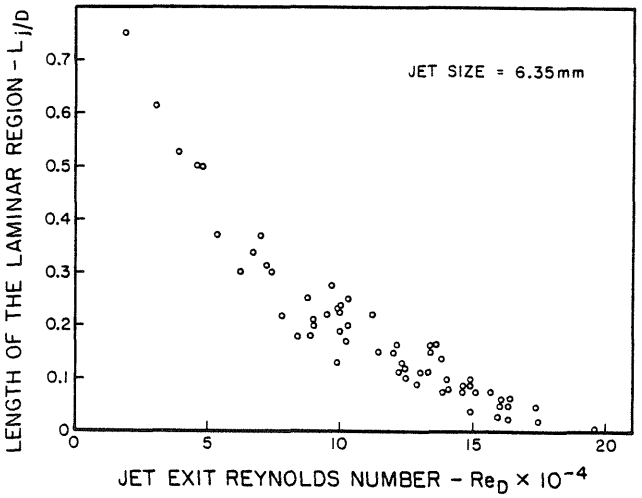

b

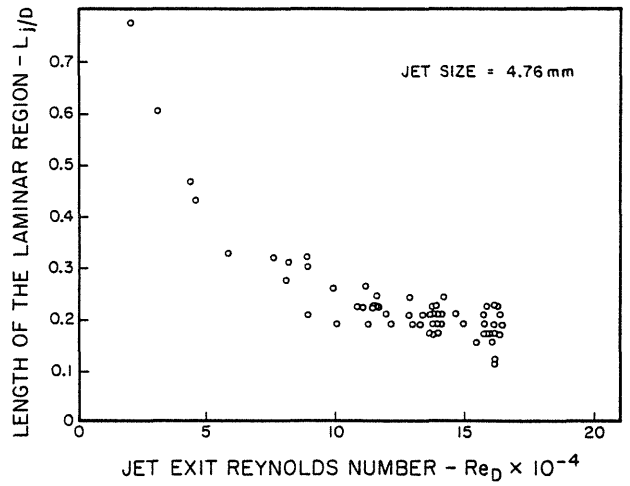

c

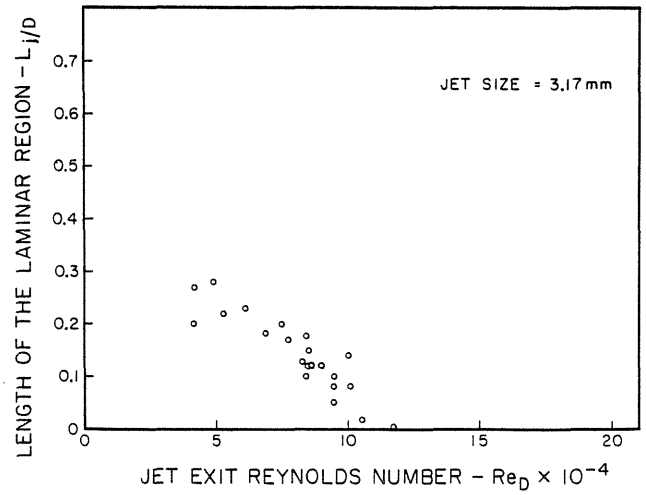

Fig. 5.37. Graphs of L_j/D vs Re_D for the (a) 6.35mm jet, (b) 4.76mm jet, and (c) 3.17mm jet.

a

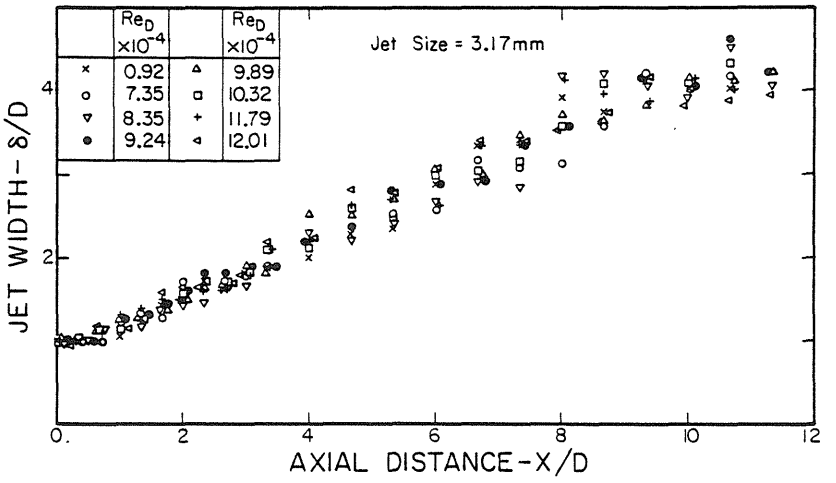

b

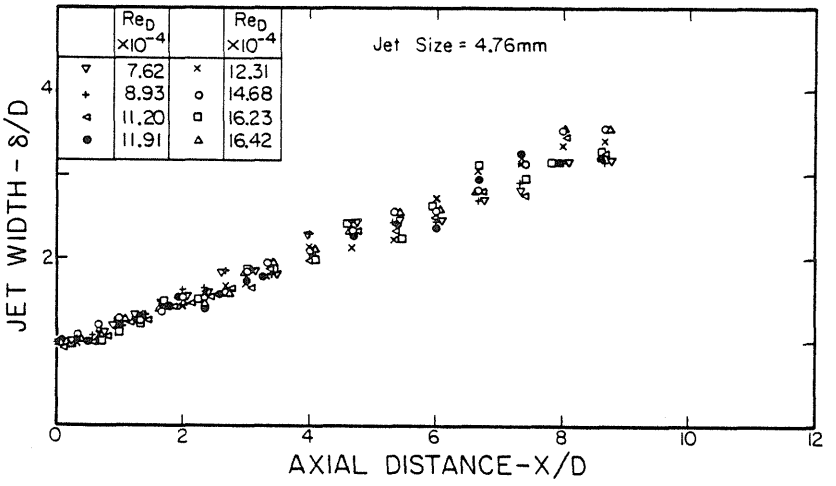

c

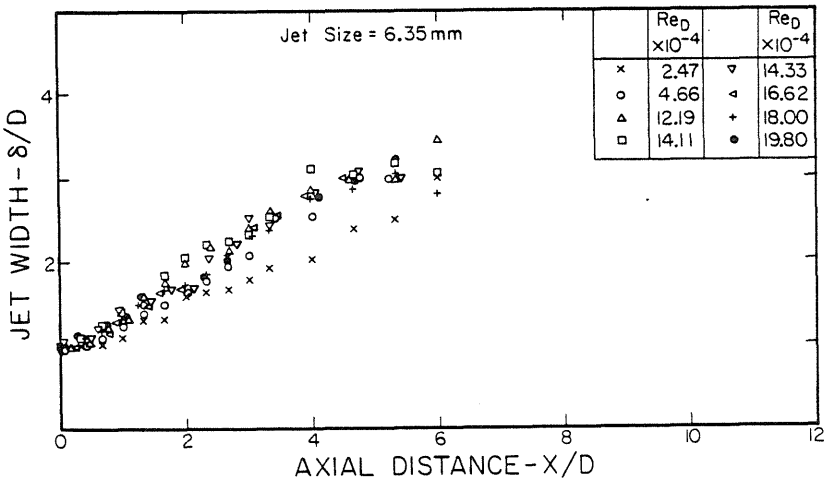

Fig. 5.38. Plots of the non-dimensional jet width δ/D versus the dimensionless axial position for the (a) 3.17mm jet, (b) 4.76mm jet, and (c) 6.35mm jet.

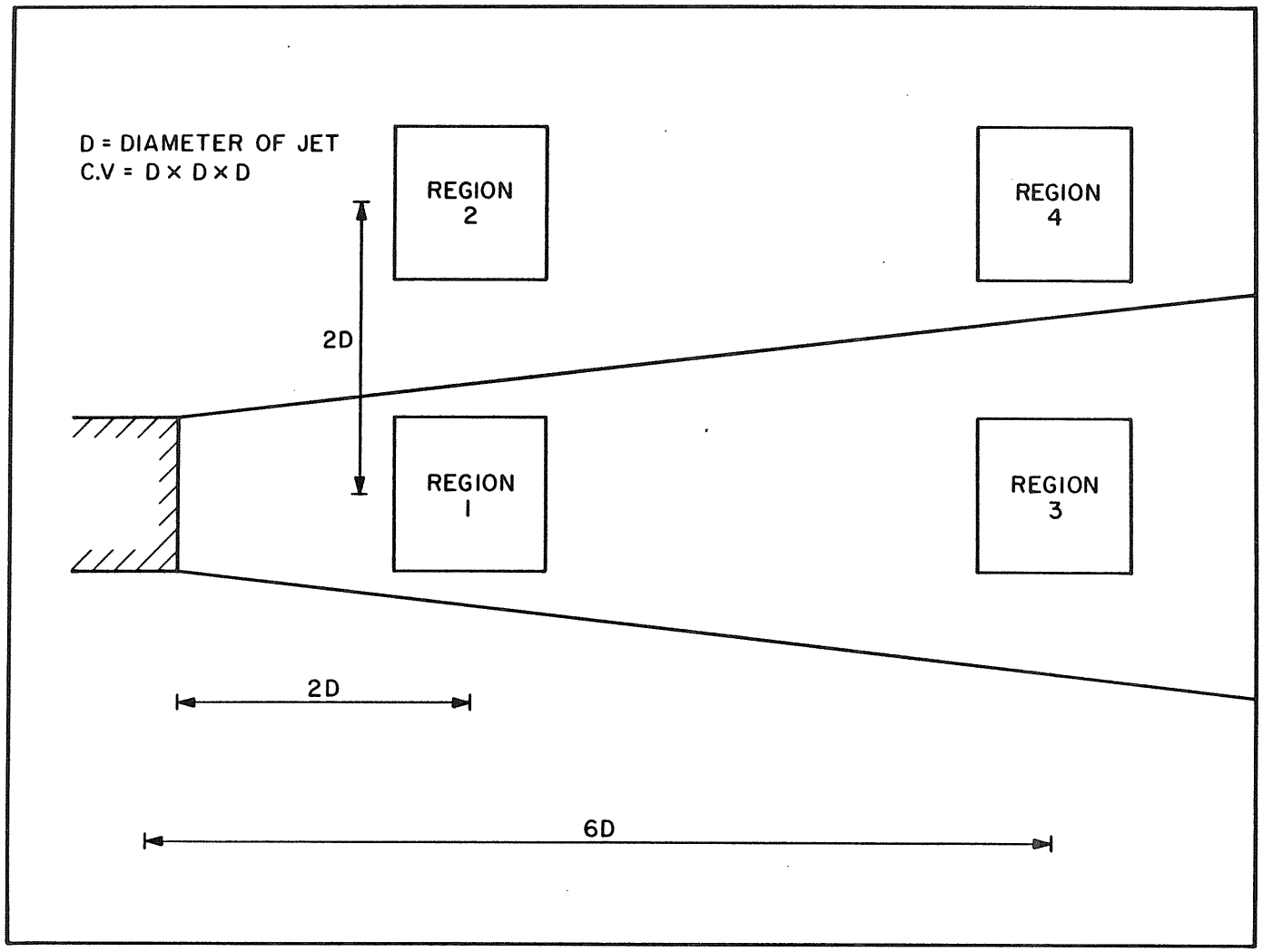

Fig. 5.39. A schematic drawing depicting the 4 regions in the jet where nuclei counts were carried out

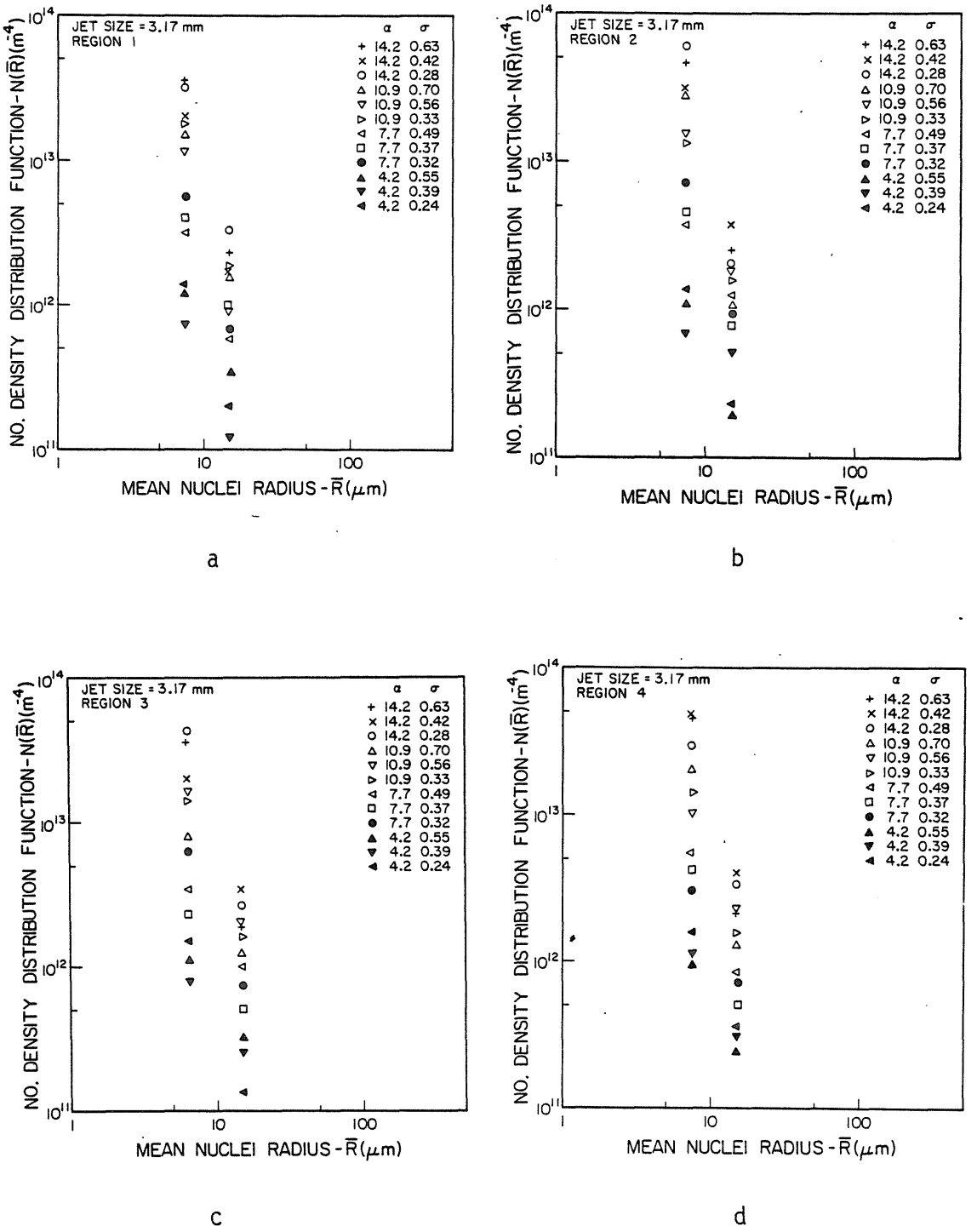

Fig. 5.40. Plots of the nuclei distributions for the 3.17mm jet: (a) Region 1, (b) Region 2, (c) Region 3, and (d) Region 4.

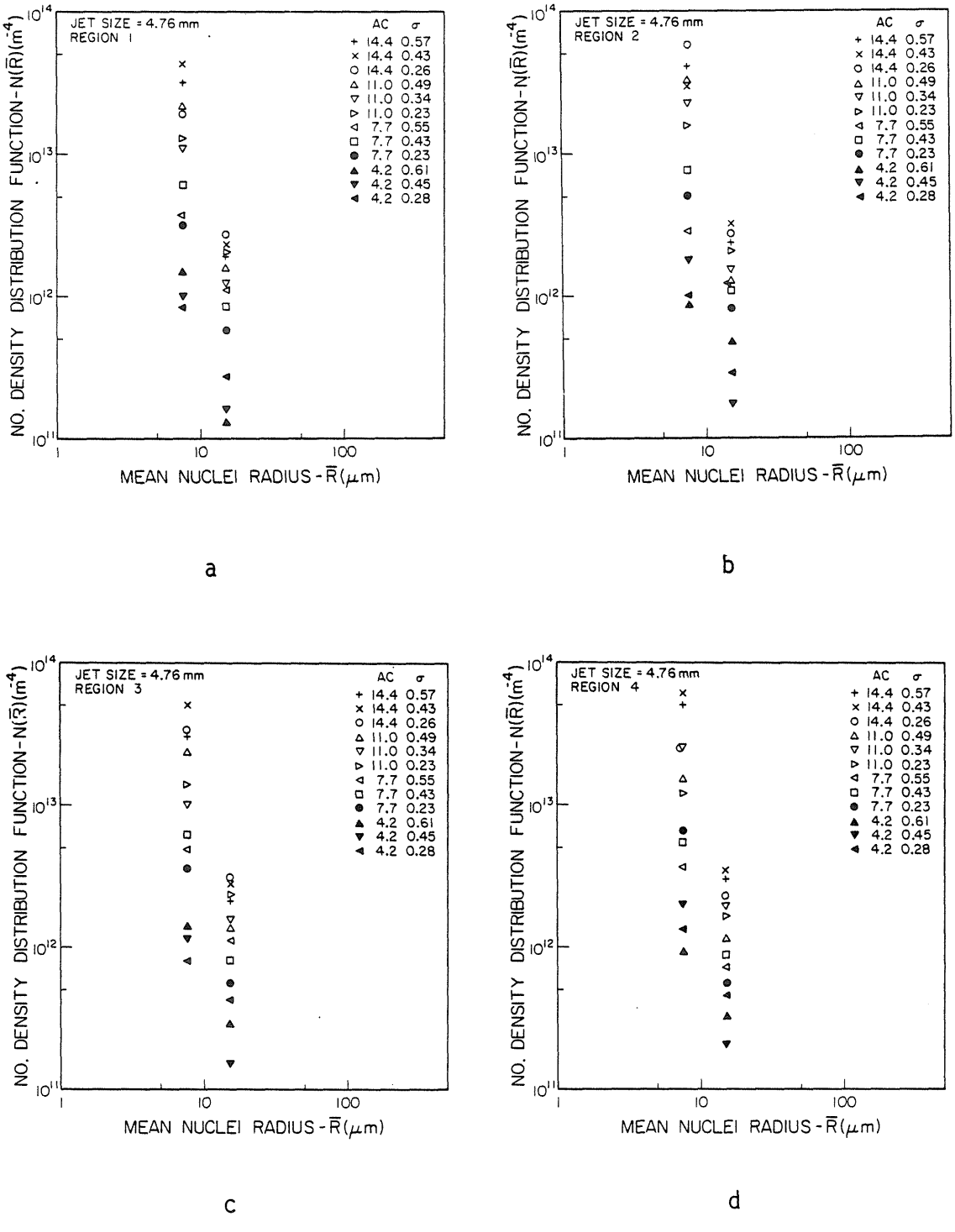

Fig. 5.41. Plots of the nuclei distributions for the 4.76mm jet: (a) Region 2, (c) Region 3, and (d) Region 4.

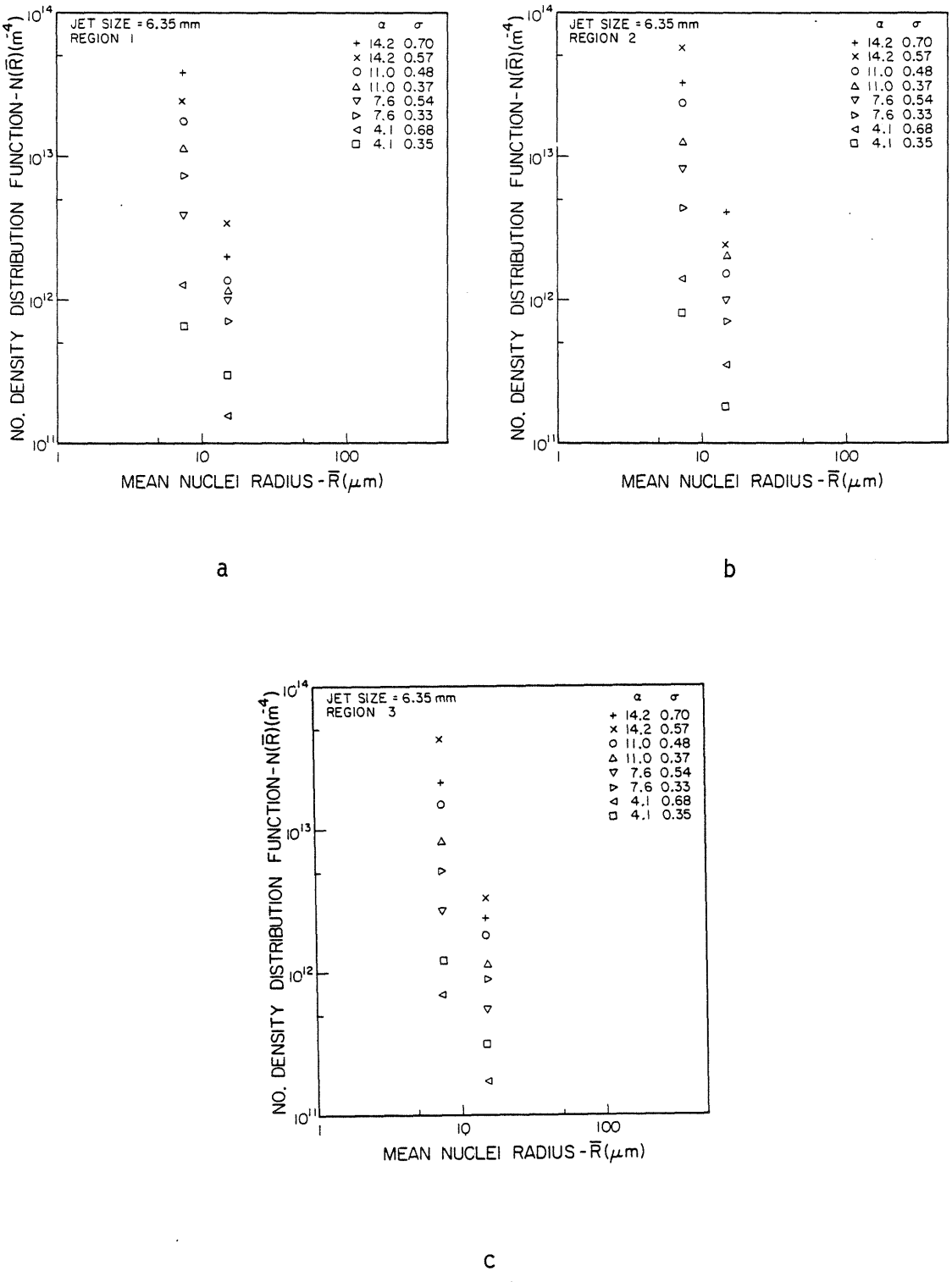

Fig. 5.42. Plots of the nuclei distributions for the 6.35 mm jet: (a) Region 1, (b) Region 2, (c) Region 3.

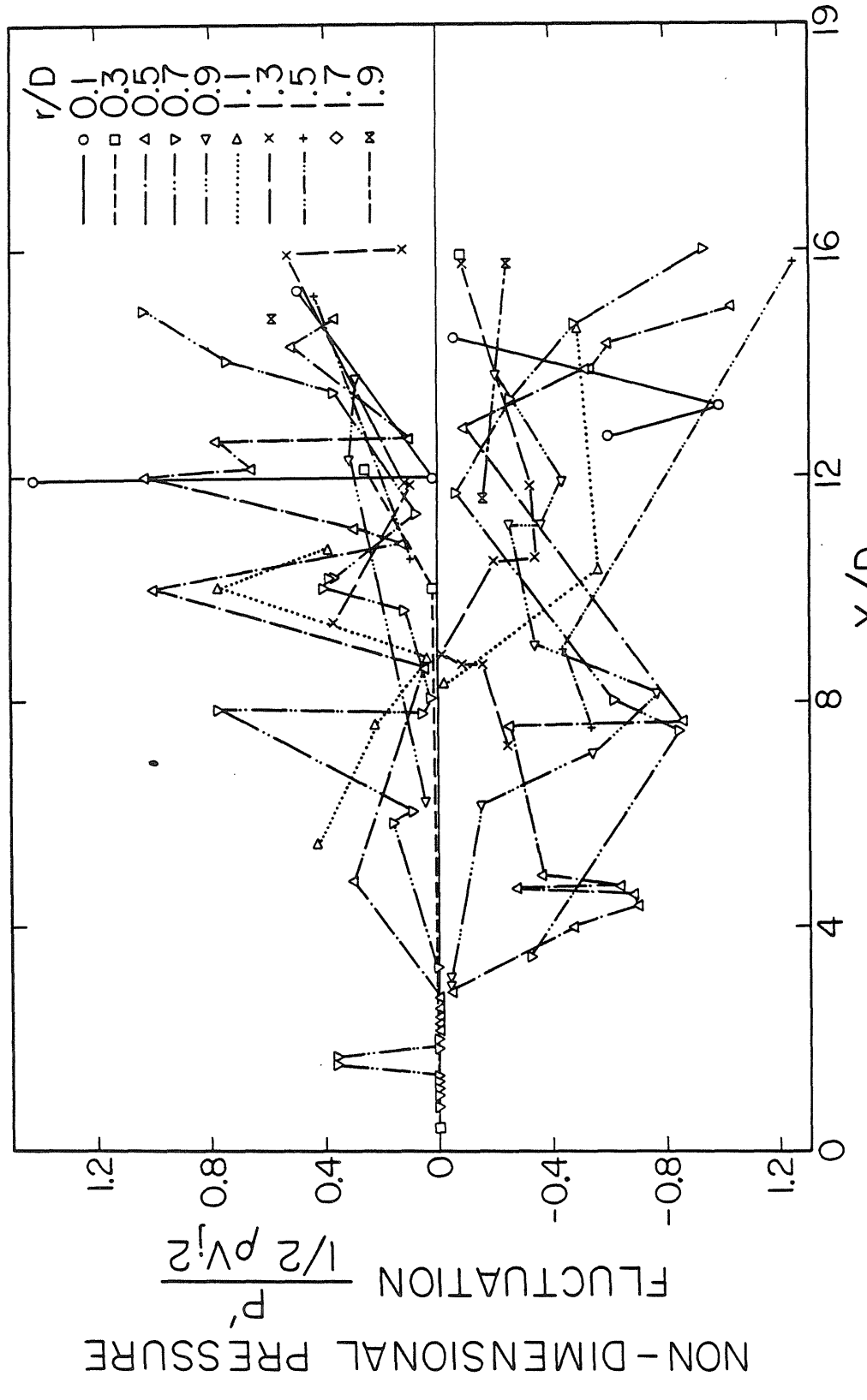

Fig. 5.43. Graphs of the instantaneous local pressure fluctuations as a function of the dimensionless axial position in the 3.17mm jet.

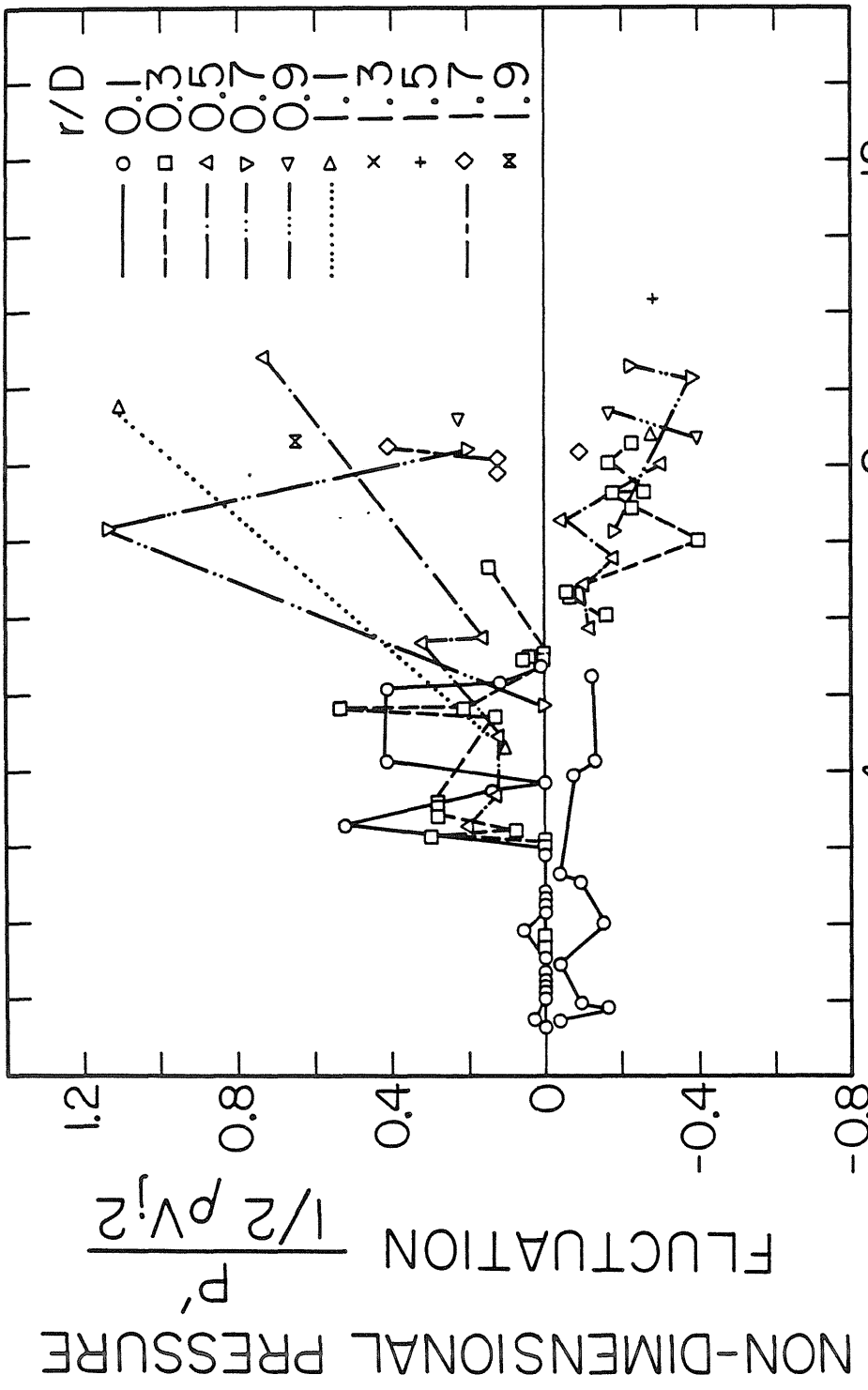

Fig. 5.44. Graphs of the instantaneous local pressure fluctuations as a function of the dimensionless axial position in the 4.76mm jet.

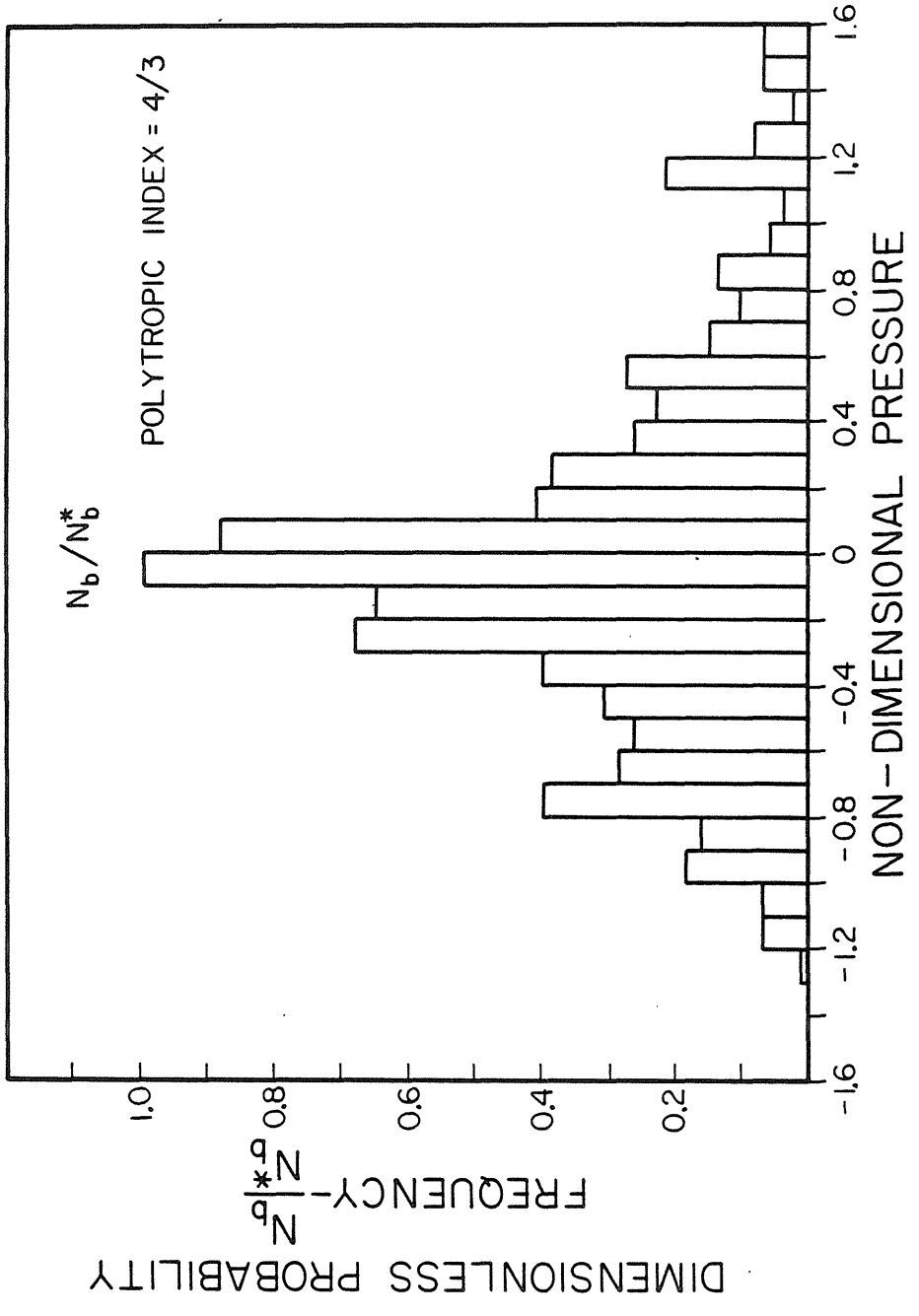

Fig. 5.45. Probability histogram showing the distribution of the pressure fluctuation intensities in a jet. (Polytropic index of 4/3)

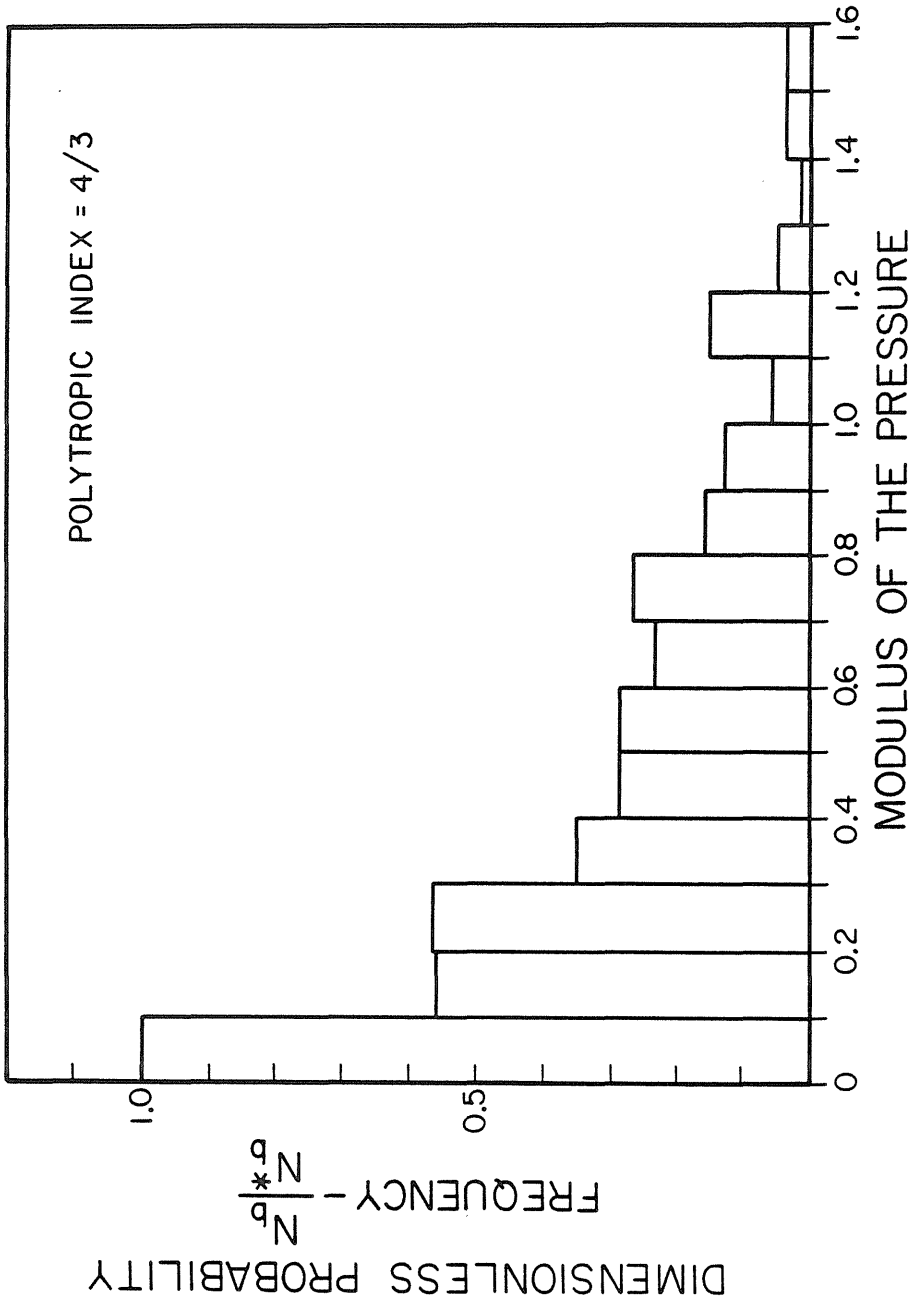

Fig. 5.46. Probability histogram showing the distribution of the modulus of pressure fluctuation intensities in a jet. (Polytropic index of 4/3).

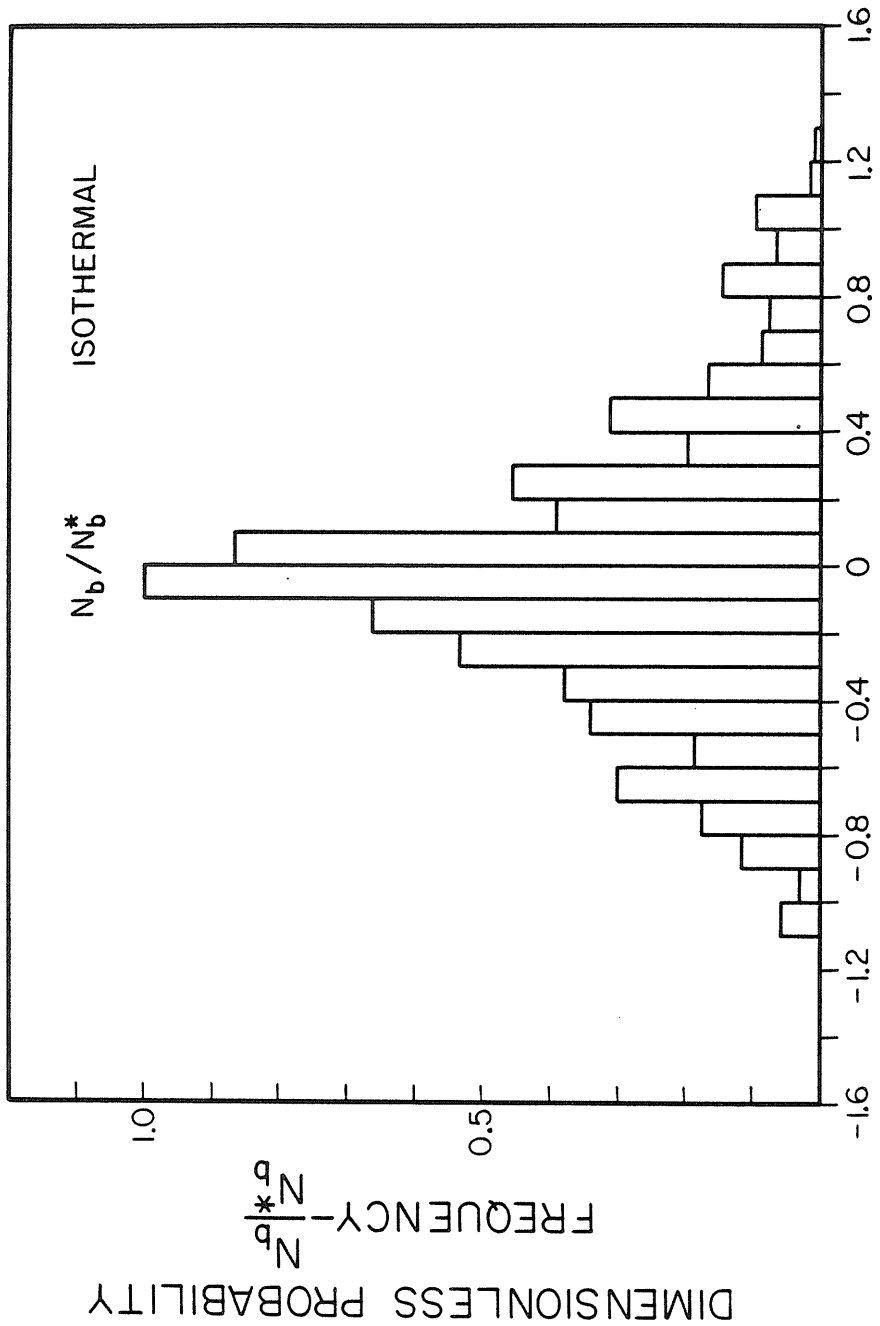

Fig. 5.47. Probability histogram showing the distribution of the pressure fluctuation intensities in a jet (Isothermal case).

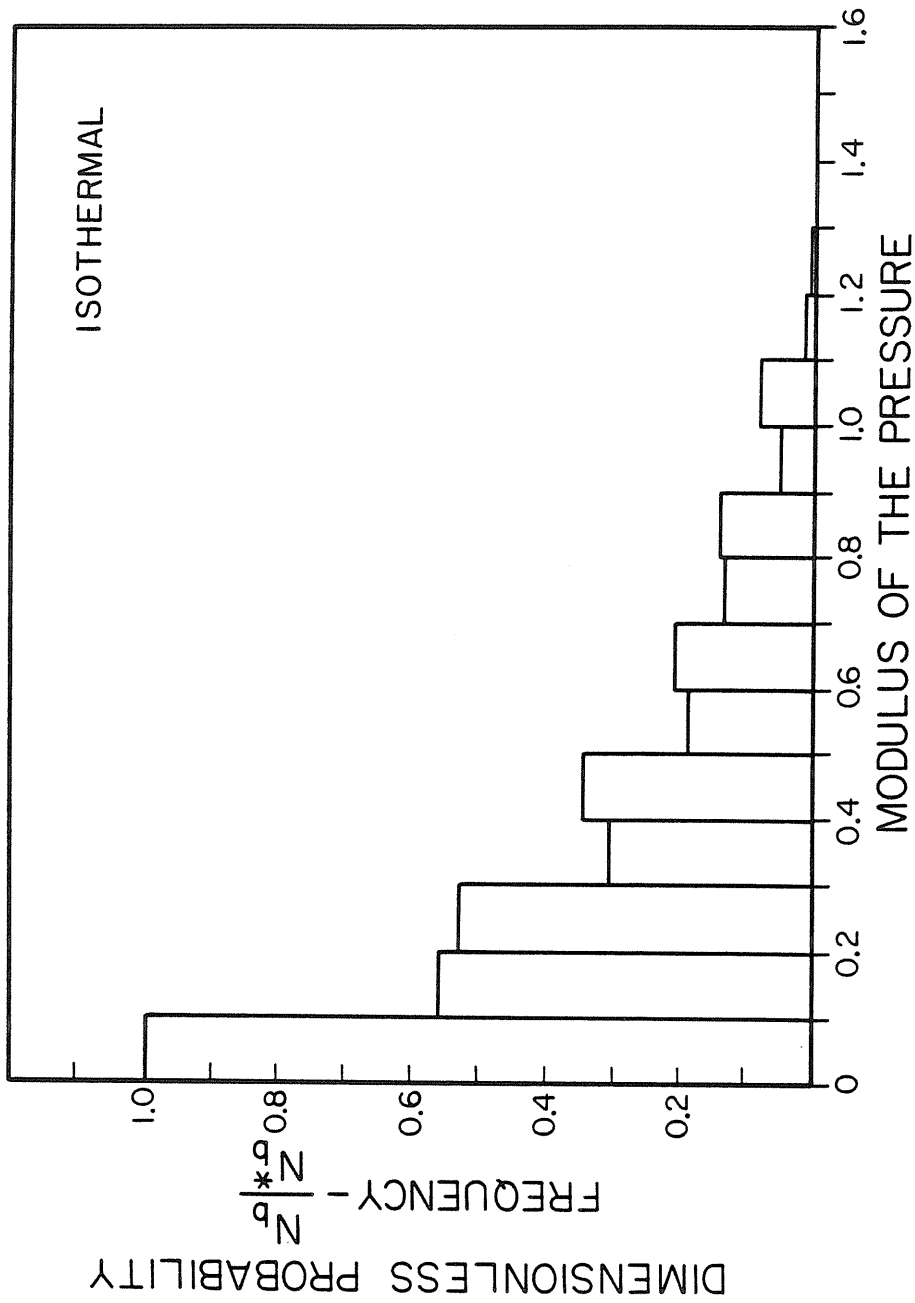

Fig. 5.48. Probability histogram showing the distribution of the modulus of pressure fluctuation intensities in a jet. (Isothermal case).

6. DISCUSSION

6.1 Introduction

The results of the present studies are quantitatively and qualitatively discussed here. Explanations for the causes of certain observed scale effects are provided through correlation of all the test results. In situations where insufficient data are available to make definite statements, probable reasons or explanations are tendered instead.

This chapter is divided into four sections. The first section deals with the results of the unseeded jets while the second focuses on the jets when flow seeding was carried out. This is followed by a comparison of results with the work of others. Finally, the chapter closes with proposals for future work.

6.2 Unseeded Jets

Results presented in Table 5.1 of Chapter 5 have shown that for a jet of constant size, the incipient cavitation index decreases with decreasing dissolved air content in the water. It has long been postulated that this suppression of the inception point is due to a reduction in the number of cavitation nuclei. However, this has never been proven or even documented quantitatively prior to the present work, insofar as studies on jets are concerned. The tabulation of the nuclei population density (Table 5.2) clearly shows that when the dissolved air content is reduced from 14.3 ppm to 4.2 ppm, the nuclei population is reduced by a factor of approximately 35, thus supporting the postu-

late. On closer inspection of the entries in Table 5.2, it can also be seen that the nuclei population density is higher in regions outside the jet (Regions 2 and 4) than those inside it. This may seem a little puzzling at first, but as mentioned earlier the jet in the present studies was created by discharging a column of water from a pressurized vessel. Hence it is to be expected that some of the gas bubbles in the jet were forced into solution by the pressurization process. Consequently the nuclei population near the jet exit (Region 1) would be lower than in the entrainment zone (Region 2). One would also expect the nuclei count to increase with downstream distance from the nozzle lip because of flow entrainment from the surrounding fluid which contains a higher nuclei population. This can be shown to be the case by comparing the nuclei population density in Region 3 to Region 1. It is worth pointing out that as the dissolved air content drops so does the difference in the nuclei population in regions inside and outside the jet.

It has also been found in the same nuclei population measurements discussed above that the population density of a fixed dissolved air content is independent of the cavitation index in the jet, at least up to the inception point. It is believed that this finding is not universally true but is a consequence of the test procedures currently practiced. Remember that the jet was discharged into a stationary tunnel sitting at an absolute pressure of approximately 13 psia and made to cavitate by rapidly lowering the pressure in the tunnel.

Since the duration of a typical run was less than 10 seconds, it is fair to assume the pressure reduction process itself would not significantly affect the nuclei population. It is our opinion that the nuclei count at a particular air content under such an operating condition is determined by the steady state condition in the water tunnel, namely, the pressure at which the water tunnel was kept prior to a test run.

The results as tabulated in Table 5.1 in Section 5.2 show that the measured incipient cavitation indices for the 3.17 mm and 4.76 mm jets at the same dissolved air content are not too different from each other. On the other hand, the 6.35 mm jet exhibits a cavitation inception number that is substantially different from the other two. The most probable explanation for this observation would be the different nuclei population in the cavitation-prone region of the jet. However, to account for the big difference in the measured σ_i's, the nuclei population in the largest jet should be significantly larger than the other two. An attempt will now be undertaken to demonstrate that this is the case.

It has already been established that at any dissolved air content, the nuclei population density is independent of the size of the jet. It follows then that at any instant the number of nuclei present in the region that is susceptible to cavitation inception is proportional to the volume of liquid in that region. As has been reported earlier, the cavitation-prone region of the two smaller jets extends from 6 to 16 jet diameters downstream of the nozzle exit while in the largest jet

it covers a distance of 2 to 14 diameters. Using these results and the data on the spread of the three jets as presented in Figures 5.38(a)-(c), it was calculated that the relevant volumes in the 6.35 mm and 4.76 mm jets were respectively 9.3 and 2.3 times more than in the smallest jet. The volume in the smallest jet was computed to be 5.41 cm^3. Therefore, for the reason stated at the outset of this paragraph, it follows that the measured σ_i's are directly proportional to the number of nuclei present.

If the nuclei population was the only determining parameter, then one would expect the measured σ_i's to be scaled up or down in the same proportion when the nuclei population is altered as a result of using water with different dissolved air content. However, it is evident from the present results that this is not the case; the effect of a change in the number of nuclei on the cavitation inception number is more pronounced on the 3.17 mm and 4.76 mm jets than for the 6.35 mm jet. Obviously this implies that at least one other scaling parameter is involved. The most likely candidate is the pressure fluctuation since it is responsible for initiating cavitation.

Typically, a whole spectrum of pressure fluctuation intensities exists in a jet (Arndt and George [10]). In the present investigation, negative peak pressure fluctuations from 0 to 120 percent of the dynamic head of the jet at exit were detected. However, this is not to say that cavitation inception would occur at the first negative pressure fluctuation a bubble sees. In reality, two conditions have to be present before inception can occur. The first condition is that

the pressure fluctuation must be intense enough to create a local pressure that is conducive to the explosive growth of the bubble. It can be shown from bubble dynamics that this local pressure P_ℓ is reached when

$$P_\ell = P_V - \frac{4S}{3R} \tag{6.1}$$

The second condition to be satisfied is that the local pressure P_ℓ given by Equation (6.1) above must persist at or even below that value for a period of time that is long in comparison to the response time of the bubble. It has already been reported that no nuclei greater than 20 μm in radius was ever detected in the jets currently investigated. Since a bubble of the size reported has a response time of about 10 microseconds, which is about two orders of magnitude shorter than the time scale of the pressure fluctuations or the traverse time across the cavitation-prone region, we would expect inception to take place once the local pressure satisfies Equation (6.1). It is also evident that the pressure fluctuations recorded in the present tests are intense enough to account for cavitation inception in all the three jets studied.

It has been found that the mean static pressure at which cavitation inception occurred was a function of numerous variables, for example, the velocity and size of the jet. This meant that different minimum magnitudes of negative peak pressure fluctuations were required to initiate cavitation in each case. However, the probability histogram

on the pressure fluctuations in Figure 5.45(a) shows that the different pressure fluctuation intensities have dissimilar probabilities of occurring. Consequently, the cumulative probability of a favorable pressure fluctuation is also different from one flow condition to another. It is possible that this variable enters as a second scaling parameter.

We define a new parameter N_p as

$$N_p = n \times P(P_f) \tag{6.2}$$

where n = total number of nuclei present in the region of the jet that is susceptible to cavitation; and $P(P_f)$ = cumulative probability of favorable negative peak pressure fluctuation intensities that would cause the explosive growth of a cavitation nucleus.

In general, nuclei of various sizes are present in the jets. These nuclei are often sorted out in different size categories to facilitate documentation of their presence. In addition to having different population densities, the nuclei in the different categories require different minimum pressure fluctuations to cause them to grow explosively. Consequently the value of N_p as defined in Equation (6.2) would vary from one size category to another. Hence, Equation (6.2) should be generalized to

$$N_p = \Sigma N_{Pk} \tag{6.3}$$

where

$$N_{Pk} = n_k \times P_k(P_f) \tag{6.4}$$

The symbols have the same meaning as the corresponding symbols without the subscript k, except that they now represent the variables for a specific nuclei size category (which is characterized by a mean radius).

It follows that if Equation (6.3) is an adequate scaling parameter for cavitation inception in jets, then σ_i would be a function of N_p only. That is to say a universal curve would be obtained when σ_i is plotted against N_p, irrespective of flow conditions. The results of the present work were used to ascertain if N_p is a useful scaling parameter.

The values of N_p corresponding to the various measured σ_i's were computed at jet velocities of 10 m/s, 20 m/s and 30 m/s. The method by which these values were obtained is shown in Appendix 2 and only the results are discussed here. However, it should be pointed out that two assumptions were made to enable these calculations to be carried out and they were:

(i) that the peak pressure fluctuation intensities scaled with the dynamic head of the jet at exit; and

(ii) that the probability distribution curve of the peak pressure fluctuations was the same for all the three jets.

These assumptions had to be made because the pressure measurements were performed at only one velocity ($\simeq$ 13 m/s) and furthermore no data were available on the largest jet for reasons already discussed in the previous chapter.

The calculated results are summarized graphically in Figures 6.1

to 6.3. It can be inferred from these plots that in the range of velocities of 10 m/s to 30 m/s, the measured σ_i's do scale with N_p, for a constant size jet. However, when the data on the three jets were plotted on the same graph, the data points, especially those for the 6.35 mm jet, do not all fall on the same curve. It is conceivable that the probability distribution curve of the peak pressure fluctuations is not universal and is a function of the jet size or some yet undefined parameter. Consequently, this would mean that the computed N_p's for the largest jet were not scaled in the right proportion. It would be premature to say that this is indeed the reason for the scatter in the data points without further investigation. Nevertheless, there is a strong indication that σ_i is a function of N_p.

We have already mentioned in Section 2.6 that in the current investigation, inception was called when 5 cavitation events or more per second were detected. It was suggested that it will be more appropriate to scale the count of events to the volume in the cavitating region of the jet. Thus in a larger jet, inception will be called at a correspondingly higher count. This means that in the present case, cavitation inception in the largest jet should only be called when about 50 cavitation events or more are measured. The question at this point is whether the measured σ_i's are significantly changed as a result of this new definition of the inception point. We claim that the values of σ_i's are not greatly affected because it has been observed that once cavitation inception occurs, the number of cavitation events increases exponentially thus implying that the mean static pres-

sures between the two inception points (and consequently σ_i) were not that different. This is especially true for jets with a high nuclei population. A statistical analysis will now be performed to verify the above claim.

It is to be expected that the probability of the occurrence of cavitation events is governed by the number of nuclei in the cavitation-prone region and the cumulative probability of favorable fluctuations, that is the parameter, N_p, as discussed earlier. Since the occurrence of these events is a Poisson process, the probability of say, m events occurring per second can be written as

$$P(m) = \frac{(N_p)^m \, e^{-N_p}}{m!} \tag{6.5}$$

and

$$P(\geq m) = 1 - \sum_{\phi=1}^{m} P(\phi) \tag{6.6}$$

where $P(\geq m)$ denotes the probability of the occurrence of m events or more per second. As a conservative estimate we will take $N_p = 500$. Therefore, from Equations (6.5) and (6.6) we have

$$P(\geq 5) = 1 - e^{-500} \left[500 + \frac{500^2}{2!} + \frac{500^3}{3!} + \frac{500^4}{4!}\right]$$

or

$$P(\geq 5) \simeq 1$$

because the product of the term in the bracket and the exponential term is very small in comparison to unity. Similarly,

$$P(\geq 50) = 1 - e^{-500}\left[500 + \frac{500^2}{2!} + \ldots + \frac{500^{49}}{49!} + \frac{500^{50}}{50!}\right]$$

$$\simeq 1$$

As demonstrated above, the occurrence per second of these cavitation events has very nearly the same probabilities thereby supporting the claim that the measured inception indices in the present investigation were not significantly affected by the technique chosen. However, it can also be deduced from the above analysis that if N_p is small in comparison to the number arbitrary assigned as the inception point, then, the difference in value of the measured σ_i by virtue of this different definition of the inception point would be significant.

Another interesting finding of the current studies is that the cavitation inception number for a particular nozzle size is independent of the jet exit Reynolds number, at least over the range of velocities investigated. A possible reason for this observation is discussed in the next paragraph.

Consider the case of a jet of an arbitrary size. As mentioned before, inception would only occur when

$$P_\ell - P_V \leq \frac{-4S}{3R}$$

or

$$P_\ell \leq P_V - \frac{4S}{3R}$$

If inception occurred at a mean pressure denoted by P_T, then the minimum negative pressure fluctuation required to initiate cavitation is given by

$$P' = (P_\ell - P_T) \tag{6.7}$$

Substituting for P_ℓ in Equation (6.7) gives

$$P' = (P_V - \frac{4S}{3R} - P_T) \tag{6.8}$$

Furthermore if $P' = K\frac{1}{2}\rho V_j^2$, where K is a constant, then Equation (6.8) can be rewritten as

$$K = \frac{(P_V - P_T)}{\frac{1}{2}\rho V_j^2} - \frac{8S}{3\rho RV_j^2}$$

or

$$\sigma_i = (K_a - \Delta\sigma_i) \tag{6.9}$$

where

$$\sigma_i = \frac{P_T - P_V}{\frac{1}{2}\rho V_j^2}$$

$$\Delta\sigma_i = \frac{8S}{3\rho RV_j^2}$$

and

$$K_a = -K = \text{constant}$$

For the purpose of discussion, Equation 6.9 was plotted over the range of nuclei sizes found in the present jets. This is shown in Figure 6.5 for an arbitrary value of K_a. In the present work, σ_i was measured in the velocity range of approximately 20 m/s to 35 m/s. It can be seen from this figure that over this range of velocities, σ_i is only a weak function of the jet exit velocity, and the maximum change in the value of $\Delta\sigma_i$ is 0.05. This change in value of $\Delta\sigma_i$ with velocity is of the same magnitude as the scatter in the measured σ_i's. It is probably because of this reason that the measured σ_i's give the appearance of being independent of Reynolds number at a constant jet size.

Since K_a is arbitrary, it is applicable to any jet. If K_a had been independent of jet size, then Figure 6.5 says that the measured σ_i's for the three jets investigated would have the same σ_i's since they were operated over the same velocity range and had similar nuclei size distribution. However, the measured σ_i's are otherwise thus suggesting that K_a could possibly be a function of jet size and maybe even some other parameters. It should be emphasized again that all the above arguments are only valid if K_a is a function of the dynamic head. This information is presently unavailable, bearing in mind that K_a is a "scaling constant" for the peak and not the rms pressure fluctuations. Further investigations are required before any definite conclusions could be drawn.

Another puzzling observation was the location of the cavities at inception. As has been pointed out in the last chapter, in the two smaller jets, the cavities were first seen in the region beyond the

potential core; whereas, in the largest jet the cavities were just as likely to occur in the shear layer wedged between the potential core and the entrainment zone. As a result of this observation, we believe that it is appropriate for the cavitation-prone region of any jet to be divided into two sections; namely, the shear layer region and the region beyond the potential core which is referred to as the transition region of the jet in some literature. Furthermore, we would theorize that the factor that determines where the cavity is first seen is the ratio of the N_p in the shear layer to that in the transition zone. It is conceivable that when the ratio is less than a certain yet undetermined value, inception would always occur in the transition zone of the jet. On the other hand, this ratio of the probable cavitation occurrence parameter, N_p, could be so large that the cavities at inception always appear in the shear layer, for all flow conditions. Between these two extremes, there is probably an intermediate range where cavities could appear in either or both regions in the jet. Unfortunately a quantitative analysis similar to that performed earlier could not be carried out here due to a lack of information on the pressure fluctuation intensities in the shear layers of the present jets. However, if we were to use the size of the jet as a rough guide-line, the present results would suggest that for jets smaller than 4.76 mm, the cavities would almost always occur in the transition zone. In jets larger than 4.76 mm, the cavities are just as likely to appear in the shear layer. The upper bound of this intermediate range is probably defined by a jet of 25.4 mm size where it has been

reported by Arndt [12] for example that the cavities were seen in the shear layer. Again there is a need for further work in this area before the actual cause of this phenomenon is established.

The results of the present studies as well as those of others have shown that at a high dissolved air content, inception in the jet occurred at a relatively high mean pressure in the jet. In such a situation, only a few locations in the jet experienced local pressure fluctuations that were intense enough to cause cavitation. Consequently, the cavities at inception only occurred in these few positions. However, at a low air content, the mean pressure at inception was considerably lower which resulted in many locations having local pressures that were conducive to the explosive growth of the nuclei. Thus, the cavities were much more extensive than the former case. These explanations are consistent with the results of our flow visualization.

Up to now, we have only presented a discussion on cavitation inception in the jets where the cavitation nuclei are not generated by any external sources but are from the dissolved air content in the water. A discussion on the behavior on the same jets when flow seeding was performed will now be considered.

6.3 Seeded Jets

It is currently unknown if the pressure field in the jet was affected by the introduction of electrolysis bubbles, especially in cases when the bubbles were present in large numbers. However, for the sake of this discussion, it will be assumed that the pressure field

remains the same as in the unseeded jet. Thus it is presumed that the only effect of the seeding was to alter the nuclei population.

We have already pointed out that when flow seeding was performed, the nuclei were so abundant that the counting of these nuclei from the holograms was impractical. Nevertheless it is still desirable to have some estimate on these nuclei populations. From Kuiper's work [75], the volume of hydrogen gas produced per unit length by an electrolysis current at a water temperature of 23^{o} C is given by

$$G = 1.27 \times 10^{-4} \frac{I}{\ell_{\omega} P_g} \, m^3/s \tag{6.10}$$

where I = current through the wire in amperes

ℓ_{ω} = the length of the wire in meters, and

P_g = the gas pressure in N/m^2.

The gas pressure P_g can be found from the static equilibrium equation, viz

$$P_g = (P - P_V + \frac{2S}{R})$$

where P is the static pressure at the position of the wire. It is surprising to note from Equation (6.10) that the volume of gas production is independent of the diameter of the electrode. To obtain an order of magnitude estimate on the nuclei population, we shall further assume that all the nuclei are of the same size and are 10 μm in diameter. Hence, if $\dot{n}_g$ denotes the number of bubbles produced per unit time by the current I, then,

$$\dot{n}_g \frac{4}{3}\pi R_g^3 = G \tag{6.11}$$

Substituting for G in Equation (6.11) and rearranging we have

$$\dot{n}_g = 2.43\times10^{11} \frac{I}{\ell_\omega P_g} \tag{6.12a}$$

But as mentioned in previous chapters, ℓ_ω = 0.5 mm. As can be inferred from Equation (6.12a), the number of bubbles generated is dependent on the gas pressure which in turn is determined by the velocity of the jet. However, for convenience, $\dot{n}_g$ was computed at only one representative velocity of 40 ft/s (13 m/s). This corresponded to a gas pressure of approximately 20 psia (1.35 atm.). Thus Equation (6.12a) becomes

$$\dot{n}_g = 3.52\times10^{9}\ I \tag{6.12b}$$

Hence it follows that the total number of nuclei that are present in the cavitation-prone region at any instant is given by

$$n = n_d + \frac{Q}{\dot{Q}_j}\dot{n}_g$$

where n_d = number of nuclei normally present in the jet without flow seeding

Q = volume of the cavitation-prone region

and $\dot{Q}_j$ = volume efflux of the nozzle per second.

Proceeding in a similar manner as has already been discussed for the unseeded jets, the measured incipient cavitation indices at various magnitudes of the electrolysis current were plotted against the para-

meter N_p for all the three jets concerned. This is shown graphically in Figure (6.6). Again, it can be seen that while the data for the two smaller jets lie on the same curve, those for the largest jet do not. The probable explanation for this discrepancy has already been discussed in the previous section.

It can be easily shown that when flow seeding was performed, the number of bubbles introduced into the flow were far more numerous than those that are normally present in the jet. Consequently one would not expect the dissolved air content of the water to have any significant effect on the cavitation inception number under these circumstances. This was the general observed behavior of the jets under investigation as was seen from Figures 5.20 to 5.43. There were some exceptions where the dissolved air content had an observable effect on the measured σ_i's although no regular pattern could be inferred. The reason for this discrepancy in the data is not known at present. Another observation of the present results is that σ_i do not scale with the jet exit Reynolds although in some instances the data of the jets do supplement one another.

With flow seeding, the jet cavitated a lot sooner and as a result the tests had to be confined over a lower range of velocity which was 10 m/s to 20 m/s. Looking back at Figure (6.5) it can be seen that over this range of velocity, there is a strong dependence of σ_i on the jet velocity (or Reynolds number at a constant jet size). Therefore we would expect this dependence to show up despite the

scatter of the data points, which is the case as can be seen in Figures 5.8(a) to 5.10(d). It should be stressed at this point that the above explanation is valid only if the assumptions made for the plot of Figure 6.6 are true. The experimental results also showed that for a constant jet size and at a fixed velocity, σ_i increases with increasing electrolysis current. The reason for this behavior can be explained as follows. When the flow was seeded with more and more nuclei, there was an increasing tendency for cavitation inception to be caused by higher and higher fluctuation intensities although the frequency of occurrence of these intensities were less than the lower ones. Consequently increasing values of σ_i were recorded. In addition, a "saturation" point was reached when the nuclei were so numerous that inception in the jet occurred at the very first opportunity. Beyond this point, the measured σ_i did not exhibit any significant change in value with further increase in the number of electrolysis bubbles.

We have, up to this moment, only discussed the results of the present investigations with little to no references made to the work of others. Our attention will now be turned to this area.

6.4 Comparison of Experimental Results

6.4.1 Nuclei Measurements

It has already been stated earlier that so far measurements of the distribution of the nuclei population in submerged jets have not been available. However, numberous investigators, for example, Gates and Acosta[46], Peterson et al [96] and Keller and Weitendorf [68] have

made nuclei measurements in water tunnels under various flow conditions. It can be seen by comparing Figure 6.7 and Figure 6.8 that the results of the current work compare favorably with those of the others except that large size nuclei were not found in our jets. This is because the present measurements were made in a jet discharging into an otherwise stationary medium; whereas, the other measurements were performed in flowing water tunnels which were at times under cavitating conditions.

In the preliminary work by Ooi and Katz [88], it was reported that the size and distribution of the nuclei population were dependent on the cavitation number which is contrary to the present observation. Since the measurements were made on the same test facility, we believe that this discrepancy in the results is due to the different test procedures. Recall that in the current investigation, the pressure in the tunnel was always raised to its initial value and the tunnel was permitted to sit at that pressure for some time before the next test run was made. This procedure was not adopted in the earlier reported work. It is thus obvious that there is a need for all investigators to monitor the nuclei population distribution in their jets especially if different test procedures are followed.

6.4.2 Photographic Investigation of the Non-Cavitating Jets - Coherent Structures

The existence of large quasi two-dimensional coherent structures in shear flows was first reported by Brown and Roshko [24]. Since

then, numerous other investigators, for example, Winant and Browand[112], Konrad[73], Davies and Yule[29] and Perry and Watmuff[94] have directly or indirectly established the presence of these structures in shear layers, wakes and jets. However, Chandrsuda et al [27] and Castro and Bradshaw [26] suggested that these large scale eddies were neither quasi-deterministic nor two dimensional. Both groups of investigators claimed that the observed features of Brown and Roshko were "the notoriously prolonged effects of transition" of initially laminar layers. Chandrsuda et al further suggested that the flow would become highly three-dimensional whenever the free stream turbulence was high. However, these claims have been disproved by Wygnanski et al [113] who concluded that "the two-dimensional character of the coherent eddies perseveres in spite of strong external small-scale buffeting, and the Brown-Roshko structure may be more common in practice than was hitherto observed".

In the present study, these large structures could only be observed up to a relatively low Reynolds number (based on axial position) of approximately 45,000. An example of these structures is shown in Figure 6.9. Unlike the structures in the plane shear layer described by Brown and Roshko, the present large scale structures only remained distinct up to the second or third vortex. Beyond that the flow became three-dimensional with a multitude of small grainy structures.

As was pointed out in the last chapter, cellular structures were seen just downstream of the laminar region of the jet. These struc-

tures were also seen by Konrad [73]. It is believed that these cellular structures begin as hairpin vortices and as they proceed further downstream, they become unstable and produce the three-dimensional small scale structures in the jet.

The work of Brown and Roshko has established that the longitudinal increase in the scales of the large eddy structures and consequently the spreading rate of the shear layer was accomplished by the coalescence of two or more of the neighboring coherent structures. Based on their schlieren photographs, Brown and Roshko estimated that the slope of the spread of the shear layer was 0.38. In the present work, slopes of 0.33, 0.24 and 0.43 were obtained for the 3.17 mm, 4.76 mm, and 6.35 mm jets, respectively. The reason for the different spread rates is presently unclear. It has been suggested that the initial condition of the jet could be a determining factor.

6.4.3 Pressure Fluctuation Measurements

All previous pressure fluctuation measurements were made in an Eulerian frame with intrusive pressure transducers. Although such measurements do give information concerning the pressure field in the jet, they are not directly applicable to the problem of cavitation which is a Lagrangian problem (i.e., the fluctuations moving with the fluid). It is our belief that the bubble injection technique used in the present work and described in detail in Chapter 4 represent the first attempt ever in measuring the pressure fluctuations in a Lagrangian frame. The present method has the added advantage

that the "probes" do not cause a significant flow disturbance since they are a part of the flow. Also this method provides a means where the instantaneous pressures at numerous positions in the jet could be simultaneously measured, which is not possible with the conventional method by virtue of the fact that the flow would be drastically changed by the inserted pressure transducers.

It has already been pointed out in the course of this chapter that cavitation is initiated when the local pressure dips to or below the vapor pressure. Thus a knowledge of the peak temporal pressure fluctuations would be very useful. However, with the exception of the present investigation, such information has been sorely lacking. All the measurements have dealt with the rms of the pressure fluctuations although Arndt and Ippen [6] and Rouse [103] for example have noted that peak fluctuations could be as high as 7 times the rms level in a turbulent boundary layer and 10 times in a jet. In the present investigation, the maximum peak fluctuation intensities are only about 2 to 3 times that of the computed rms values. Various possible reasons for this discrepancy come to mind. The fact that the present measurements were made in water whereas all the other measurements were in air may account for some of this difference. It has been discussed in earlier sections that the intensity of the pressure fluctuations could very well be a function of the jet size and velocity. Both these factors could be additional reasons for the discrepancy in the results. In any event, the peak pressure fluctuation intensities in the present jets are high enough to initiate cavitation

inception if a nucleus is present at the right instant.

To have an idea on the rms fluctuation, the jet was divided into various regions as shown in Table 6.1. The calculation was then performed using the expression:

$$\left\langle \frac{P'}{\frac{1}{2}\rho V_j^2} \right\rangle \cdot \left[\frac{1}{(m-1)} \sum_{i=1}^{m} \left(\frac{P_i'}{\frac{1}{2}\rho V_j^2} \right)^2 \right]^{\frac{1}{2}}$$

where $\left\langle \frac{P'}{\frac{1}{2}\rho V_j^2} \right\rangle$ = rms of the dimensionless pressure fluctuation in a particular region of the jet.

m = total number of data points in the same region of the jet.

P' = instantaneous pressure fluctuation.

The computed results are tabulated in Tables 6.1 and 6.2 for the polytropic and isothermal cases, respectively. It can be seen from these tables that there are two entries in each region of the jet. The first entry is the calculated rms fluctuation when all the measured data were used. The second entry corresponds to the calculated rms value when a few of the data points were not included in the calculation because they exhibited values that were significantly different from the majority of the data in that group. A quick comparison of these two entries clearly show that in many instances, there is a sizeable difference in the two rms values. This implies that the calculated values are not too accurate because of the limited number of data points. It should also be pointed out that the numbers in

	$0 \leq r/D \leq 0.5$	$0.5 \leq r/D \leq 1.0$	$1.0 \leq r/D \leq 1.5$	$1.5 \leq r/D \leq 2.0$	$2.0 \leq r/D \leq 2.5$	$2.5 \leq r/D \leq 3.0$
	0.25(95)	0.43(38)	0.64(13)			
$4.0 \leq X/D \leq 6.0$				-	-	-
	0.20(92)	0.32(35)	0.45(11)			
	0.39(43)	0.56(45)	0.76(25)	0.48(3)		
$6.0 \leq X/D \leq 8.0$				-	-	-
	0.31(41)	0.39(42)	0.65(22)			
	0.56(24)	0.53(35)	0.56(33)	0.63(14)		
$8.0 \leq X/D \leq 10.0$					-	-
	0.40(20)	0.40(32)	0.43(30)	0.56(13)		
	0.66(13)	0.69(38)	0.73(31)	0.83(20)	0.94(3)	
$10.0 \leq X/D \leq 12.0$						-
	0.40(11)	0.54(35)	0.61(28)	0.68(17)	0.77(2)	
	0.64(12)	0.65(28)	0.78(18)	0.59(14)	0.69(1)	0.65(7)
$12.0 \leq X/D \leq 14.0$						
	-	0.51(24)	0.49(14)	-	0.58(10)	-
	0.60(6)	0.69(10)	0.64(25)	0.68(25)	0.65(9)	0.76(13)
$14.0 \leq X/D \leq 16.0$						
	0.43(5)	-	0.50(22)	-	0.56(8)	0.57(10)

Table 6.1 A tabulation of the rms pressure fluctuations in various regions of the present jet. (polytropic index = 4/3)

	0≤r/D≤0.5	0.5≤r/D≤1.0	1.0≤r/D≤1.5	1.5≤r/D≤2.0	2.0≤r/D≤2.5	2.5≤r/D≤3.0
	0.19(95)	0.33(38)	0.49(13)			
4.0≤X/D≤6.0				-	-	-
	0.16(92)	0.26(35)	0.36(11)			
	0.31(43)	0.40(45)	0.60(25)	0.38(3)		
6.0≤X/D≤8.0					-	-
	0.25(41)	0.34(42)	0.51(22)	-		
	0.44(24)	0.41(35)	0.44(33)	0.46(14)		
8.0≤X/D≤10.0					-	-
	0.32(20)	0.32(32)	0.37(30)	0.42(13)		
	0.47(13)	0.51(38)	0.53(31)	0.61(20)	0.65(3)	
10.0≤X/D≤12.0						-
	0.32(11)	0.42(35)	0.43(28)	0.50(17)	0.44(2)	
	0.47(12)	0.48(28)	0.59(18)	0.44(14)	0.46(11)	0.49(7)
12.0≤X/D≤14.0						
	-	0.37(24)	0.39(14)	-	0.41(10)	-
	0.48(6)	0.50(10)	0.54(25)	0.45(25)	0.55(9)	0.57(13)
14.0≤X/D≤16.0						
	0.33(5)	-	0.40(22)	-	0.49(8)	0.43(10)

Table 6.2 A tabulation of the rms pressure fluctuations in various regions of the present jet. (isothermal case)

parentheses in the two tables represent the sampling size.

In the rms pressure fluctuation measurements made to date, the results show that the magnitude of fluctuations decreases with increasing distance from the jet exit. However, this trend is not apparent in the present work. The reason for this discrepancy is not known at present. In addition the current rms level is considerably higher than those reported by Sami et al [105] and Barefoot [16]. Their lower rms measurements could be due to the effect of spatial averaging since the transducers they used were large by comparison. Needless to say, further work has to be undertaken before some of these differences in experimental findings can be explained.

6.4.4 Cavitation Results

A careful survey on the published work in jet cavitation revealed that this area is currently in a very disorganized state. Despite the fact that measurements were usually performed using different experimental procedures under various flow configurations, many investigators have not carefully taken into account the flow environment and the flow dynamics associated with the jets they were working on. For example, only a handful of workers have carried out flow visualization studies and pressure fluctuation measurements in jets. Nuclei population density measurements have also been seriously lacking. As a result of this oversight, it is often difficult if not impossible to compare the results of the various investigators especially since σ_i's were usually measured in different sized nozzles and at various

dissolved air content. Nevertheless we shall present a very brief discussion on the comparison of the present results with the work of others below. This discussion will be limited to jet cavitation only since other shear flow results can be found in Arndt and George [10] and Arndt [12].

The incipient cavitation number for a 3.17 mm and a 6.35 mm jet was reported to be 0.25 and 0.55, respectively, by Lienhard and Stephenson [78]. Although they did not measure the air content in their jet, we believe the jet could be at most near saturation. This means that their σ_i's are considerably higher than the presently measured values of 0.16 and 0.27 for the unseeded jet at 14 ppm. The higher values of σ_i's could be due to the following reasons.

It has been shown from schlieren photographs that the present jets are laminar at exit. On the other hand it is likely that the jets of Lienhard and Stephenson were turbulent. If this is true then the higher σ_i could be attributed to the higher nuclei population in the cavitation-prone region of the jet since Hussain and Zedan [61] have demonstrated that the spread rate of an initially turbulent jet is greater than a laminar one. The difference in the results could also be caused by the different intensity of pressure fluctuations since it is conceivable that they are governed by the initial conditions of the jet.

Another disagreement in the results is the location of the cavities of inception in the jet. It has either been stated or implied in a number of sources (e.g., Arndt [12] and Arndt and George [10])

that the cavities at inception are first seen in shear layer of the jet, which is not always the case in the present jets. The probable explanations for this discrepancy have already been discussed earlier and will not be repeated here. However, we would like to comment on Sami et al's [105] assumption that the cavities usually occur at the cores of the turbulent eddies. Our extensive flow visualization studies in the present jets have not given such an indication. Of the hundreds of schlieren photographs that were taken at inception, only one showed the occurrence of a cavity in the core of a vortex. This is shown in Figure 6.10. Finally, it should be also pointed out that contrary to the findings of Baker et al [14], the measured cavitation index of the present jet was a function of the dissolved air content even when the jet was undersaturated. The reason for this discrepancy is still not known.

6.5 Proposals for Future Work

One of the assumptions made in the course of the current discussion is that the probability distribution curve of the peak pressure fluctuation intensities is universal. Questions were raised as to the validity of this assumption since the distribution curve could very well be a function of the jet size, the jet velocity and the exit condition. All of these questions could be answered by performing a series of pressure measurements on jets of different sizes over a range of velocities and turbulence level at exit. Recall also that the present pressure measurements were confined

to the transition region of the jet. Obviously these measurements could not be accurately used to predict cavitation occurrences in the shear layer since the distribution curve could be different. Consequently, it would be advantageous to extend these measurements to this region of the jet.

It was also postulated that the factor that determines where the cavity is first seen at cavitation inception is the ratio of the N_p in the shear layer to that in the transition zone of the jet. This could be established one way or another by using the results of the above proposed studies.

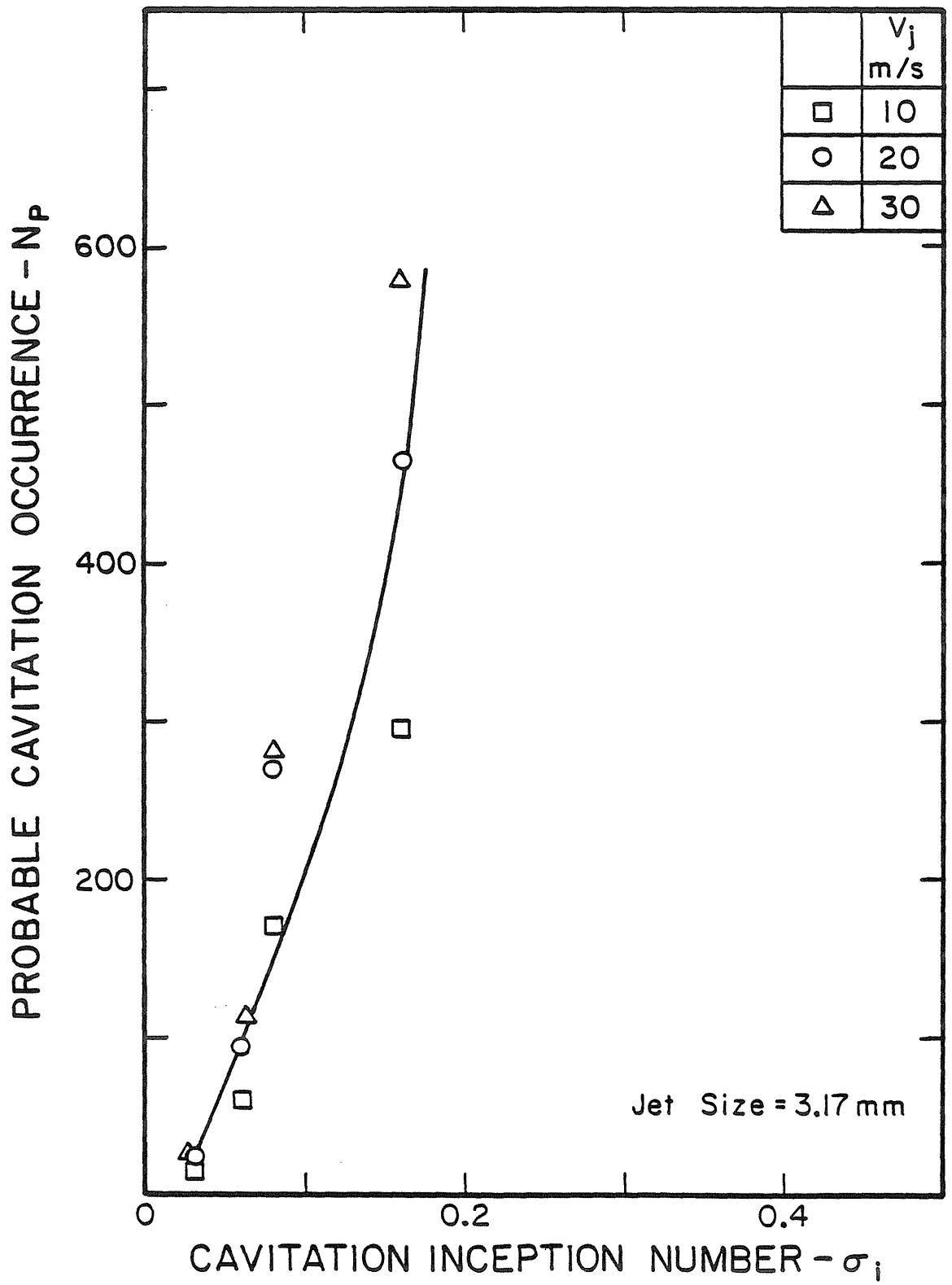

Fig. 6.1. A plot of the probable cavitation occurrence parameter, N_p, versus σ_i at different jet exit velocities for the 3.17mm jet.

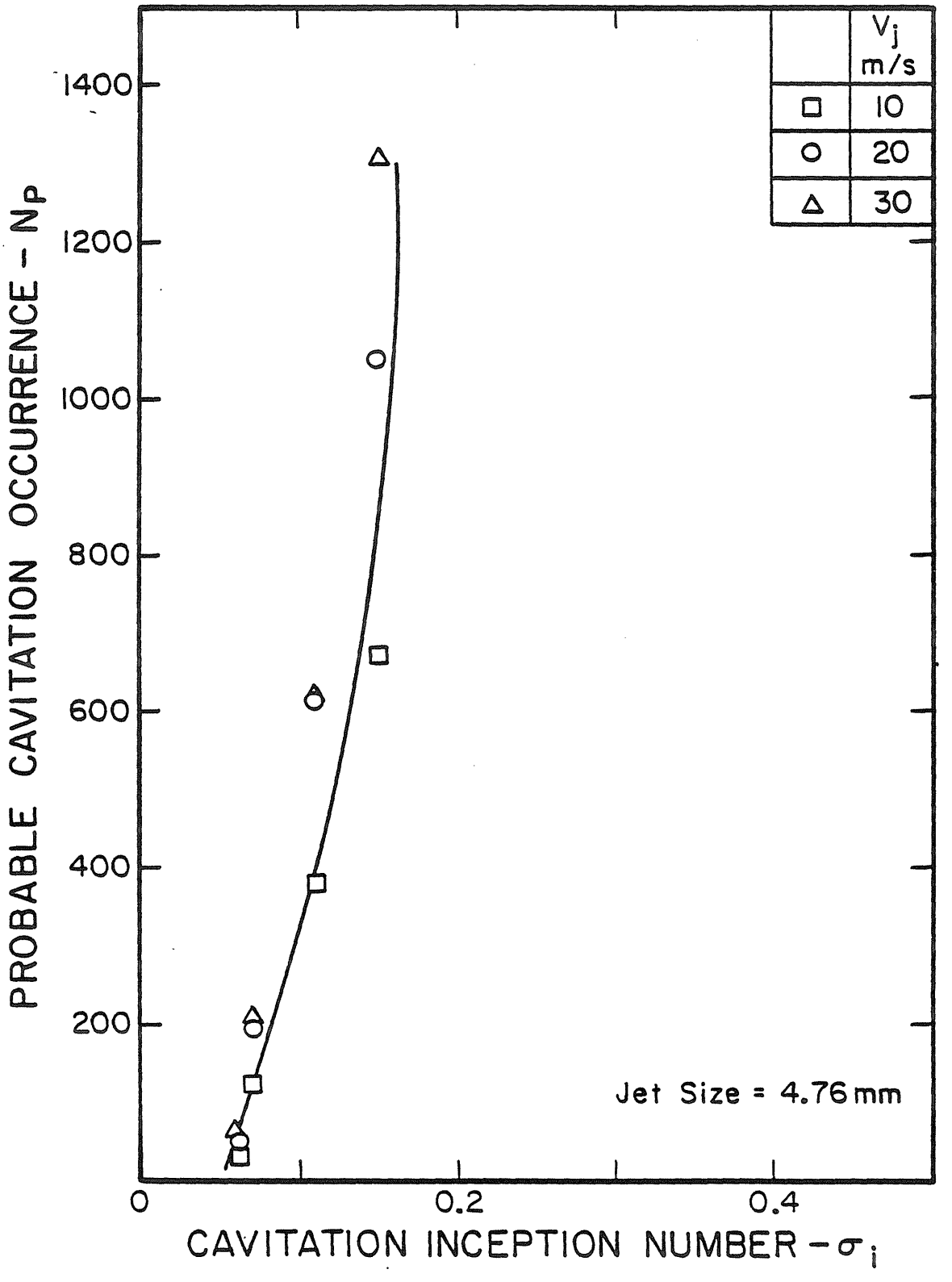

Fig. 6.2. A plot of the probable cavitation occurrence parameter, N_P, versus σ_i at different jet exit velocities for the 4.76mm jet.

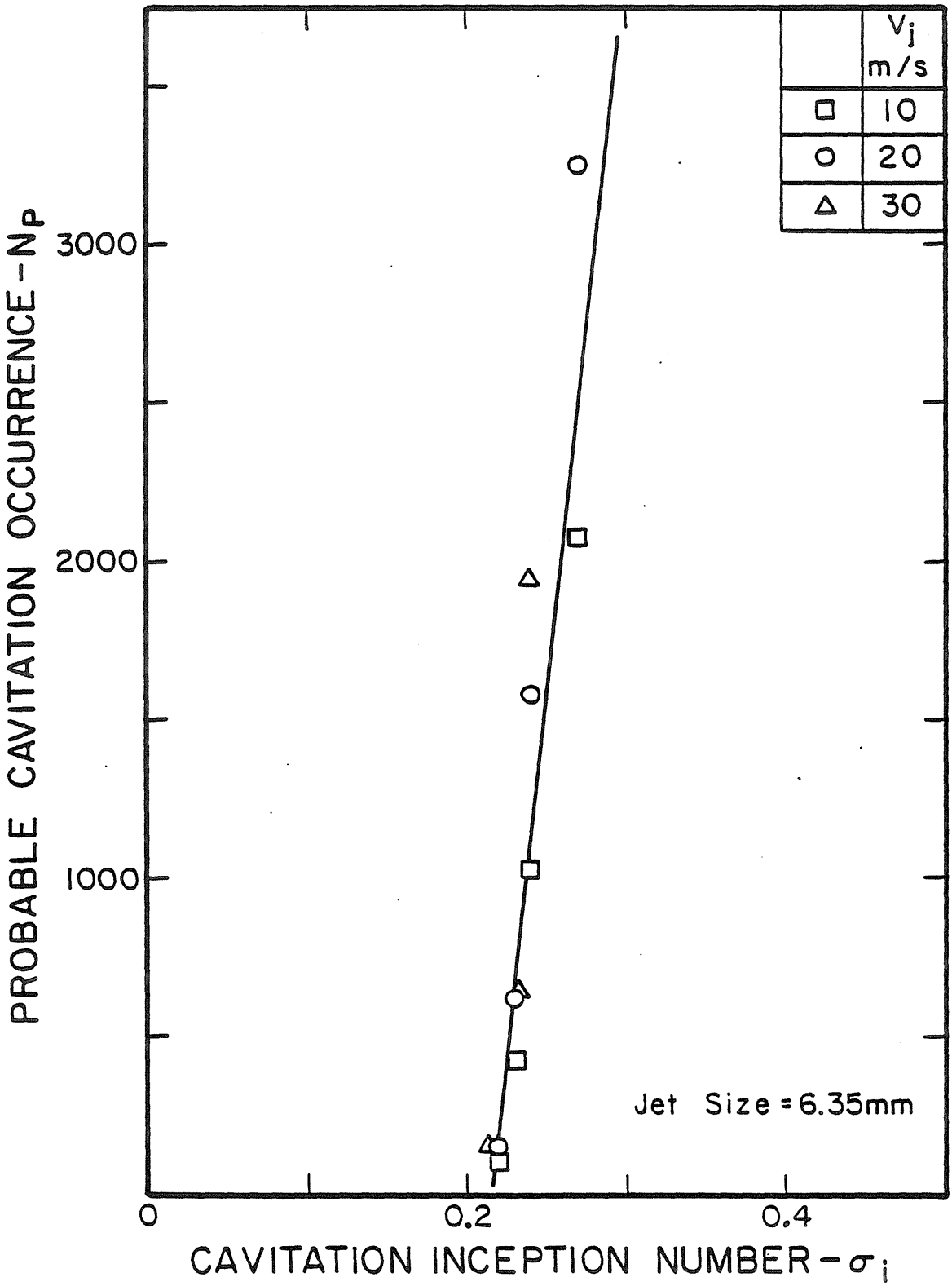

Fig. 6.3. A plot of the probable cavitation occurrence parameter, N_p, versus σ_i at different jet exit velocities for the 6.35mm jet.

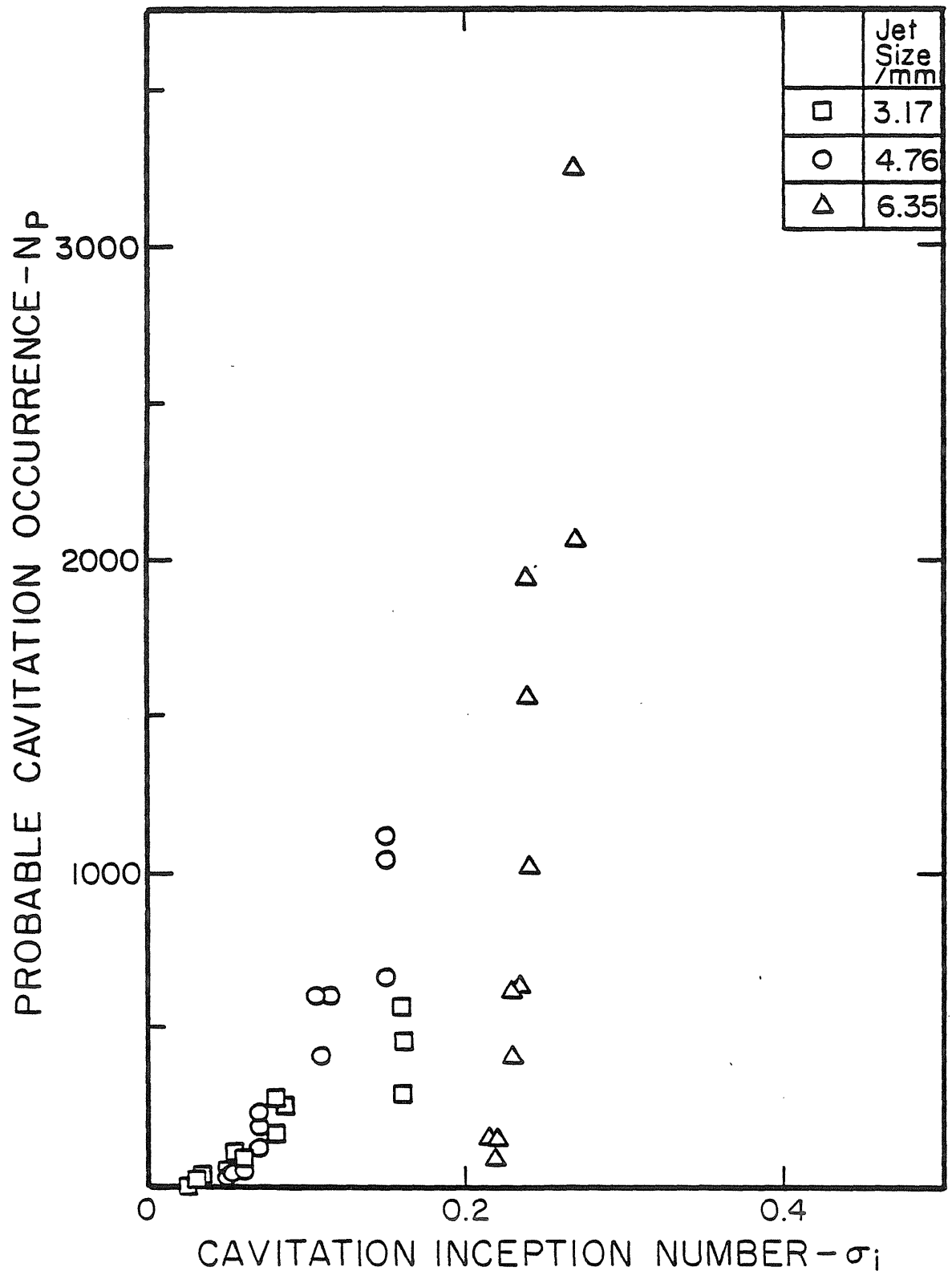

Fig. 6.4. A plot of N_p versus σ_i for the 3.17mm, 4.76mm and 6.35mm jet at different jet exit velocities.

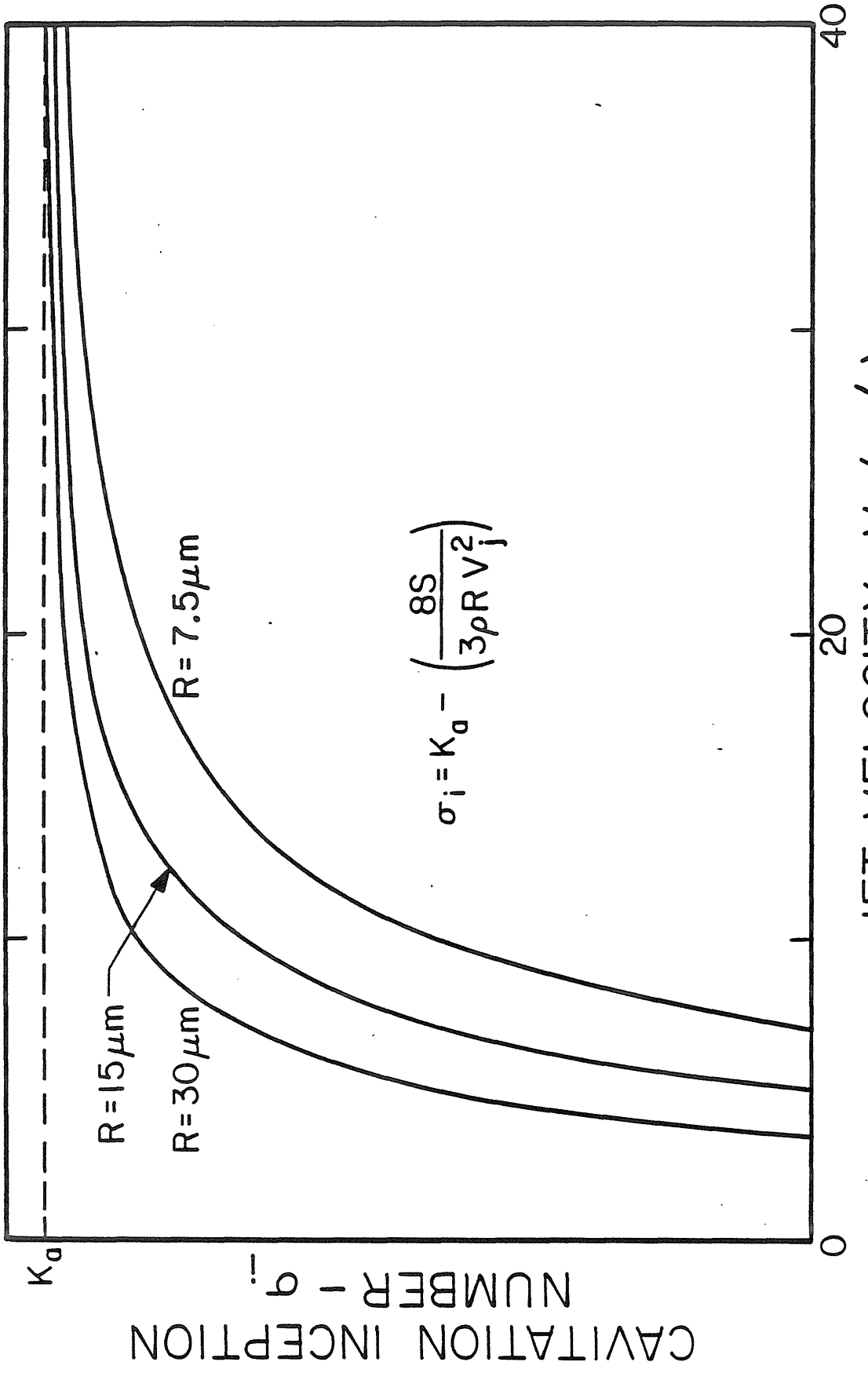

Fig. 6.5. A plot of σ_i versus V_j for the equation $\sigma_i = K_a - (8S/3\rho RV_j^2)$.

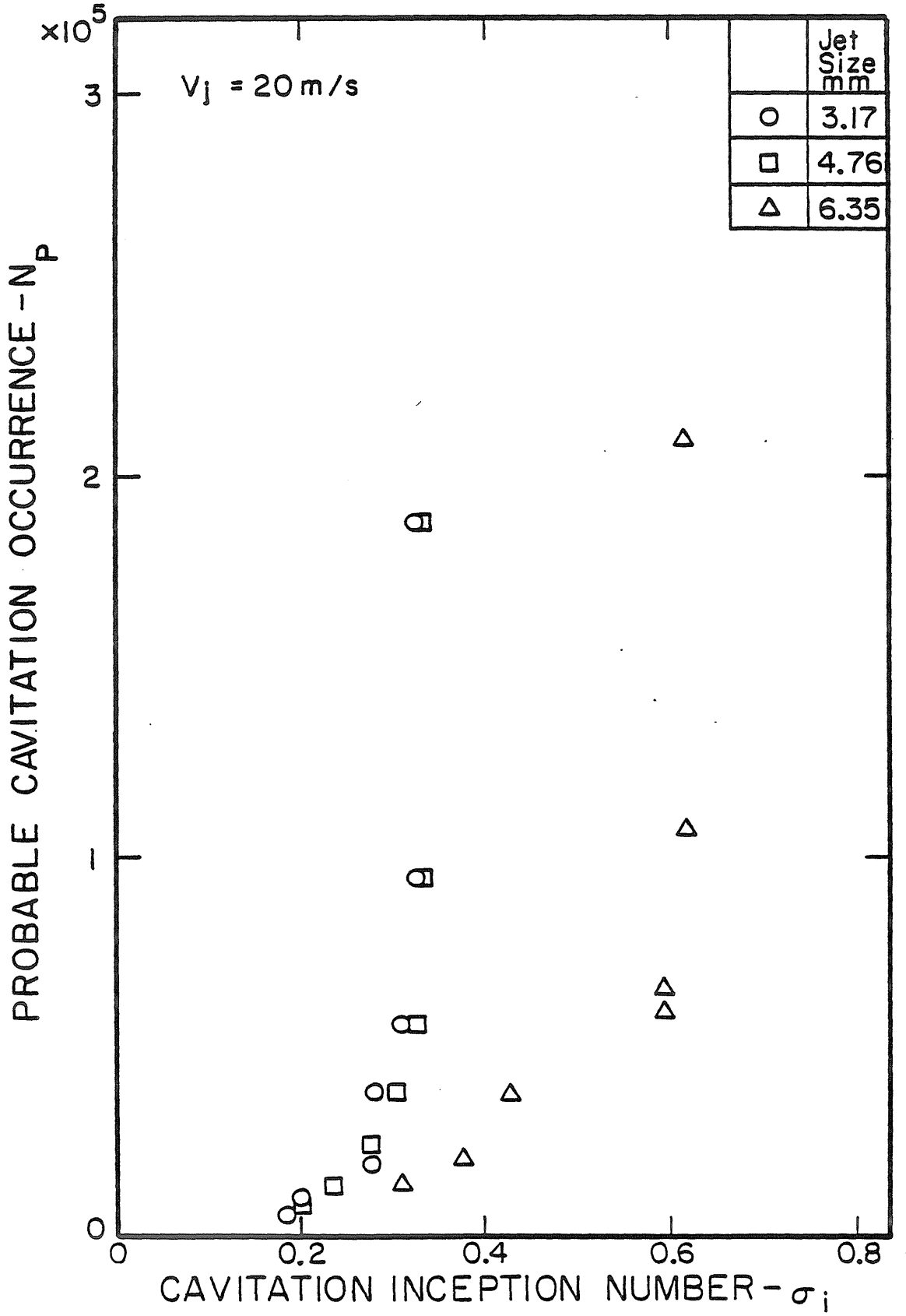

Fig. 6.6. A plot of the probable cavitation occurrence parameter, N_p, versus σ_i at a jet exit velocity of 20m/s for the three jets when flow seeding was carried out.

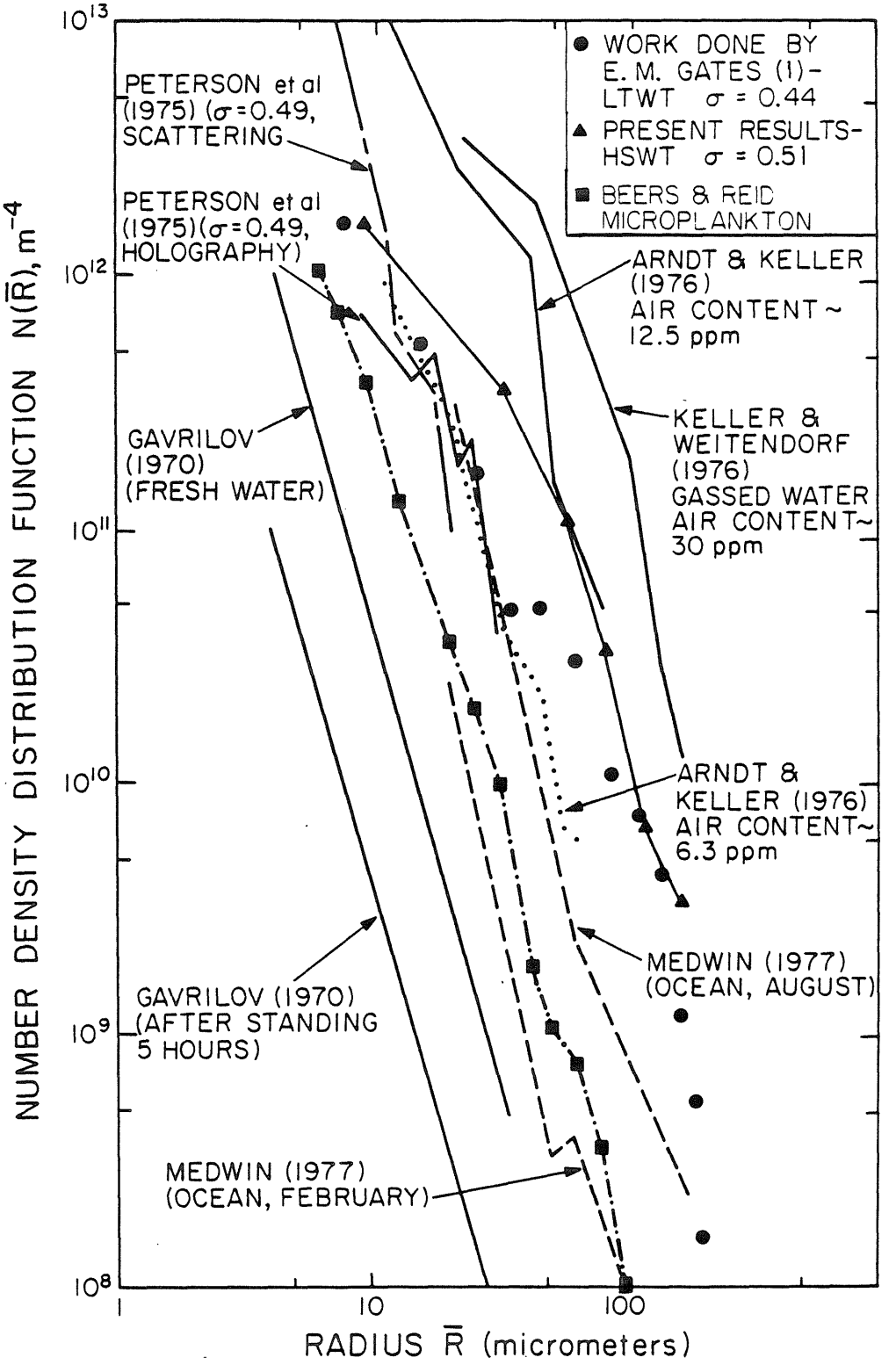

Fig. 6.7. A plot showing the nuclei distribution from various sources [Katz and Acosta (1981)].

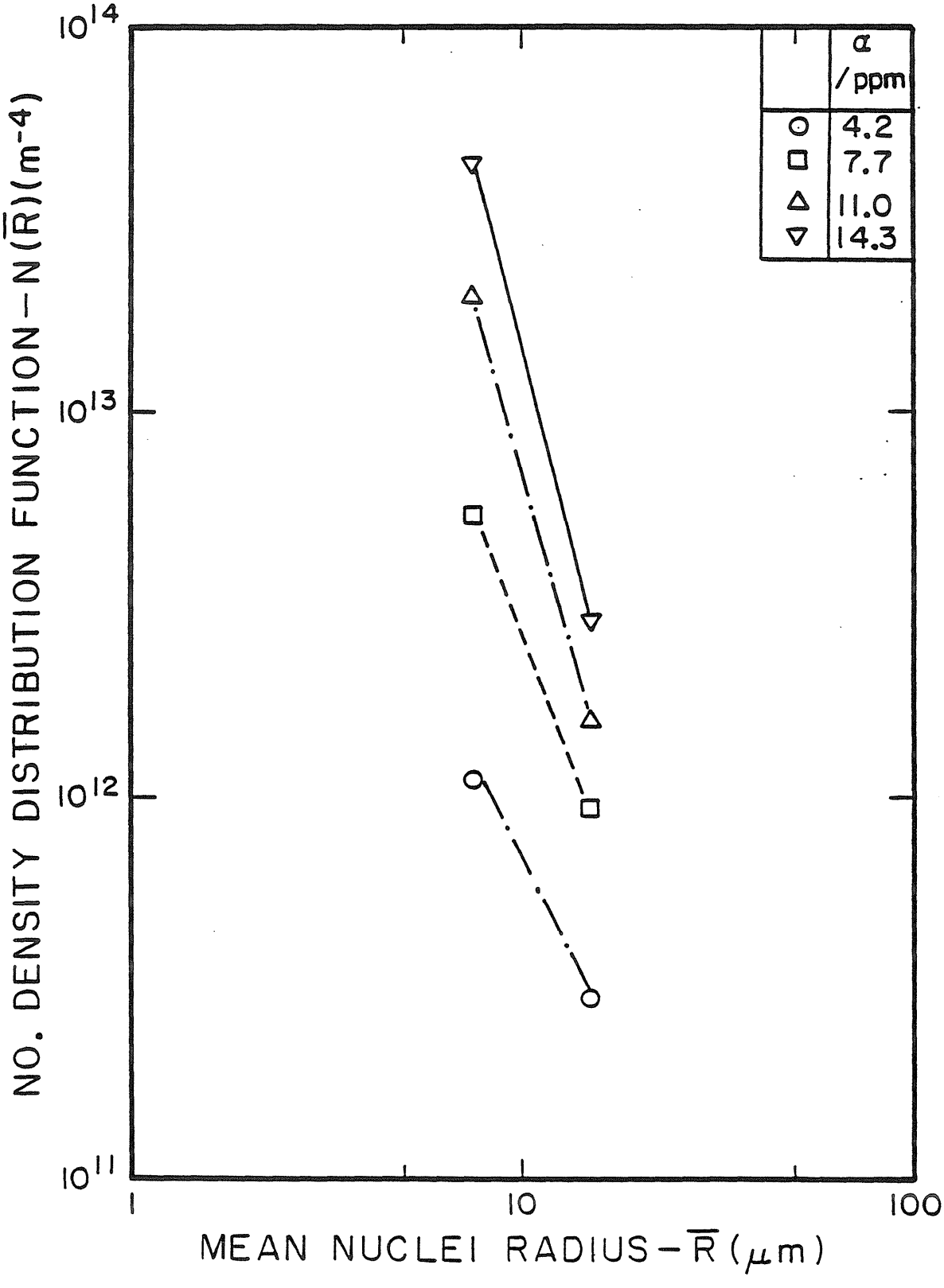

Fig. 6.8. A plot showing the nuclei distribution in the present jets at different dissolved air contents.

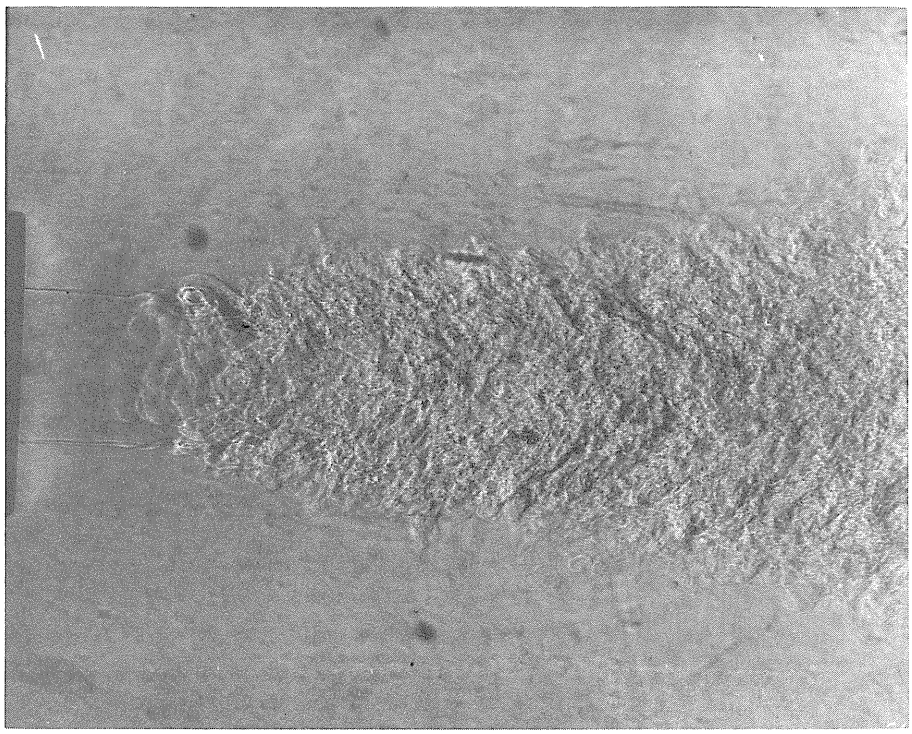

Fig. 6.9. Schlieren photograph showing the large eddies in the 6.35mm jet at $Re_D = 3.1 \times 10^4$.

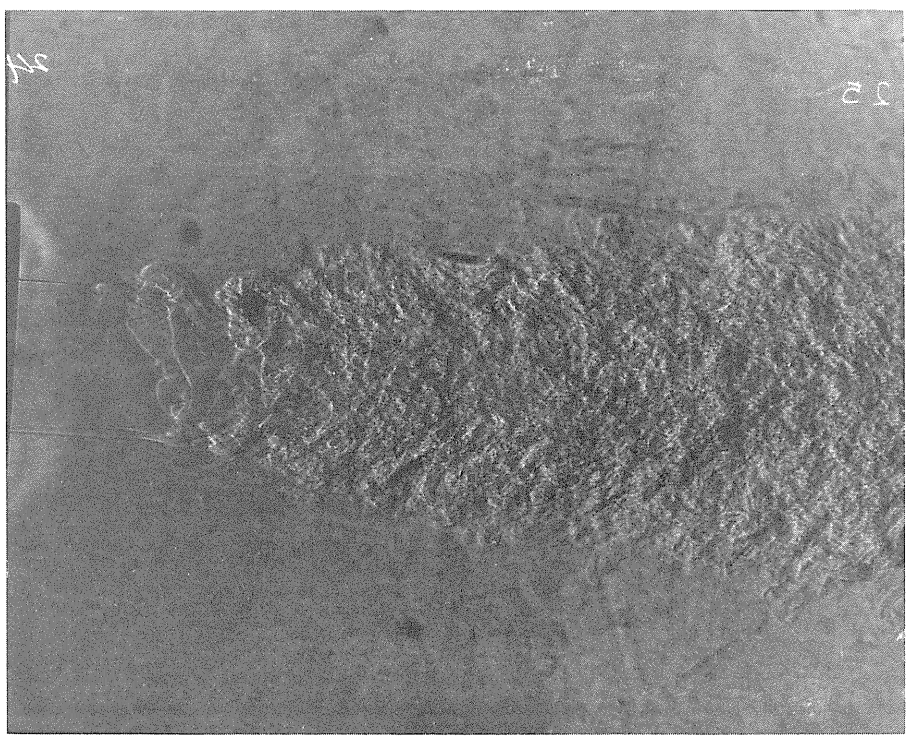

Fig. 6.10. Schlieren photograph showing cavitation inception in the core of a vortex.

7. SUMMARY AND CONCLUSIONS

A new technique employing specially tailored air bubbles has been successfully used to map out the temporal pressure field in the jet. The results showed that negative peak fluctuation of as low as 120 percent, and positive peak of as high as 160 percent of the dynamic head existed in the jet. The fluctuation intensities were found to have a slightly skewed bell shape distribution.

Flow visualization revealed that cavitation inception occurred with a sudden burst of cavities within the jet. The location of these cavities were dependent on the jet size but were never observed beyond 16 jet diameters downstream of the nozzle lip. In general, these cavities did not start in the cores of the vortices.

The cavitation inception numbers in all the jets were found to be independent of the velocity when the jets were not seeded. The dissolved air content had a definite influence on the inception number. With flow seeding, the inception number exhibited, in most cases, a linear dependence on the exit velocity. This dependency on velocity was found to increase with increased nuclei population. The present results also indicated that for a fixed jet size, σ_i is a function of a newly defined parameter, N_p, called the probable cavitation occurrence parameter. However, we were unable to determine if this scaling parameter is universal from the present experiments.

A survey of published literature showed that few investigators have actually tried to correlate their cavitation results to the pres-

sure field in the jet. In addition, many of these workers have neglected to make careful flow visualization studies or to document the nuclei population in their jets. It is our belief that until and unless such studies are undertaken, the many questions that exist will never be satisfactorily answered.

REFERENCES

1. Acosta, A. J., and Hamoguchi, H., Cavitation Inception on the ITTC Standard Headform", Hydrodynamics Laboratory, Rep. No. E-149.1, California Institute of Technology, Mar., 1967.

2. Acosta, A. J., and Parkin, B. R., "Cavitation Inception - A Selective Review", J. Ship Res., 19,4; pp. 193-205, 1975.

3. Acosta, A. J., "Cavitation Inception and Internal Flows with Cavitation", the 4th David W. Taylor Lecture, Oct., 1979.

4. Arakeri, V. H., "Viscous Effects in Inception and Development of Cavitation on Axisymmetric Bodies", Ph. D. dissertation, California Institute of Technology, 1973.

5. Arakeri, V. H., and Acosta, A. J., "Viscous Effects in the Inception of Cavitation on Axisymmetric Bodies", J. Fluids Engrg., Vol. 95, Series 1, No. 4, pp. 519-527, Dec. 1973.

6. Arndt, R. E. A., and Ippen, A. T., "Rough Surface Effects on Cavitation Inception", J. Basic Engrg., Vol. 90, Series D, No. 2, pp. 249-261, June 1968.

7. Arndt, R. E. A., and Daily, J. W., "Cavitation in Turbulent Boundary Layers", Cavitation State of Knowledge, pp. 64-86, ASME, 1969.

8. Arndt, R. E. A., Billet, M. L., Holl, J. W., and Baker, C. B., "A Note on the Inhibition of Cavitation in Dilute Polymer Solutions", App. Res. Lab., Tech. Memo., File No. 75-285, Penn. State Uni., Nov., 1975.

9. Arndt, R. E. A., and Keller, A. P., "Free Gas Content Effects on Cavitation Inception and Noise in a Free Shear Flow", Proc. IAHR Symp. Two Phase Flow and Cavitation in Power Generation Systems, Grenoble, France, pp. 3-16, 1976.

10. Arndt, R. E. A., and George, W. K., "Pressure Fields and Cavitation in Turbulent Shear Flows", 12th Symp., Naval Hydrodynamics, Washington, D. C., pp. 327-39, 1978.

11. Arndt, R. E. A., Holl, J. W., Bohn, J. C., and Bechtel, W. T., Influence of Surface Irregularities on Cavitation Performance", J. Ship Res., Vol. 23, No. 3, pp. 157-170, Sept., 1979.

12. Arndt, R. E. A., "Cavitation in Fluid Machinery and Hydraulic Structures", Ann. Rev. of Fluid Mech., Vol. 13, pp 273-328, 1981.

13. Arndt, R. E. A., "The Correlation Between Cavitation and Pressure Fluctuation in Turbulent Shear Flow", Proposal 81-8, St. Anthony Falls Hyd. Lab., Uni. of Minnesota, March, 1981.

14. Baker, C. B., Holl, J. W., and Arndt, R. E. A., "The Influence of Gas Content and Polyethylene Oxide Additive upon Confined Jet Cavitation in Water", Applied Res. Lab., Tech. Memo., File No. TM 75-274, Penn. State Uni., Nov., 1975.

15. Ball, J. W., discussion on "Cavitation effect on the discharge Coefficient of the Sharp-edged Orifice Plate", J. Basic Engrg., Vol. 82, Series D, No. 1, pp. 6-10, March, 1960.

16. Barefoot, G. L., "Fluctuating Pressure Characteristics in the Mixing Region of a Perturbed and Unperturbed Round Free Jet", Appl. Res. Lab., Tech. Memo., File No. TM 72-165, Penn. State Uni., Aug., 1972.

17. Barthés-Biesel, D., and Acrivos, A., "Deformation and Burst of a Liquid Droplet Freely Suspended in a Linear Shear Field", J. Fluid Mech., Vol. 61, Part 1, pp. 1-21, 1973.

18. Beuther, P., George, W. K., and Arndt, R. E. A., "Pressure Spectra in a Turbulent Shear Flow", Bulletin Amer. Phys. Soc., 22, 12, Dec., 1977 (b).

19. Beuther, P., George, W. K., and Arndt, R. E. A., "Pressure Spectra in Homogeneous Isotropic Turbulent Flow", Bulletin Amer. Phys. Soc., 22, 12, Dec. 1977 (c).

20. Beavers, G. S., and Wilson, T. A., "Vortex Growth in Jets", J. Fluid Mech., Vol. 44, Part 1, pp. 97-112, 1970.

21. Becker, H. A., and Massaro, T. A., "Vortex Evolution in a Round Jet", J. Fluid Mech., Vol. 31, Part 3, pp. 435-448, 1968.

22. Billet, M. L., Holl, J. W., and Parkin, B. R., "Scale Effects on Cavitating Flows Due to Surface Roughness and Laminar Separation", IAHR, 10th Symp., Vol. 1, pp. 39-52, Tokyo, 1980. (Section for Hydraulic Machinery, Equipment and Cavitation.)

23. Billet, M. L., and Gates, E. M., "A Comparison of Two Optical Techniques for Measuring Cavitation Nuclei", J. Fluids Engrg. Vol. 130, No. 1, March, 1981.

24. Brown, G. L., and Roshko, A., "On Density Effects and Large Structure in Turbulent Mixing Layers", J. Fluid Mech., Vol. 64, Part A, pp. 775-816, 1974.

25. Carroll, J. A., "Observations of the Effects of Boundary Layer and Nuclei on Cavitation of Axisymmetric Bodies", Applied Res. Lab., Tech. Memo., File No. 81-60, Penn. State Uni., 1981.

26. Castro, I. P., and Bradshaw, P., "The Turbulence Structure of a Highly Curved Mixing Layer", J. Fluid Mech., Vol. 73, Part 2, pp. 265-304, 1976.

27. Chandrsuda, C., Mehta, R. D., Weir, R. D., and Bradshaw, P., "Effect of Free Stream Turbulence on Large Structures in Turbulent Mixing Layers", J. Fluid Mech., Vol. 85, Part 4, pp. 693-704, 1978.

28. Crockett, K., and Upp, L., "The Measurement and Effects of Edge Sharpness on the Flow Coefficients of Standard Orifices", J. Fluids Engrg., Vol. 95, Series 1, No. 2, pp. 271-275, June, 1973.

29. Davies, P. O. A. L., and Yule, A. J., "Coherent Structures in Turbulence", J. Fluid Mech., Vol. 69, Part 3, pp. 513-537, 1975.

30. Devin, C., Jr., "Survey of Thermal, Radiation, and Viscous Damping of Pulsating Air Bubbles in Water", J. Acous. Soc. Am., Vol. 31, No. 12, pp. 1654-1667, Dec., 1959.

31. Durst, F., Launder, B. E., Schmidt, F. W., and Whitelaw, J. H., "Turbulent Shear Flows I - Selected Papers from the First International Symposium on Turbulent Shear Flows", Penn. State Uni., University Park, Pennsylvania, U.S.A., April 18-20, 1977.

32. Ellis, A. T., "Parameters Affecting Cavitation and Some New Methods for Their Study", Hydro. Lab., California Institute of Technology, Rept. No. E-115.1, Oct., 1965.

33. Ellis, A. T., Waugh, J. G., and Ting, R. Y., "Cavitation Suppression and Stress Effects in High Speed Flows of Water with Dilute Macromolecular Additives", J. Basic Engrg., Vol. 92, Series D, No. 3, pp. 459-466, Sept., 1970.

34. Epstein, P. S., and Plesset, M. S., "On the Stability of Gas Bubbles in Liquid-gas Solutions", J. Chem. Phys., Vol. 18, No. 11, pp. 1505-1509, Nov., 1950.

35. Fox., F. E., and Herzfeld, K. R.,"Gas Bubbles with Organic Skin as Cavitation Nuclei", J. Acous. Soc. Am., Vol. 26, No. 6, pp. 984-989, Nov., 1954.

36. Franklin, R. E., and McMillan, J., "Noise Generation in Cavitating Flows. The Submerged Water Jet I", Oxford Uni. Engrg. Lab Report No. 1312/80.

37. Franklin, R. E., and McMillan, J., "Noise Generation in Cavitating Flows. The Submerged Water Jet II", Oxford Uni. Engrg. Lab Report No. 1313/80.

38. Franklin, R. E., and McMillan, J., "Noise Generation in Cavitating Flows. The Submerged Water Jet III", Oxford Uni. Engrg. Lab Report No. 1326/80.

39. Freed, D., Walker, W. F., Dube, C. M., and Tokuno, T., "Cavitation near Decelerating Prosthetic Surfaces", Cav. and Polyphase Flow Forum, Joint ASME/ASCE Conf., Boulder, Colorado, June, 1981.

40. Freymuth, P., "On Transition in a Separated Laminar Boundary Layer", J. Fluid Mech., Vol. 25, Part 4, pp. 683-704, 1966.

41. Fuchs, H. V.,"Space Correlations of the Fluctuating Pressure in Subsonic Turbulent Jets", J. Sound and Vib., Vol. 23, No. 1, pp. 77-99, 1972.

42. Fuchs, H. V., "Measurements of Pressure Fluctuations within Subsonic Turbulent Jets", J. Sound and Vib., Vol. 22, No. 3, pp. 361-378, 1972.

43. Fuchs, H. V., "Resolution of Turbulent Jet Pressure into Azimuthal Components", Advis. Group Aerosp. Res. and Develop. Conf. Proc. No. 131, Paper 27, 1973.

44. Fuchs, H. V., Mercker, E., and Michel, U., "Large-scale Coherent Structures in the Wake of Axisymmetric Bodies", J. Fluid Mech., Vol. 93, Part 1, pp. 185-207, 1979.

45. Gates, E. M., "The Influence of Freestream Turbulence, Free Stream Nuclei Populations and a Drag-reducing Polymer on Cavitation Inception on Two Axisymmetric Bodies", Ph. D. dissertation, California Institute of Technology, 1977.

46. Gates, E. M., and Acosta, A. J., "Some Effects of Several Freestream Factors on Cavitation Inception of Axisymmetric Bodies", 12th Symp., Naval Hydro., Washington, D. C., pp. 86-108, 1978.

47. Gates, E. M., Billet, M. L., Katz, J., Ooi, K. K., Holl, J. W., and Acosta, A. J., "Cavitation Inception and Nuclei Distribution, Joint ARL/CIT Experiments", California Institute of Technology, Rep. No. E244.1, 1979.

48. Gates, E. M., Billet, M. L., Ooi, K. K., Oldenziel, D. M., Holl, J. W., and Acosta, A. J., "Joint ARL-CIT Cavitation Roughness Scaling Experiments", California Institute of Technology, Rep. No. E183-5 (in preparation).

49. Harvey, E. N., Barnes, D. K., McElroy, W. D., Whiteley, A. H., Pease, D. C., and Cooper, K. W., "Bubble Formation in Animals I, Physical Factors", J. Cellular and Comp. Physiol., Vol. 24, No. 1, pp. 1-22, Aug.,1944.

50. Holdeman, J. D., and Foss, J. F., "The Initiation, Development and Decay of the Secondary Flow in a Bounded Jet", J. Fluids Engrg., Vol. 97, Series 1, No. 3, Sept., 1975.

51. Holl, J. W., and Wislicenus, G., "Scale Effects on Cavitation", J. Basic Engrg., Vol. 83, Series D, No. 3, pp. 385-395, Sept., 1961.

52. Holl, J. W., and Treaster, A. L., "Cavitation Hysteresis", J. Basic Engrg., Vol. 88, Series D, No. 1, pp. 199-212, March, 1966.

53. Holl, J. W., "Limited Cavitation", Proc. of the Symp. on Cavitation State of Knowledge, ASME, pp. 26-63, June, 1969.

54. Holl, J. W., "Nuclei and Cavitation", J. Basic Engrg., Vol. 92, Series D, No. 4, pp. 681-688, Dec. 1970.

55. Hoyt, J. W., "Effect of High-polymer Solutions on a Cavitating Body", Proc. 11th ITTC, Tokyo, 1966.

56. Hoyt, J. W., "The Effect of Additives on Fluid Friction", J. Basic Engrg., Vol. 94, Series D, No. 2, pp. 258-285, June 1972.

57. Hoyt, J. W., "Cavitation Inception in Polymer Solutions - Effects of Polymers on Surface Tension, Dissolved Air and Nuclei Count", Proc. 14th ITTC, Ottawa, Sept., 1975.

58. Hoyt, J. W., "Effect of Polymer Additives on Jet Cavitation", J. Fluids Engrg., Vol. 98, Series 1, No. 1, pp. 106-112, March 1976.

59. Hoyt, J. W., and Taylor, J. J., "A Photographic Study on Cavitation in Jet Flow", J. Fluids Engrg., Vol. 103, Number 1, March, 1981.

60. Huang, T. T., and Hannan, D. E., "Pressure Fluctuations in the Regions of Flow Transitions", DTNSRDC Rep. 4723, 1975.

61. Hussain, A. K. M. F., and Zedan, M. F., "Effects of the Initial Condition of the Axisymmetric Free Shear Layer: Effects of the Initial Momentum Thickness", Phys. Fluids, Vol. 21, No. 7, pp. 1100-1112, July, 1978.

62. Johnson, Jr., V. E., and Hsieh, T., "The Influence of the Trajectories of Gas Nuclei on Cavitation Inception", 6th Symp. Naval Hydro., 1966.

63. Jorgensen, D. W., "Noise from Cavitating Submerged Water Jets", J. Acous. Soc. Am., Vol. 33, No. 10, pp. 1334-1338, Oct., 1961.

64. Katz, J., "Construction and Calibration of an Holograph Camera Designed for Micro Bubbles Observation in Cavitation Research", CIT Report No. Eng. 183-4, Oct., 1979.

65. Katz, J., "Flow Visualization and Cavitation Observation on Axisymmetric Bodies Using a Modified Holographic Technique", Cav. and Polyphase Flow Forum, Joint ASME/ASCE Mechanics Conf., Boulder, Colorado, June, 1981.

66. Katz, J., and Acosta, A. J., "Observations of Nuclei in Cavitating Flows", Presented at the IAUTAM Symp. on Mechanics and Physics of Bubbles in Fluids, California Institute of Technology, June, 1981.

67. Keller, A. P., "The Influence of the Cavitation Nucleus Spectrum on Cavitation Inception, Investigated with a Scattered Light Counting Method", J. Basic Engrg., Vol. 94, Series D, No. 4, pp. 917-925, Dec. 1972.

68. Keller, A. P., and Weitendorf, E. A., "Influence of Undissolved Air Content on Cavitation Phenomena at the Propeller Blades and on Induced Hull Pressure Amplitudes", Proc. IAHR Symp. Two Phase Flow and Cavitation in Power Generation, Systems, Grenoble, France, pp. 65-76, 1976.

69. Kermeen, R. W., and Parkin, B. R., "Incipient Cavitation and Wake Flow Behind Sharp-edged Disks", California Institute of Technology Hydro. Lab. Rep. 85-4, Aug., 1957

70. Knapp, R. T., and Hollander, A., "Laboratory Investigations of the Mechanism of Cavitation", Trans. ASME., Vol. 70, pp. 419-435, 1948.

71. Knapp, R. T., Daily, J. W., and Hammitt, F. G., Cavitation , McGraw-Hill, New York, 1970.

72. Kohler, R. A., and Billet, M. L., "Light Scattering by a Non-spherical Bubble", Cav. and Polyphase Flow Forum, Joint ASME/ ASCE Mechanics Conf., Boulder, Colorado, June, 1981.

73. Konrad, J. H., "An Experimental Investigation of Mixing in Two-dimensional Turbulent Shear Flows with Applications to Diffusion-limited Chemical Reactions", Project Squid, Tech. Rep. CIT-8-PU, Dec., 1976.

74. Kudirka, A. A., and Decoster, M. A., "Jet Pump Cavitation with Ambient and High Temperature Water", Trans. ASME, J. Fluid Engrg., Vol. 101, No. 1, pp. 93-99, March, 1979.

75. Kuiper, G., "Cavitation Inception on Ship Propeller Models", Ph. D. dissertation, Netherlands Ship Model Basin, 1981.

76. Lau, J. C., Fischer, M. J., and Fuchs, H. V., "The Intrinsic Structure of Turbulent Jets", J. Sound and Vib., Vol. 22, Part 4, pp. 379-406, 1972.

77. Laurence, J. C. and Stickney, T. M., "Further Measurements of Intensity, Scale, and Spectra of Turbulence in a Subsonic Jet", NACA Tech. Note 3576, Oct., 1956.

78. Lienhard, J. H., and Stephenson, J. M., "Temperature and Scale Effects upon Cavitation and Flashing in Free and Submerged Jets", J. Basic Engrg., Vol. 88, Series D, No. 2, pp. 525-532, June, 1966.

79. Lienhard, J. H., and Goss, C. D., "Influence of Size and Configuration on Cavitation in Submerged Orifice Flows", ASME Paper No. 71-FE-39, 1971.

80. Lindgren, H., and Johnsson, C. A., "Cavitation Inception on Head Forms ITTC Comparative Experiments", 11th ITTC, Tokyo, 1966.

81. Michalke, A., "On Spatially Growing Disturbances in an Inviscid Shear Layer", J. Fluid Engrg., Vol. 23, Part 3, pp. 521-544, 1965.

82. Michalke, A., and Fuchs, H. V., "On Turbulence and Noise of an Axisymmetric Shear Flow", J. Fluid Mech., Vol. 70, Part 1, pp. 179-205, 1975.

83. Mowbray, D. E., "The Use of Schlieren and Shodowgraph Techniques in the Study of Flow Patterns in Density Stratified Liquids", J. Fluid Mech., Vol. 27, Part 3, pp. 595-608, 1967.

84. Morel, T., "Comprehensive Design of Axisymmetric Wind Tunnel Contraction", Trans. ASME, J. Fluid Engrg., Vol. 97, Series 1, No. 2, pp. 225-233, June, 1975.

85. Numaichi, F., Yamabe, M., and Ōba, R., "Cavitation Effect on the Discharge Coefficient of the Sharp Edged Orifice Plate", J. Basic Engrg., Vol. 82, Series D, No. 1, pp. 1-11, March, 1960.

86. Oldenziel, D. M., "Bubble Cavitation in Relation to Liquid Quality", Delft Hydraulics Lab., Publ. No. 211, May, 1979.

87. Oldenziel, D. M., "Observed Relations Between Wall Roughness and Cavitation Inception", Cav. and Polyphase Flow Forum, Joint ASME/ASCE Mech. Conf., Boulder, Colorado, June, 1981.

88. Ooi, K. K., and Katz, J., "Flow Visualization of Cavitation in Water Jets and Nuclei Distribution Measurements by Holography", Cav. and Polyphase Flow Forum, ASME Conf., New Orleans, 1980.

89. Oshima, R., "Theory of Scale Effects on Cavitation Inception on Axially Symmetric Bodies", J. Basic Engrg., Vol. 83, Series D, No. 3, pp. 379-398, Sept., 1961.

90. Parkin, B. R., "Scale Effects on Cavitating Flow", Ph. D. dissertation, California Institute of Technology, 1952.

91. Parkin, B. R., and Kermeen, R. W., "Incipient Cavitation and Boundary Layer Interaction on a Streamlined Body", California Institute of Technology, Hydro. Lab., Rep. No. E-35.2, Dec., 1953.

92. Patel, P. D., and Theofanous, F. G., "Hydrodynamic Fragmentation of Drops", J. Fluid Mech., Vol. 103, pp. 207-223, 1981.

93. Pease, D. C., and Blinks, L. R., "Cavitation from Solid Surfaces in the Absence of Gas Nuclei", J. Physical and Colloidal Chem., Vol. 51, pp. 556-567, 1947.

94. Perry, J. A., and Watmuff, J. H., "The Phase-averaged Large Scale Structures in Three-dimensional Turbulent Wakes", J. Fluid Mech., Vol. 103, pp. 33-51, 1981.

95. Peterson, F. B., "Hydrodynamic Cavitation and Some Considerations of the Influence of Free Gas Content", 9th Symp. Naval Hydro., Paris, Vol. 2, pp. 1131-86, 1972.

96. Peterson, F. B., Danel, F., Keller, A., and Lecoffe, Y., "Determination of Bubble and Particulate Spectra and Number Density in a Water Tunnel with Three Optical Techniques", Proc. 14th ITTC, Ottawa, Vol. 2, pp. 27-52, 1975.

97. Plesset, M. S., "The Tensile Strength of Liquids", Cavitation State of Knowledge, pp. 15-25, ASME, 1969.

98. Plesset, M. S., and Prosperetti, A., "Bubble Dynamics and Cavitation", Ann. Rev. Fluid Mech., Vol. 9, pp. 145-185, 1977.

99. Prosperetti, A., "Nonlinear Oscillations of Gas Bubbles in Liquids: Transient Solutions and the Connection between Subharmonic Signal Cavitation", J. Acoust. Soc. Am., Vol. 57, No. 4, pp. 810-821, April 1975.

100. Prosperetti, A., "Application of the Subharmonic Threshold to the Measurement of the Damping of Oscillating Gas Bubbles", J. Acoust. Soc. Am., Vol. 61, No. 1, pp. 11-16, Jan., 1977.

101. Prosperetti, A., "Viscous Effects on Perturbed Spherical Flows", Quarterly of Appl. Math., pp. 339-352, Jan., 1977.

102. Roshko, A., "Structure of Turbulent Shear Flows: A New Look", AIAA Journal, Vol. 14, No. 10, pp. 1349-1357, Oct., 1976.

103. Rouse, H., "Cavitation in the Mixing Zone of a Submerged Jet", La Houille Blanche, Nos. 1 and 2, 1953.

104. Rouse, H., "Jet Diffusion and Cavitation", J. Boston Soc. of Civil Eng., Vol. 53, July 1966.

105. Sami, S., Carmody, T., and Rouse, H., "Jet Diffusion in the Region of Flow Establishment", J. Fluid Mech., Vol. 27, Part 2, pp. 231-252, 1967.

106. Schiebe, F. R., "The Influence of Gas Nuclei Size Distribution on Transient Cavitation near Inception", St. Anthony Falls Hyd. Lab., Project Rep. No. 107, Uni. of Minnesota, May, 1969.

107. Schiebe, F. R., "Measurement of the Cavitation Susceptibility of Water Using Standard Bodies", St. Anthony Falls Hyd. Lab., Project Rep. No. 118, Uni. of Minnesota, 1972.

108. Strasberg, M., "The Pulsation Frequency of Nonspherical Gas Bubbles in Liquids", J. Acous. Soc. Am., Vol. 25, No. 3, pp. 536-537, May, 1953.

109. van der Meulen, J. H. J., "A Holographic Study of Cavitation on Axisymmetric Bodies and the Influence of Polymer Additives", Ph. D. Thesis, Univ. Twente, The Netherlands, 1976.

110. van der Meulen, J. H. J., "A Holographic Study of the Influence of Boundary Layer and Surface Characteristics on Incipient and Developed Cavitation on Axisymmetric Bodies", 12th Symp. Naval Hydro., Washington, D. C., pp. 433-51, 1978.

111. van der Walle, F., "On the Growth of Nuclei and the Related Scaling Factors in Cavitation Inception", 4th Symp. Naval Hydrodynamics, Aug., 1962.

112. Winant, C. D., and Browand, F. K., "Vortex Pairing: the Mechanism of Turbulent Mixing Layer Growth at Moderate Reynolds Number", J. Fluid Mech., Vol. 63, Part 2, pp. 237-255, 1974.

113. Wygnanski, I., Oster, D., Fiedler H., and Dziomba, B., "On the Perserverance of a Quasi-two-dimensional Eddy-structure in a Turbulent Mixing Layer", J. Fluid Mech., Vol. 93, Part 2, pp. 325-335, 1979.

114. Yungkurth, C. B., and Billet, M. L., "A Calibration Procedure for a Light Scattering System", Cav. and Polyphase Flow Forum, Joint ASME/ASCE Mech. Conf., Boulder, Colorado, June, 1981.

115. Clay, C. S., and Medwin, H., Acoustical Oceanography: Principles and Applications , pp. 199, John Wiley & Sons, Inc., 1977.

APPENDIX 1

ORDER OF MAGNITUDE ANALYSIS OF THE TERMS IN THE RAYLEIGH-PLESSET EQUATION

The Rayleigh-Plesset equation is given by

$$R\ddot{R} + \frac{3}{2}\dot{R}^2 = \frac{1}{\rho}\left[P_c - P_\infty(t) - \frac{2S}{R} - \frac{4\nu\dot{R}}{R}\right] \tag{A.1}$$

If the circular frequency of the pressure fluctuation is given by ω, then we would expect the change in R to be proportional to ω too. Let R be given by

$$R = R_o + \varepsilon e^{-j\omega t} \tag{A.2}$$

where R_o is the initial bubble radius and ε is the amplitude of oscillation from the mean radius. It should be pointed out that ε could be of the same order of magnitude as R_o. Therefore, it follows from Equation (A.2) that

$$\dot{R} \sim \omega\varepsilon$$

and

$$\ddot{R} \sim \omega^2\varepsilon$$

Furthermore, we define

$$R^* = \frac{R}{R_o} = O(1)$$

$$\varepsilon^* = \frac{\varepsilon}{R_o} = O(1)$$

$$\omega^* = \frac{\omega}{\omega_o} = O(\delta),\ \delta << 1.$$ (ω_o is the natural frequency of the bubble). Thus, the left-hand terms of equation (A.1) become

$$R\ddot{R} \sim R^*\varepsilon^*\omega^{*2} = O(\delta^2)$$

$$\dot{R}^2 \sim \varepsilon^{*2}\omega^{*2} = O(\delta^2)$$

In addition

$$\text{pressure term} \sim \frac{1}{\rho u_o^2} \quad (u_o = \omega_o R_o)$$

$$\text{viscous term} \sim \frac{\varepsilon^* \omega^*}{R^*} = O(\delta) \quad ,$$

and surface tension term $\sim \frac{1}{W_e}$ (W_e = Weber number = $\frac{S}{\rho R u_o^2}$) .

By this order of magnitude arguments we can conclude that if the time scale of the pressure fluctuations is small in comparison with the response time of the bubble, then the Rayleigh-Plesset equation can be simplified to:

$$0 = P_c - P_\infty(t) - \frac{2S}{R}$$

or

$$P_\infty(t) = P_c - \frac{2S}{R}$$

$$= P_g(T) + P_V(T) - \frac{2S}{R} \quad . \qquad \text{(A.3)}$$

APPENDIX 2. COMPUTATION OF THE PROBABLE CAVITATION OCCURRENCE PARAMETER, N_p

A2.1 Objective

The aim here is to determine if the presently measured incipient cavitation index is a function of the parameter N_p as defined in Equation (A2.1) below. If it turns out that a unique curve is obtained when σ_i is plotted against N_p, then this would strongly suggest that Equation (A2.1) is an accurate description of the scaling law that governs cavitation in jets. Before the plot can be performed, the values of N_p corresponding to the various measured σ_i's for the three different jets operating at different dissolved air contents, have to be computed. This was performed in the manner shown below in Section A2.2. An example was used to illustrate the steps and arguments followed. It should be pointed out that two assumptions were made to enable the calculations to be carried out. They were:

i) that the negative peak pressure fluctuation intensities scaled with $\frac{1}{2}\rho V_j^2$; and

ii) the probability distribution curve of pressure fluctuation intensities was the same for all three jets.

A2.2 Illustrative Example

Define

$$N_P = \Sigma N_{Pk} \tag{A2.1}$$

and

$$N_{Pk} = n_k \times P_k(P_f) \tag{A2.2}$$

where

n_k = total number of nuclei in size category k that were present in the cavitation-prone region of the jet; and

$P_k(P_f)$ = cumulative probability of favorable negative peak pressure fluctuation intensities that would cause the nuclei in the said category to grow explosively.

Consider the case of the 3.17 mm jet at a dissolved air content of 14.1 ppm and at a velocity of 20 m/s. It has been found that inception in the jet occurred at a mean static pressure, P_T, of 5.04 psi (corresponds to $\sigma_i = 0.16$). In addition, nuclei population measurements by holography revealed that nuclei of only two size categories were present in the jets investigated. These categories corresponded to mean nuclei radii of 7.5 μm and 15 μm. For convenience, subscripts 1 and 2 will be used in Equation (A2.2) to denote variables that are related to the 7.5 μm and 15 μm size nuclei, respectively.

Bubble dynamics dictates that inception would only occur when the instantaneous local pressure P_ℓ satisfies the equation below:

$$P_\ell \leq P_v - \frac{4S}{3R} \tag{A2.3}$$

The symbols have their usual meanings. In the case of the 7.5 μm size nuclei, Equation (A2.3) is satisfied when

$$P_\ell \leq -1.44 \text{ psi}$$

while

$$P_\ell \leq -0.52 \text{ psi for the 15 μm size.}$$

The negative sign indicates that the fluid is under tension. Therefore, the minimum pressure fluctuation, P'_{min}, required to cause the onset of cavitation is given by

$$P'_{min} = (P_{\ell min} - P_T)$$

$$= -6.48 \text{ psi (for the 7.5 μm nuclei)}$$

and $P'_{min} = -5.56$ psi (for the 15 μm nuclei).

In this example, the minimum required pressure fluctuation for the two size categories translates into 22% and 19% of the dynamic head, respectively. From the probability distribution curve in Figure 5.45, the cumulative probabilities are

$$P_1(P_f) = 0.33$$

and

$$P_2(P_f) = 0.43.$$

For convenience, the cumulative probabilities of the peak fluctuation intensities from negative infinity to specific fluctuation intensity levels are tabulated as shown in Table A2.1 below.

$\frac{P'}{\frac{1}{2}\rho V_j^2}$	$P(P_f)\times 10^2$	$\frac{P'}{\frac{1}{2}\rho V_j^2}$	$P(P_f)\times 10^2$
$0 \geq$	55.58	$-0.9 \geq$	4.93
$-0.1 \geq$	43.24	$-1.0 \geq$	3.08
$-0.2 \geq$	33.49	$-1.1 \geq$	1.85
$-0.3 \geq$	26.09	$-1.2 \geq$	0.86
$-0.4 \geq$	20.54	$-1.3 \geq$	0.43
$-0.5 \geq$	16.22	$-1.4 \geq$	0.18
$-0.6 \geq$	12.70	$-1.5 \geq$	0.06
$-0.7 \geq$	9.74	$-1.6 \geq$	0.00
$-0.8 \geq$	7.15		

Table A2.1. A tabulation of the cumulative probabilities of negative peak pressure fluctuation intensities.

In addition, from nuclei measurements we have,

$$n_1 = 2.69\times 10^3$$

and

$$n_2 = 349 \quad .$$

Therefore, Equations (A2.1) and (A2.2) imply that

$$N_p = n_1 \times P_1(P_f) + n_2 \times P_2(P_f)$$

$$= (5690\times 0.33) + (349\times 0.43)$$

$$= 1051.8$$

Hence, the calculated N_p corresponding to $\sigma_i = 0.16$ for the 3.17 mm jet is 1052.

Proceeding in the same manner illustrated above, the values of N_p for the other measured σ_i's were generated. The calculations were done for jet velocities of 10 m/s, 20 m/s and 30 m/s. The calculated results are tabulated as shown in Tables A2.2(a) - (c) to Tables A2.4(a) - (c) below. These results are discussed in the main text.

Cavitation Inception Index σ_i	Air Control α ppm	Nuclei size = 7.5 μm			Nuclei size = 15 μm			N_P
		$n_1 x10^{-3}$	$P_1(P_f)x10^2$	$N_{P_1} x10^{-2}$	$n_2 x10^{-2}$	$P_2(P_f)x10^2$	$N_{P_2} x10^{-1}$	
0.27	14.1	11.01	16.2	17.84	14.34	20.5	29.40	2078
0.24	10.9	4.99	16.2	8.08	8.12	26.1	21.19	1020
0.23	7.7	1.40	20.5	2.87	4.78	26.1	12.48	412
0.22	4.2	0.28	20.5	0.57	1.48	26.1	3.86	96

Table 2.2(a)

Cavitation Inception Index	Air Control	Nuclei size = 7.5 μm			Nuclei size = 15 μm			
σ_i	α ppm	$n_1 x10^{-3}$	$P_1(P_f)x10^2$	$N_{P_1} x10^{-2}$	$n_2 x10^{-2}$	$P_2(P_f)x10^2$	$N_{P_2} x10^{-1}$	N_P
0.27	14.1	11.01	26.1	28.74	14.34	26.1	37.43	3248.3
0.24	10.9	4.99	26.1	13.02	8.12	33.5	27.20	1574
0.23	7.7	1.40	33.5	4.69	4.78	33.5	16.01	629.1
0.22	4.2	0.28	33.5	0.94	1.48	33.5	4.96	143.6

Table 2.2(b)

Cavitation Inception Index σ_i	Air Control α ppm	Nuclei size = 7.5 μm			Nuclei size = 15 μm			N_P
		$n_1 x10^{-3}$	$P_1(P_f)x10^2$	$N_{P_1} x10^{-2}$	$n_2 x10^{-2}$	$P_2(P_f)x10^2$	$N_{P_2} x10^{-1}$	
0.27	14.1	11.01	33.5	36.88	14.34	33.5	48.04	4168.4
0.24	10.9	4.99	33.5	16.72	8.12	33.5	27.20	1944
0.23	7.7	1.40	33.5	4.69	4.78	33.5	16.01	629.1
0.22	4.2	0.28	33.5	0.94	1.48	33.5	4.96	143.6

Table 2.2(c)

Table 2.2 A tabulation of N_P for the 6.35 mm jet without flow seeding: (a) V_j = 10 m/s, (b) V_j = 20 m/s and (c) V_j = 30 m/s.

Cavitation Inception Index σ_i	Air Control α ppm	Nuclei size = 7.5 μm			Nuclei size = 15 μm			N_P
		$n_1 x10^{-3}$	$P_1(P_f)x10^2$	$N_{P_1} x10^{-2}$	$n_2 x10^{-2}$	$P_2(P_f)x10^2$	$N_{P_2} x10^{-2}$	
0.15	14.1	2.69	20.5	5.51	3.49	33.5	11.69	667.9
0.11	10.9	1.22	26.1	3.18	1.98	33.5	6.63	384.3
0.07	7.7	0.34	26.1	0.89	1.17	33.5	3.92	128.2
0.06	4.2	0.07	26.1	0.18	0.36	43.2	1.56	33.6

Table 2.3(a)

Cavitation Inception Index σ_i	Air Control α ppm	Nuclei size = 7.5 μm			Nuclei size = 15 μm			N_P
		$n_1 x10^{-3}$	$P_1(P_f)x10^2$	$N_{P_1} x10^{-2}$	$n_2 x10^{-2}$	$P_2(P_f)x10^2$	$N_{P_2} x10^{-1}$	
0.15	14.1	2.69	33.5	9.01	3.49	43.2	15.08	1051.8
0.11	10.9	1.22	43.2	5.27	1.98	43.2	8.55	612.5
0.07	7.7	0.34	43.2	1.47	1.17	43.2	5.05	197.50
0.06	4.2	0.07	43.2	0.30	0.36	55.6	2.00	50

Table 2.3(b)

Cavitation Inception Index σ_i	Air Control α ppm	Nuclei size = 7.5 μm			Nuclei size = 15 μm			N_p
		$n_1 x 10^{-3}$	$P_1(P_f) x 10^2$	$N_{P_1} x 10^{-2}$	$n_2 x 10^{-2}$	$P_2(P_f) x 10^2$	$N_{P_2} x 10^{-1}$	
0.15	14.1	2.69	43.2	11.62	3.49	43.2	15.08	1312.80
0.11	10.9	1.22	43.2	5.27	1.98	43.2	8.55	612.50
0.07	7.7	0.34	43.2	1.47	1.17	55.6	6.50	212.0
0.06	4.2	0.07	55.6	0.39	0.36	55.6	2.00	59

Table 2.3(c)

Table 2.3 A tabulation of N_p for the 4.76 mm jet without flow seeding: (a) V_j = 10 m/s, (b) V_j = 20 m/s and (c) V_j = 30 m/s.

Cavitation Inception Index σ_i	Air Control α ppm	Nuclei size = 7.5 μm			Nuclei size = 15 μm			N_P
		$n_1 x10^{-3}$	$P_1(P_f)x10^2$	$N_{P_1} x10^{-2}$	$n_2 x10^{-2}$	$P_2(P_f)x10^2$	$N_{P_2} x10^{-1}$	
0.16	14.1	1.19	20.5	2.44	1.54	33.5	5.16	295.60
0.08	10.9	0.54	26.1	1.41	0.88	33.5	2.95	170.5
0.06	7.7	0.15	26.1	0.39	0.52	43.2	2.25	61.50
0.03	4.2	0.03	33.5	0.10	0.16	43.2	0.69	16.90

Table 2.4(a)

Cavitation Inception Index σ_i	Air Control α ppm	Nuclei size = 7.5 μm			Nuclei size = 15 μm			N_P
		$n_1 \times 10^{-3}$	$P_1(P_f) \times 10^2$	$N_{P_1} \times 10^{-2}$	$n_2 \times 10^{-2}$	$P_2(P_f) \times 10^2$	$N_{P_2} \times 10^{-1}$	
0.16	14.1	1.19	33.5	3.99	1.54	43.2	6.65	465.5
0.08	10.9	0.54	43.2	2.33	0.88	43.2	3.80	271
0.06	7.7	0.15	43.2	0.65	0.52	55.6	2.89	93.9
0.03	4.2	0.03	55.6	0.17	0.16	55.6	0.89	25.9

Table 2.4(b)

Cavitation Inception Index σ_i	Air Control α ppm	Nuclei size = 7.5 μm			Nuclei size = 15 μm			N_P
		$n_1 x10^{-3}$	$P_1(P_f)x10^2$	$N_{P_1} x10^{-2}$	$n_2 x10^{-2}$	$P_2(P_f)x10^2$	$N_{P_2} x10^{-1}$	
0.16	14.1	1.19	43.2	5.14	1.54	43.2	6.65	580.5
0.08	10.9	0.54	43.2	2.33	0.88	55.6	4.89	281.9
0.06	7.7	0.15	55.6	0.83	0.52	55.6	2.89	111.9
0.03	4.2	0.03	55.6	0.17	0.16	55.6	0.89	25.9

Table 2.4(c)

Table 2.4 A tabulation of N_P for the 3.17 mm jet without flow seeding: (a) V_j = 10 m/s, (b) V_j = 20 m/s and (c) V_j = 30 m/s.